Eindhoven University of Technology

MASTER

From supersaturated water vapour to supercooled liquid water

analysis and experiments

Holten, V.

Award date:
2004

Link to publication

From supersaturated water vapour to supercooled liquid water; analysis and experiments

Vincent Holten

R-1634-A

April 2004

Supervisors:
prof. dr. ir. M.E.H. van Dongen
D.G. Labetski

Eindhoven University of Technology
Gas Dynamics Group

/department of applied physics

Abstract

Homogeneous nucleation rates of water between 10^{14} and 10^{17} $m^{-3}s^{-1}$ have been measured in an expansion wave tube, at temperatures of 200–240 K, using helium as a carrier gas at atmospheric pressure. At low temperature, a large discrepancy between the experimental data and the predictions of the classical nucleation theory (CNT) is found. To describe the measurements better, the temperature dependence of the CNT is adjusted, the supersaturation dependence being corrected as well. The corrected theory is found to agree both with our data and with the measurements of Wölk et al. [J. Wölk and R. Strey, J. Phys. Chem. B 105, 11683 (2001)].

Contents

1. Introduction

The condensation of water is an everyday phenomenon. When water boils, a cloud of tiny droplets is formed in the cold air above it. Clouds in the sky also contain liquid water drops, even though their temperature can be far below 0 °C.

Condensation, the formation of droplets from a supersaturated vapour, consists of two steps: first, a few dozen molecules have to form a cluster that is stable – small clusters have a large probability of falling apart again. This is a statistical process, called *nucleation*. If the cluster consists only of vapour molecules, then we call the process homogeneous nucleation; if other substances – such as dust particles – induce the nucleation, we have heterogeneous nucleation.

The second process is droplet growth: the growth of the molecular clusters to macroscopic droplets. It is this process that allows us to see the condensation; nucleation itself is an invisible process.

In this research we focus on the homogeneous nucleation *rate*: the speed of nucleation, that is, the number of stable clusters that are formed per unit of space and time. In this report we will present our experimental nucleation rate measurements as well as various theoretical descriptions of this process.

2. Nucleation Theory

2.1 General

2.1.1 Capillarity approximation

Before quantities such as the nucleation rate can be derived, a model for the cluster has to be adopted. Most theories are based on a very simplified model called the 'capillarity approximation'. In this model, it is assumed that he cluster is spherical and that it has a uniform density equal to that of the bulk liquid. The interface between the liquid and the vapour is taken infinitely thin and the surface tension there is equal to that of the interface between the bulk phases at equilibrium.

We expect a real cluster to have very different properties, and it seems likely that not a single assumption of the capillarity approximation is satisfied. Nevertheless, it is frequently used, at least in all theories we will encounter in this chapter.

We can simply take the volume of the cluster v_n proportional to the number of molecules n that are in it:

$$v_n = n\, v_1, \tag{2.1}$$

where v_1 is the average volume available for one molecule in the bulk liquid, i.e., $v_1 = M/(\rho_\ell N_A)$ with ρ_ℓ the bulk liquid density (units mass per volume), M is the molar mass and N_A is the Avogadro constant.

The surface energy of the cluster is represented by the product σa_n; σ is the surface energy per unit area and a_n is the surface area of the drop. Using the geometry of a sphere, the surface area is related to the volume:

$$a_n = (36\pi)^{1/3} v_n^{2/3} = a_1 n^{2/3}. \tag{2.2}$$

In the last step Eq. 2.1 was used, and $a_1 \equiv (36\pi)^{1/3} v_1^{2/3}$ was introduced.

2.1.2 Cluster distribution

The Helmholtz free energy of a cluster is, by definition,[1]

$$F_n = n\mu_l + \sigma a_n - p\, v_n, \tag{2.3}$$

where μ_l is the chemical potential (the Gibbs energy per molecule) of the liquid, and p is the pressure of the surrounding vapour. The canonical partition function for a cluster at rest is then, also by definition,[1]

$$q_n = \exp(-F_n/kT), \tag{2.4}$$

where k is the Boltzmann constant. The partition function of the total system (which has a volume V) must include the molecular configurations of the surrounding vapour.

Assuming that the molecules in the vapour do not interact with those in the drop, the total partition function can be written as a product

$$Q^1 = q_n Q_{N-n},$$ (2.5)

where Q_{N-n} is the partition function of the vapour and the '1' in Q^1 denotes that the cluster is at rest at a single position. Next, we have to account for the translational freedom of the cluster, which means that we allow it to be anywhere in the volume V. Simply multiplying Q^1 by V gives a dimension problem; instead, we have to introduce a volume scale, which we will call ϑ. The partition function of the total system Q^V, allowing cluster translation, is then

$$Q^V = Q^1 \times \frac{V}{\vartheta}.$$ (2.6)

It is not at all straightforward what value the volume scale should have. Since it has to do with the translation of the cluster, we expect it to be related to, and dependent on, cluster parameters such as it size. We could, for example, take the volume scale equal to the average volume in which the centre of mass of the cluster fluctuates due to collisions of vapour molecules. Regardless of the volume scale, it can be shown[1] that (under the assumption that the vapour is an ideal gas) Eq. 2.6 leads to

$$\rho_n = \frac{1}{\vartheta} \exp(-W_n/kT),$$ (2.7)

where W_n is the work of cluster formation, which will be derived in the next section. The cluster distribution ρ_n has the units of number per volume; it tells how many clusters of a certain size n are present. The exponential factor $\exp(-W_n/kT)$ can be seen as the familiar Boltzmann factor, governing the occupation of states with different energies.

2.1.3 Work of formation

The work of formation of a cluster is the difference in the Helmholtz free energy between a system with and without the cluster. It is:[2]

$$W_n = n\Delta\mu - v_n \Delta p + \sigma a_n.$$ (2.8)

The quantity $\Delta\mu$ is the difference in chemical potential between a drop and a vapour molecule (Figure 2.1):

$$\Delta\mu = \mu_l(p_l) - \mu_v(p).$$ (2.9)

The pressure in the drop p_l is higher than the pressure of the surrounding vapour p, and Δp is defined as

$$p_l = p + \Delta p.$$ (2.10)

The pressure difference, sometimes called the Laplace pressure, is caused by the curved surface and the surface tension of the drop. If the drop is in mechanical equilibrium,[3]

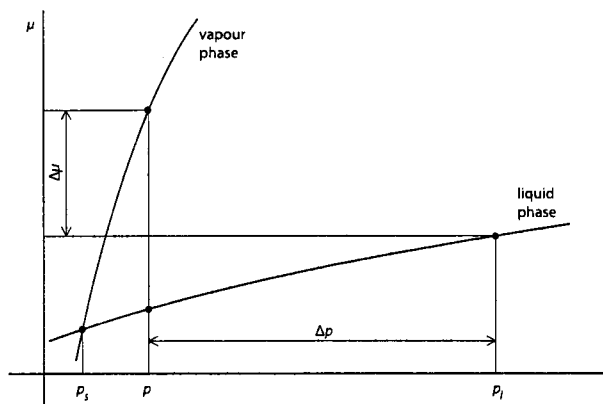$$\Delta p = \frac{2\sigma}{r},$$ (2.11)

Figure 2.1: Chemical potential of the vapour and liquid phases as a function of pressure.

where r is the drop radius. Eq. 2.11 is called the *Laplace equation*.

Using a thermodynamic relation called the Gibbs-Duhem equation,[4] the chemical potential of the drop at pressure p_l can be related to the chemical potential at pressure p:

$$\mu_l(p_l) = \mu_l(p + \Delta p) = \mu_l(p) + v_1 \Delta p. \tag{2.12}$$

We define the *supersaturation* of the vapour S as:

$$kT \ln S = \mu_v(p) - \mu_v(p_s). \tag{2.13}$$

The pressure p_s is the saturated vapour pressure, the pressure that exists over a liquid when it is in equilibrium with its vapour. At this pressure, the chemical potentials of liquid and vapour are equal. For a perfect gas, Eq. 2.13 simplifies to:

$$S(p, T) = p/p_s(T). \tag{2.14}$$

Using the previous definitions, we are now ready to derive an expression for $\Delta \mu$.

$$\Delta \mu = \mu_l(p_l) - \mu_v(p) \tag{2.15}$$

$$= \mu_l(p_l) - \mu_l(p_s) + \mu_v(p_s) - \mu_v(p) \tag{2.16}$$

$$\approx \mu_l(p_l) - \mu_l(p) + \mu_v(p_s) - \mu_v(p) \tag{2.17}$$

$$= v_1 \Delta p - kT \ln S. \tag{2.18}$$

The three steps here need explanation: (2.15)$\rightarrow$(2.16) Here we used that $\mu_l = \mu_v$ at $p = p_s$. (2.16)$\rightarrow$(2.17) Because $\Delta p \gg p - p_s$, we can make the approximation $\mu_l(p_l) - \mu_l(p_s) \approx \mu_l(p_l) - \mu_l(p)$.* (2.17)$\rightarrow$(2.18) Here, (2.12) and (2.13) were used.

Finally, substituting the expression for $\Delta \mu$ in the one for the work of formation, Eq. 2.8, yields

$$W_n = v_n \Delta p - n kT \ln S - v_n \Delta p + \sigma a_n$$
$$= \sigma a_1 n^{2/3} - n kT \ln S. \tag{2.19}$$

---

*This is correct for pure vapours. If a carrier gas is present, no significant errors are introduced for atmospheric conditions. For higher carrier gas pressures, corrections are needed.[2]
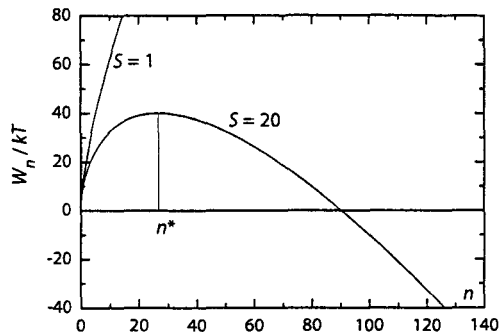
Figure 2.2: Work of formation of a cluster of water molecules as a function of the number of molecules, according to Eq. 2.20, at 220 K. The work is shown for two saturations: 1 and 20.

For the purpose of shortening the notation, a dimensionless surface energy $\Theta \equiv \sigma a_1/kT$ is introduced, so that Eq. 2.19 simplifies to:

$$W_n/kT = \Theta n^{2/3} - n \ln S. \tag{2.20}$$

The work of formation can thus be described by two terms: one is proportional to the surface area and represents the energy needed to form a new phase interface; the other one is proportional to the volume and represents the energy gained by forming an amount of the new phase (if $S > 1$); see Fig. 2.2.

The cluster size at which the work of formation is maximal is called the 'critical size', or n^*. Clusters smaller than this size have a high probability to shrink; clusters that are larger tend to grow. We can determine n^* by solving $\partial W/\partial n|_{n^*} = 0$; this gives

$$n^* = \left(\frac{2\Theta}{3\ln S}\right)^3. \tag{2.21}$$

If the $\Delta\mu$ in Eq. 2.18 is evaluated for a critical cluster, using the Laplace equation, Eq. 2.21 and the relation $nv_1 = \frac{4}{3}\pi r^3$, it can be shown that

$$\Delta\mu = 0 \qquad \text{for a critical cluster}, \tag{2.22}$$

so that a critical cluster has the same chemical potential as the vapour.

Now that we know the work of formation, the only unknown on the right-hand side of Eq. 2.7 is the volume scale, ϑ.

2.1.4 Volume scales

As already mentioned, it is not clear which value should be chosen for the volume scale. In early theories the notion of such a scale never occurred. It was during the "replacement free energy" controversy[5-8] in the 1960s and 70s that the confusion started about the way the translational freedom of the cluster should be accounted for. The issue was never really solved, until in 1997 Reiss, Kegel and Katz[1,9] claimed to have found a solution. Since the theories now called 'classical' are still the most widely used, we will show their volume scales.

Standard theory

What is called 'standard theory' in this text is the classical theory by Becker and Döring[10] of 1935 with an additional $1/S$ factor in the formula for the nucleation rate;

a correction which is generally agreed to be required.[1] In the standard theory, the volume scale is independent of the cluster size; it is the volume per vapour molecule, at saturation:

$$\vartheta^{\,\text{stan}} = 1/\rho_1^{\text{sat}}. \tag{2.23}$$

Girshick-Chiu theory

In 1990, Girshick and Chiu[11] argued that at saturation ($S = 1$), the work of formation of a monomer ($n = 1$) should be zero. In the standard theory, this is not the case since $W_n/kT = \Theta\, n^{2/3}$, at saturation. Girshick and Chiu corrected this as follows:

$$W_n^{\text{GC}} = \Theta\,(n^{2/3} - 1) \qquad \text{at } S = 1, \tag{2.24}$$

so that at general supersaturations

$$\begin{aligned} W_n^{\text{GC}} &= \Theta\,(n^{2/3} - 1) - n \ln S \\ &= W_n/kT - \Theta. \end{aligned} \tag{2.25}$$

To obtain the volume scale, we rewrite the cluster distribution:

$$\begin{aligned} \rho_n^{\text{GC}} &= \rho_1^{\text{sat}} \exp(-W_n^{\text{GC}}/kT) \\ &= \rho_1^{\text{sat}} \exp(\Theta)\exp(-W_n/kT). \end{aligned} \tag{2.26}$$

so that

$$\vartheta^{\,\text{GC}} = \exp(-\Theta)/\rho_1^{\text{sat}}. \tag{2.27}$$

An important property of this correction is that the cluster distribution now yields the correct result for monomers ($n = 1$), namely $\rho_1^{\text{GC}} = \rho_1^{\text{sat}}\,S$. Since it is this consistency which distinguishes the Girshick-Chiu theory from the classical theory, it is sometimes called the internally consistent classical theory (ICCT).

Reiss-Kegel-Katz theory

The volume scale of the RKK theory will be derived later in this chapter; here we will already show the result:

$$\vartheta_n^{\text{RKK}} = (kT\kappa n v_1)^{1/2}, \tag{2.28}$$

where κ is the compressibility of the liquid; $\kappa \equiv (\partial \rho_\ell/\partial p)_T/\rho_\ell$. Note that unlike the previous volume scales, this volume scale does depend on the cluster size n.

2.1.5 Nucleation rate

We want to keep the derivation of the nucleation rate as general as possible. That is why we do not choose a specific volume scale at this point, but assume that it is proportional to a power of n, i.e.,

$$\vartheta_n = \alpha\, n^\gamma, \tag{2.29}$$

where α and γ are arbitrary constants independent of n. We further assume that the volume scale does not depend on the supersaturation.

The derivation itself is based on the so-called 'kinetic method', concisely recapitulated by Girshick and Chiu.[11] We start with an expression for the nucleation rate J that follows from kinetic considerations

$$J = \left[\int_1^\infty \frac{1}{\beta a_n \rho_n^{sat} S^n} \, dn \right]^{-1} = \left[\int_1^\infty e^{-H(n)} dn \right]^{-1}, \tag{2.30}$$

where $H(n) \equiv \ln(\beta a_n \rho_n^{sat} S^n)$. Here β is the impingement rate of monomers, which is taken from ideal gas kinetic theory; an expression for β appears in Table 2.1. The integral is written in this form because we expect the integrand to be a sharply peaked function of n, with the peak around the critical size. This peak is approximated by a Gaussian curve, similar to $\exp[-(n - n^*)^2]$, so that the integration becomes standard. To write the integral in the desired form, H is expanded in a Taylor series around n^*, the critical size, where the derivative of $H(n)$ is zero:

$$H(n) \approx H(n^*) + \tfrac{1}{2}(n - n^*)^2 H''(n^*), \tag{2.31}$$

where the double prime denotes the second derivative. Note that the critical size is redefined here as the n for which $H(n)$ has a minimum; this value may be different from the n^* of Eq. 2.21. When the expansion of H of Eq. 2.31 is substituted back in Eq. 2.30 and the lower integration limit is shifted to $-\infty$, the result is indeed a standard integral, with solution

$$J = \left[\frac{H''(n^*)}{2\pi} \right]^{1/2} \exp\left[H(n^*) \right]. \tag{2.32}$$

We write H using the definition of a_n (Eq. 2.2) and the cluster distribution of Eq. 2.7:

$$H(n) = \ln(\beta a_1) + \ln(n^{2/3}) - \ln(\vartheta_n) - \Theta n^{2/3} + n \ln S. \tag{2.33}$$

To find the critical size, we use that $H'(n^*) = 0$, which gives

$$\tfrac{2}{3} n^{*-1} - \gamma n^{*-1} - \tfrac{2}{3} \Theta n^{*-1/3} + \ln S = 0, \tag{2.34}$$

which leads to

$$\frac{\Theta n^{*2/3} + \tfrac{3}{2}\gamma - 1}{n^*} = \frac{3}{2} \ln S. \tag{2.35}$$

Similar to the approximation of Girshick and Chiu, we now assume that for most cases $\Theta n^{*2/3} \gg |\tfrac{3}{2}\gamma - 1|$. For our experiments $\Theta n^{*2/3} = O(100)$, so that the approximation is justified. The critical size is then

$$n^* = \left(\frac{2}{3} \frac{\Theta}{\ln S} \right)^3, \tag{2.36}$$

which is the same result as obtained before (Eq. 2.21). Apparently, the dependence of the volume scale on the cluster size is too weak to influence the critical size, which remains completely determined by the maximum of the work of formation.

Table 2.1: Substitutions

Θ	$\rightarrow$	$a_1\sigma/kT$		ρ_1	$\rightarrow$	p/kT
a_1	$\rightarrow$	$(36\pi)^{1/3}v_1^{2/3}$		m_1	$\rightarrow$	M/N_A
v_1	$\rightarrow$	$M/\rho_\ell N_A$		ρ_1^{sat}	$\rightarrow$	p_s/kT
β	$\rightarrow$	$(kT/2\pi m_1)^{1/2}\rho_1$		p	$\rightarrow$	$S\,p_s$

To obtain J with Eq. 2.32 we also need the second derivative of H at the critical size:

$$H''(n^*) = \frac{\Theta\,n^{*2/3} + \frac{9}{2}\gamma - 3}{\frac{9}{2}n^{*2}} \approx \frac{\Theta\,n^{*2/3}}{\frac{9}{2}n^{*2}} = \frac{2}{9}\Theta\,n^{*-4/3}. \tag{2.37}$$

In the second step the approximation $\Theta\,n^{*2/3} \gg \left|\frac{9}{2}\gamma - 3\right|$ was made. For this approximation to be allowed, $|\gamma|$ cannot be too large; if for example $\gamma = -2$, the right-hand side is already 12.

Substituting the results, Eqs. 2.36 and 2.37, in the expression for the nucleation rate, Eq. 2.32, and using Eqs 2.7 and 2.20, finally gives

$$J = \frac{1}{\vartheta_{n^*}}\frac{a_1\beta}{3}\left(\frac{\Theta}{\pi}\right)^{1/2}\exp\left[-\frac{4}{27}\frac{\Theta^3}{(\ln S)^2}\right]. \tag{2.38}$$

Since the standard theory has $\vartheta = 1/\rho_1^{\text{sat}}$, we have

$$J^{\text{stan}} = \rho_1^{\text{sat}}\frac{a_1\beta}{3}\left(\frac{\Theta}{\pi}\right)^{1/2}\exp\left[-\frac{4}{27}\frac{\Theta^3}{(\ln S)^2}\right]. \tag{2.39}$$

and generally

$$J = \frac{1}{\rho_1^{\text{sat}}\vartheta_{n^*}} \times J^{\text{stan}}. \tag{2.40}$$

To express the nucleation rate as a function of the physically measurable parameters surface tension, density, vapour pressure and supersaturation, we employ the substitutions summarized in Table 2.1.

$$J^{\text{stan}} = \left(\frac{p_s}{kT}\right)^2\left(\frac{2\sigma M}{\pi N_A}\right)^{1/2}\frac{S}{\rho_\ell}\exp\left[-\frac{16\pi}{3}\left(\frac{M}{N_A\rho_\ell\ln S}\right)^2\left(\frac{\sigma}{kT}\right)^3\right]. \tag{2.41}$$

For the RKK theory, the nucleation rate is

$$J^{\text{RKK}} = \left(\frac{3\rho_\ell}{\kappa}\right)^{1/2}\frac{N_A S p_s}{4\pi\sigma M}(\ln S)^{3/2}\exp\left[\ldots\right], \tag{2.42}$$

where the exponential factor is the same as in Eq. 2.41. Note that the J^{RKK} given here differs from the one shown by Wölk and Strey.[12]

2.2 Reiss-Kegel-Katz theory

The RKK theory[1,9] is based on: (1) the correct counting of molecular cluster configurations; (2) finding the average volume of a fluctuating drop. Combining these leads to the volume scale.

2.2.1 Volume scale

What is called 'the drop' in the original paper is a rigid, spherical container of volume v_n in which there are n molecules. Inside the container, the cluster of molecules can have any shape and size, and it does not have to be in the centre of the container. The only constraint is that the molecules must be in a single cluster, i.e., evaporation is not allowed; see Fig. 2.3.
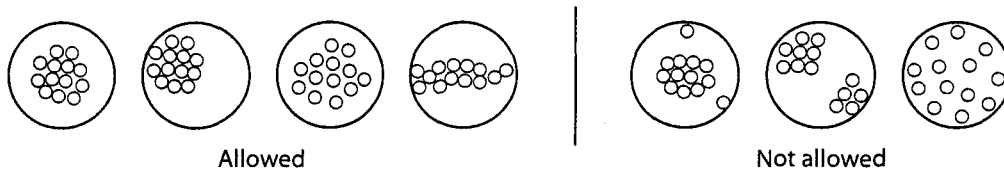

Allowed   Not allowed

Figure 2.3: Molecular configurations that are allowed. The large circle is the spherical container volume; the smaller ones are the molecules.

The partition function $q_n(v_n)$ includes all configurations that are allowed as specified above. The total system has a volume V and contains the drop and $N - n$ vapour molecules in the remaining volume $V - v_n$. In the analysis to follow we will take v_n equal to the average liquid volume of n molecules v_n^*; that is, $v_n^* = n/\rho_\ell$ where ρ_ℓ [m^{-3}] is the density of the bulk liquid. For the moment, we will fix the drop (the container) at a certain position in the system.

Having set the conditions, we will now look at the partition function (PF) of the total system, Q_n^1. Here, the 1 denotes that this PF is fixed at a single position. Since the molecules in the vapour do not interact with those in the drop, the total PF function can be decoupled and written as

$$Q_n^1 = q_n(v_n^*) \, Q_{N-n}(V - v_n^*) = q_n^* \, Q_{N-n}^*, \tag{2.43}$$

where $Q_{N-n}(V - v_n^*)$ is the PF of the vapour molecules. The last equality in Eq. 2.43 is the result of a simplifying notation, summarized in Table 2.2. Generally, a star next to a symbol means 'evaluated at v_n^*'.

Table 2.2: Definition of simplifying notation.

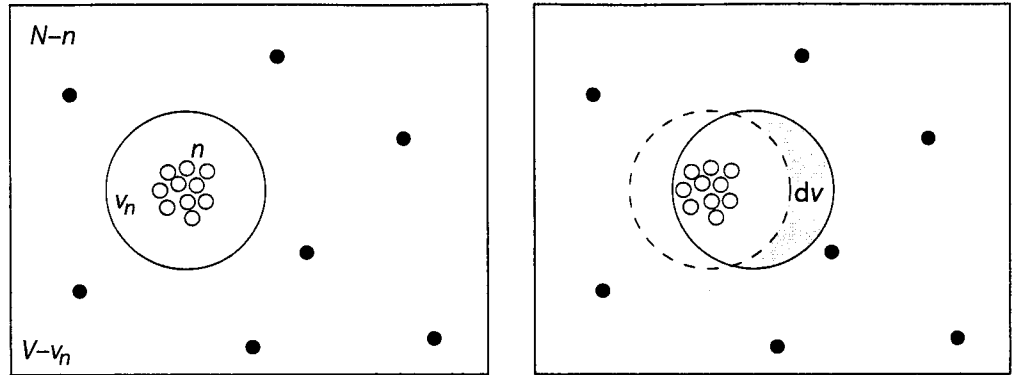| Notation	Meaning
q_n^*	$q_n(v_n^*)$
Q_{N-n}^*	$Q_{N-n}(V - v_n^*)$
$q_n'^*$	$\frac{\partial q_n}{\partial v_n}\big|_{v_n^*}$
$Q_{N-n}'^*$	$\frac{\partial Q_{N-n}}{\partial (V - v_n)}\big|_{v_n^*}$

Figure 2.4: *Left:* System of volume V with the container of volume v_n. Open circles are the n drop molecules; filled ones are the $N - n$ molecules in the vapour. *Right:* Second position of the container, overlapping the original one (dashed). Non-overlapped volume is dv.

In the next important step we allow the drop to be in *one other* location. Again, we wish to know the total partition function Q_n^2 (where the 2 now indicates that this PF includes two drop locations). In the simplest case

$$Q_n^2 = Q_n^1 + Q_n^1 = q_n^* Q_{N-n}^* + q_n^* Q_{N-n}^*. \tag{2.44}$$

In our case, however, the second position is very close to the first one, so that the new and the original drop volume partially overlap. Now, a redundancy problem occurs: certain configurations are 'counted' twice. Figure 2.4 shows such a configuration, in which all drop molecules are in the overlapped volume. An additional condition for a configuration to be redundant is that there are no *vapour* molecules inside the volume created by the two spherical drop volumes.

We will now calculate the partition function of the redundant configurations. The non-overlapped volume is called dv, so the overlapped volume is $v_n^* - dv$. The PF for which all drop molecules are in the overlapped volume is

$$q_n(v_n^* - dv) \approx q_n(v_n^*) - \left.\frac{\partial q_n}{\partial v_n}\right|_{v_n^*} dv, \tag{2.45}$$

using a first order approximation. Similarly, the PF for which all vapour molecules are outside the two drop volumes is

$$Q_{N-n}(V - (v_n^* + dv)) = Q_{N-n}(V - v_n^* - dv) \approx Q_{N-n}(V - v_n^*) - \left.\frac{\partial Q_{N-n}}{\partial(V - v_n)}\right|_{v_n^*} dv. \tag{2.46}$$

The total PF of the redundant configurations is then equal to the product

$$\begin{aligned} Q_{\text{redun}} &= q_n(v_n^* - dv) \times Q_{N-n}(V - v_n^* - dv) \\ &= q_n^* Q_{N-n}^* - q_n^* Q_{N-n}'^* \, dv - Q_{N-n}^* q_n'^* \, dv, \end{aligned} \tag{2.47}$$

where (2.45) and (2.46) have been used and the term proportional to $(dv)^2$ was neglected. The notation was again simplified according to Table 2.2.

Now the size of the redundancy has been found, we return to our task of evaluating Q_n^2. We can now correct Eq. 2.44 by subtracting the PF of all redundant configurations:

$$Q_n^2 = Q_n^1 + Q_n^1 - Q_{\text{redun}}$$
$$= q_n^* Q_{N-n}^* + q_n^* Q_{N-n}^{'*} \, dv + Q_{N-n}^* q_n^{'*} \, dv, \tag{2.48}$$

where we used (2.43) and (2.47). We now continue the drop displacement process and allow it to be in a third position. We keep the displacement distance the same, so that the PF of redundant configurations is the same:

$$Q_n^3 = Q_n^2 + Q_n^1 - Q_{\text{redun}}$$
$$= q_n^* Q_{N-n}^* + 2 \left[dv(q_n^* Q_{N-n}^{'*} + Q_{N-n}^* q_n^{'*}) \right]. \tag{2.49}$$

By now it will be clear what happens: every displacement adds an amount $Q_n^1 - Q_{\text{redun}}$ to the PF; this amount is equal to the terms in square brackets in Eq. 2.49. Every displacement also increases the covered volume of the PF by an amount dv, so that when the entire volume V is covered the PF is given by

$$Q_n^V = q_n^* Q_{N-n}^* + (V - v_n^*)(q_n^* Q_{N-n}^{'*} + Q_{N-n}^* q_n^{'*})$$
$$\approx V(q_n^* Q_{N-n}^{'*} + Q_{N-n}^* q_n^{'*}). \tag{2.50}$$

In the last step it was assumed that $v_n^* \ll V$.

For the purpose of rewriting Eq. 2.50, a quantity p_n (which has the dimension of pressure) is introduced:

$$p_n = kT \left(\frac{\partial \ln q_n}{\partial v_n} \right)_{n,T} = \frac{kT}{q_n} \left(\frac{\partial q_n}{\partial v_n} \right)_{n,T}. \tag{2.51}$$

According to Kikuchi,[8] this p_n may be seen as the outside pressure with which the drop is in equilibrium or the pressure exerted on the container from inside, although Koper and Reiss[13] said that for small systems p_n may not have the meaning of a pressure.

The pressure of the surrounding vapour may be written in a similar form:

$$p = \frac{kT}{Q_{N-n}} \left(\frac{\partial Q_{N-n}}{\partial(V - v_n)} \right)_{n,T}. \tag{2.52}$$

Using the last two equations, the PF in Eq. 2.50 can be rewritten as

$$Q_n^V = q_n^* Q_{N-n}^* V \left(\frac{p_n^*}{kT} + \frac{p}{kT} \right) = q_n^* Q_{N-n}^* \left(\frac{V}{kT/(p_n^* + p)} \right). \tag{2.53}$$

If we compare this with $Q_n^V = Q_n^1 V/\vartheta_n$ (Eq. 2.6), we see that we have obtained the volume scale

$$\vartheta_n^* = \frac{kT}{p_n^* + p}. \tag{2.54}$$

We still need to find p_n^*. This will be done in the next section.

2.2.2 Fluctuation

Our aim is now to relate p_n^* to the volume fluctuations of a drop. We will therefore abandon the idea of a fixed v_n and look at the PF which includes all possible drop volumes. To make the analysis simpler we will fix the drop at a position (that means we will study Q_n^1).

To obtain a drop PF that includes configurations in all possible volumes, it might seem sufficient to integrate:

$$q_n = \int_{\hat{v}_n} q_n(\hat{v}_n)\, d\hat{v}_n. \tag{2.55}$$

However, this result is meaningless. Apart from dimension problems, the q_n's can't simply be summed because every $q_n(\hat{v}_n)$ also includes all configurations present in a volume smaller than $\hat{v}_n$. Instead, we will construct a PF which can be summed because it only contains configurations that have a volume between $\hat{v}_n$ and $\hat{v}_n + dv_n$:

$$\begin{aligned} dq_n(\hat{v}_n) &= q_n(\hat{v}_n + dv_n) - q_n(\hat{v}_n) \\ &= q_n(\hat{v}_n) + \partial q_n/\partial v_n|_{\hat{v}_n} dv_n - q_n(v_n) = \partial q_n/\partial v_n|_{\hat{v}_n} dv_n. \end{aligned} \tag{2.56}$$

For every $dq_n(\hat{v}_n)$, the PF of vapour molecules is $Q_{N-n}(V - \hat{v}_n)$. The total PF of all possible v_n is[†]

$$Q_n^1 = \int dq_n(\hat{v}_n)\, Q_{N-n}(V - \hat{v}_n) = \int \frac{p_n(\hat{v}_n)}{kT} q_n(\hat{v}_n) Q_{N-n}(V - \hat{v}_n)\, d\hat{v}_n. \tag{2.57}$$

In the last step, (2.56) and (2.51) were used. Appendix E shows how $Q_{N-n}(V - \hat{v}_n)$ can be moved out of the integral, giving

$$Q_n^1 = Q_{N-n}(V) \int \frac{p_n(\hat{v}_n)}{kT} q_n(\hat{v}_n)\, e^{-p\hat{v}_n/kT}\, d\hat{v}_n. \tag{2.58}$$

At this point RKK point out that the integral in (2.58) is the PF for a constant pressure ensemble, in the form as Koper and Reiss[13] derived. The consequence of this is that the integrand can be seen as a probability density of observing a certain v_n. Our goal is to determine p_n^*, that is, $p_n(v_n^*)$. The volume v_n^* is the average volume of the fluctuating droplet, which we will approximate by the most probable volume. By definition, the probability density has a maximum at the most probable volume, so the derivative of the integrand with respect to v_n is zero there. This eventually gives

$$kT\, \partial p_n/\partial v_n|_{v_n^*} + p_n^{*2} - p\, p_n^* = 0. \tag{2.59}$$

The authors now eliminate $\partial p_n/\partial v_n|_{v_n^*}$ by defining the isothermal compressibility to be

$$\kappa^* = -\frac{1}{v_n^*} \left(\frac{\partial v_n}{\partial p_n} \right) \bigg|_{v_n^*}, \tag{2.60}$$

[†]This can be derived more rigorously, with the overlapping method used in the previous section. Instead of covering the volume V by translating the container, the volume is covered by expanding it. If the sum of a PF with a cluster volume $\hat{v}_n$ and a PF with a slightly larger one $\hat{v}_n + dv_n$ is calculated, the number of additional, non-redundant configurations proves to be $Q_{N-n}(V - \hat{v}_n)\, \partial q_n/\partial v_n|_{\hat{v}_n} dv_n$, the first integrand in Eq. 2.57.

which leads to the quadratic equation

$$p_n^{*2} - p \, p_n^* - kT/\kappa^* v_n^* = 0,$$ (2.61)

with solution

$$p_n^* = \frac{p}{2} + \sqrt{\frac{p^2}{4} + \frac{kT}{\kappa^* v_n^*}}.$$ (2.62)

For drops which are not too large, the second term under the square root is much larger than the first, so that

$$p_n^* \simeq \sqrt{\frac{kT}{\kappa^* v_n^*}} \gg p.$$ (2.63)

The aim of this section (finding an expression for p_n^*) has now been achieved, so we substitute the result Eq. 2.63 into the expression for the volume scale Eq. 2.54:

$$\vartheta_n^* = \frac{kT}{p_n^* + p} \simeq \frac{kT}{p_n^*} = \sqrt{kT\kappa^* v_n^*}.$$ (2.64)

2.2.3 Problems of the RKK theory

There are some difficulties in the RKK theory, which are related to the drop PF, $q_n(v_n)$, and its constraints. By definition

$$q(n, v, T) = \sum_\nu e^{-E_\nu(n,v)/kT},$$ (2.65)

where the sum is over all microstates ν and the energy of a state with n molecules in a volume v is $E_\nu(n, v)$. Which microstates are allowed, and which ones are not, makes a great difference in the behaviour of the PF, as we will see.

Free cluster   To begin with, we will adopt the constraint that was used in the previous section, namely that the drop molecules must be in a single cluster, but this cluster may be anywhere inside the container. Now consider the PF of a compressible drop, whose volume fluctuates around an average volume called $\bar{v}_n$. If we choose a volume v_n^1 such that $v_n^1 \ll \bar{v}_n$ then the energies of the states in this volume, $E_\nu(n, v_n^1)$, will be very high and therefore $q(n, v_n^1, T)$ will be almost zero. Simply put, the drop cannot be compressed to such a small volume. Conversely, if a volume $v_n^2 \gg \bar{v}_n$ is chosen, the cluster of molecules can be in many positions inside the large container volume, since we did not fix the position of the cluster inside the container. Because the number of possible positions increases as the container volume grows, $q_n(v_n)$ shows a steep increase around $\bar{v}_n$; see Fig. 2.5a, dashed line.

Fixed cluster   We will now look at a second case in which there is an additional constraint: the cluster of drop molecules must be fixed inside the container. One way to implement this is to fix the centre of mass of the cluster at the geometrical centre of the container. Regardless of how it is done, this additional constraint has a great
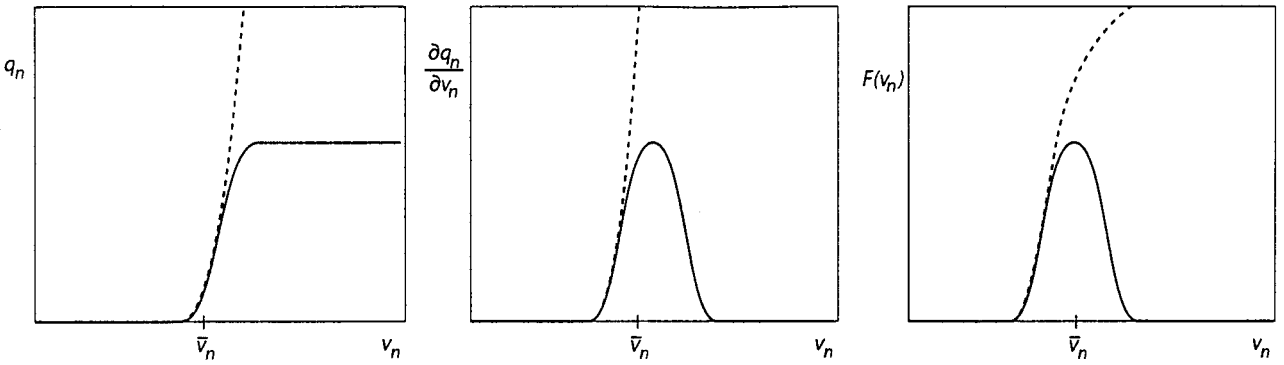
Figure 2.5: Properties of the drop as a function of the container volume v_n, at constant T and n. Dashed line: free cluster; solid line: cluster fixed at the container centre. a: drop partition function q_n; b: derivative with respect to size; c: probability density.

effect on q_n for volumes larger than the average volume: the number of additional configurations available as the volume grows is now much less. Moreover, when v_n is much larger than the average volume, the few additional configurations have a very high energy. The reason can again be stated simply: the drop cannot be 'stretched' to such a large volume. Returning to the overall shape of q_n, it remains constant for larger volumes (recall that q_n is cumulative, i.e., configurations smaller than v_n will still be included); see Fig. 2.5a, solid line.

Fluctuation and most probable volume

What we try to do in the fluctuation analysis of section 2.2.2 is to find out how probable a certain v_n is. To do so, we construct a partition function dq_n of all configurations having a certain v_n and not including smaller ones. The dq_n is proportional to $\partial q_n / \partial v_n$ (see Eq. 2.56). In the case of a free cluster, it is simply a steep function of v_n at $v_n \gtrsim \bar{v}_n$; see Fig. 2.5b, dashed line. The second case is much more physical, showing a Gaussian-like curve centred on $\bar{v}_n$ (Fig. 2.5b, solid line). This function already looks like the probability of a certain v_n, but we did not consider the influence of the surrounding vapour, which is what we will do now.

In section 2.2.2 the constant pressure ensemble (CPE) was already mentioned and we will now study it in more detail. In the form as derived by Koper and Reiss, the normalized probability density F_n of observing a certain v_n is

$$F_n(v_n, n, p, T) = \frac{F(v_n, n, p, T)}{\int_{\hat{v}_n} F(\hat{v}_n, n, p, T)\, d\hat{v}_n}, \tag{2.66}$$

where the denominator is the partition function of the constant pressure ensemble, and F is the 'non-normalized' probability density:

$$F(\hat{v}_n, n, p, T) = \frac{p_n(\hat{v}_n)}{kT} q_n(\hat{v}_n)\, e^{-p\hat{v}_n/kT} = \left.\frac{\partial q_n}{\partial v_n}\right|_{\hat{v}_n} e^{-p\hat{v}_n/kT}. \tag{2.67}$$

Ine last step we used the definition of p_n (Eq. 2.51).

Fixed cluster   When $p = 0$, the probability density is simply equal to the derivative of q_n discussed before. For nonzero pressures, the probability density is this derivative

multiplied by an exponential factor. The effect of this factor on the PF is that the most probable volume is slightly less than the value in vacuum, i.e., the drop becomes smaller. This is easily understandable if we realize that the drop is being hit by vapour molecules from all sides, compressing it. Figure 2.5c shows the probability density for this case (solid line).

Free cluster   In the case of a free cluster the exponential factor creates a maximum at some (probably large) volume (Figure 2.5c, dashed line). This happens because $\partial q_n / \partial v_n$ rises typically with some power of v_n, so the exponential term dominates in the limit of $v_n \to \infty$. The maximum, however, has no real physical meaning, and may be far from the natural volume of the cluster.

The objective of the fluctuation analysis was to find the most probable volume of the cluster of molecules, and then find the value of p_n at that volume. It is clear that if we allow the cluster to be anywhere, the p_n evaluated at the maximum of $F(v_n)$ has nothing to do with $p_n(v_n^*)$ which we need. In contrast, when we fix the cluster, the maximum of $F(v_n)$ does seem to be at the natural volume of the cluster.

Another way to visualize the problem is to look at the configurations that are allowed. Recall that $dq_n(v_n)$ should be a measure of configurations that have a volume v_n. But, if the cluster is not centred, configurations such as the second one from the left in Fig. 2.3 are counted as having the container volume v_n, although the cluster itself is much smaller.

Compressibility

Even if we consider a partition function of centred configurations in the fluctuation analysis, there is an additional problem in finding $p_n(v_n^*)$. At the most probable volume, Eq. 2.59 is valid. This equation, however, contains a derivative of p_n (evaluated at v_n^*) which is unknown. RKK introduce a somewhat questionable interpretation of the isothermal compressibility κ, as shown in Eq. 2.60. Basically there is nothing wrong with defining a new quantity as RKK do; the problem is that κ is considered constant and equal to the compressibility of the bulk liquid (even though this is never explicitly stated).

Summary

In order to determine $p_n(v_n^*)$ where v_n^* is the average volume of the bulk liquid, the PF must be constrained to configurations that are centred in the container. In the case of centred configurations, double counting does not occur, and it is therefore impossible to determine the volume scale in the way presented here. Another way to put the problem is that the first part gives the volume scale ϑ_n in terms of the 'non-centred' $p_n(v_n^*)$, whereas the second part can only provide us with the 'centred' $p_n(v_n^*)$. One can of course proceed and just use the p_n of the second part in the results of the first part, hoping that the difference between the two p_n's is small. In that case it is unclear what the error is that we make.

2.3 Kashchiev's thermodynamically consistent theory

The recent theory of Kashchiev[14] does not result in a new volume scale or cluster distribution, but is centred on the work of formation. Specifically, only the work of formation of a *critical* cluster is considered. Kashchiev tried to find a better expression for this quantity by solving two problems of the classical approach.

The first problem is that the capillarity approximation uses the equilibrium surface tension, even for very small clusters. The new theory is constructed in such a way that for all cluster sizes, the surface energy is equal to its equilibrium value by definition. A second problem that is solved is that the classical theory does not take into account the influence of the spinodal, the stability limit of a phase.

We start the derivation with the general expression for the work of formation, Eq. 2.8. Since a critical cluster has a chemical potential equal to that of the vapour, that equation becomes

$$W_n = -v\Delta p + \sigma a, \tag{2.68}$$

or, as a function of the radius r

$$W = -\tfrac{4}{3}\pi r^3 \Delta p + 4\pi r^2 \sigma. \tag{2.69}$$

The real cluster is a density fluctuation which does not have a sharp interface. The location of the thought cluster interface is therefore arbitrary, and we are free to choose it. Gibbs, who was the first to study models like this, called the hypothetical surface the *dividing surface* (DS).

Besides the choice of the DS, there are two other parameters that need to be defined: the density and pressure of the cluster. In the capillarity approximation, both are uniform throughout the spherical cluster volume. One could question which values we should take for those quantities. According to Gibbs, the density and pressure must be chosen such that the bulk new phase has the same chemical potential and temperature as the old phase. Returning to Eq. 2.69, we see that the previous condition determines Δp. The work of formation itself, W, is a physical quantity and does not depend on the choice of a DS. Therefore, the only free parameters are r and σ, and the relationship between them depends on the DS that we choose.

Surface of tension

This DS, indicated by subscript t, is chosen in such a way that the Laplace equation (Eq. 2.11) is satisfied, which relates r_t to σ_t and Δp. The problem is that the exact dependence of σ_t and r_t on p and T cannot be directly derived, so that we have to approximate one or both of these parameters. Classically, σ_t is approximated by σ_0, the equilibrium surface tension.

Conservative dividing surface

The insight of Kashchiev is that if we choose a value for σ, then Eq. 2.69 defines r. Kashchiev chooses the most convenient definition:

$$\frac{d\sigma_c}{dr_c} = 0. \tag{2.70}$$

so that σ_c is independent of r_c. We are free to choose the value of σ_c, and take $\sigma_c = \sigma_0$. However, since nucleation often takes place at conditions far from equilibrium, where σ_0 is known experimentally, the surface tension has to be extrapolated. Kashchiev lists two possibilities:

$$\sigma_c(p, T) = \sigma_0[p_s(T), T] : \quad \text{isothermal extrapolation, and} \tag{2.71}$$

$$\sigma_c(p, T) = \sigma_0[p, T_{\text{eq}}(p)] : \quad \text{isobaric extrapolation.} \tag{2.72}$$

Here, $p_s(T)$ is again the equilibrium vapour pressure, and $T_{\text{eq}}(p)$ is the inverse function of $p_s(T)$.

The next task is to find an expression for r_c. Like the case with the surface of tension, the exact dependence of r_c on p and T is unknown. However, we can construct an expression for r_c that is consistent with the known behaviour in two limiting cases. Kashchiev proves that in the limit of a large drop, when Δp goes to zero, the Laplace equation is valid:

$$r_{c,0} = \frac{2\sigma_0}{\Delta p}. \tag{2.73}$$

At the spinodal ($p = p_{\text{sp}}$), thermodynamics requires that W vanishes. Setting $W = 0$ in Eq. 2.69 gives

$$r_{c,\text{sp}} = \frac{3\sigma_0}{\Delta p_{\text{sp}}}, \tag{2.74}$$

in which Δp_{sp} is Δp evaluated at the spinodal.

Interpolation

A formula for r_c that interpolates between the limits $\Delta p \to 0$ (Eq. 2.73) and $\Delta p \to \Delta p_{\text{sp}}$ (Eq. 2.74) is

$$r_c = \frac{2\sigma_0}{\Delta p} + \frac{\sigma_0}{\Delta p_{\text{sp}}}. \tag{2.75}$$

Substituting the interpolated r_c in Eq. 2.69 gives

$$W = \frac{16\pi}{3} \frac{\sigma_0^3}{\Delta p^2} \left(1 - \frac{3\Delta p^2}{4\Delta p_{\text{sp}}^2} - \frac{\Delta p^3}{4\Delta p_{\text{sp}}^3} \right) \tag{2.76}$$

$$\approx \frac{16\pi}{3} \frac{\sigma_0^3}{\Delta p^2} \left(1 - \frac{\Delta p^2}{\Delta p_{\text{sp}}^2} \right). \tag{2.77}$$

Both formulas for the energy to form a nucleus are *thermodynamically consistent* because their behaviour is correct in the entire Δp range from 0 to Δp_{sp}, so for a nucleus of any size.

Nucleation rate

Using the work of formation W from Eq. 2.77, Kashchiev shows that the nucleation rate $J = A \exp(-W/kT)$ is

$$J = A \exp \left(\frac{16\pi}{3} \frac{\sigma_0^3}{kT\Delta p_{\text{sp}}^2} \right) \exp \left(-\frac{16\pi}{3} \frac{\sigma_0^3}{kT\Delta p^2} \right), \tag{2.78}$$

where A is a kinetic factor. In the case of nucleation of a liquid in a vapour, Kashchiev derives that

$$J = A \exp\left[-\frac{16\pi}{3} \left(\frac{M}{N_A \rho_\ell \ln S} \right)^2 \left(\frac{\sigma_0}{kT} \right)^3 \right] \exp\left[\frac{16\pi}{3} \left(\frac{M}{N_A \rho_\ell \ln S_s} \right)^2 \left(\frac{\sigma_0}{kT} \right)^3 \right],$$

(2.79)

where $S_s(T) = p_{sp}(T)/p_s(T)$. The first exponential factor is the same as in classical theory; the other exponential factor is a temperature-dependent correction.

Comments on Kashchiev's theory

One of the important parameters in the thermodynamically consistent theory is the spinodal pressure of the old phase; in our case the vapour spinodal pressure. A spinodal line separates metastable regions $[(\partial p/\partial V)_T < 0]$ and unstable regions $[(\partial p/\partial V)_T > 0]$. In a p-V diagram, the points at which an isotherm has zero slope form the spinodal line; the spinodal pressure is defined by $(\partial p/\partial V)_T = 0$.

It is not entirely certain if we can speak about a spinodal in the case of nucleating vapours. Since, as Kusaka[15] puts it, 'sharply defined spinodal is an artifact of mean-field theory', e.g., van der Waals-like equations of state, it is uncertain if the notion of a spinodal can be used in the description of non-ideal vapours. We could try to experimentally define the spinodal by isothermally compressing a vapour and measuring at which pressure and density $\partial p/\partial \rho = 0$. Unfortunately, nucleation sets in long before we would arrive at the hypothetical spinodal, so it seems to be experimentally unreachable.

Should the work at formation vanish at the spinodal? In model systems that can reach spinodal (nucleation is impossible in such models) it is seen that relatively large-scale fluctuations occur, with a diffuse boundary. This so-called 'spinodal decomposition' appears to be very different from nucleation. Although the fluctuations leading to spinodal decomposition probably have zero work of formation, it is unclear whether this is also true for the formation of a critical cluster.

On a molecular level, the ultimate limit of stability could be better defined by the conditions at which a single molecule becomes a critical cluster, so that the work of formation as a function of the cluster size monotonically decreases and there is no energy barrier towards the formation of the new phase. Since according to the Nucleation Theorem[3]

$$\left(\frac{\partial \ln J}{\partial \ln S} \right)_T \approx n^*,$$

(2.80)

where n^* is the number of molecules in the critical cluster, this stability limit would be characterized by a very low slope of isotherms in the $\ln J$ versus S plot.

3. Properties of water

In the previous chapter, we derived expressions for the nucleation rate as a function of substance properties such as liquid density, surface tension and vapour pressure. In this chapter we review the experimental data that is available for those properties of water. We will also look at several models, including a recent one developed by J. Hrubý and the current author, which is described in section 3.5.

3.1 Density

It is well known that the density of water has a maximum value near 4 °C, and decreases from this maximum down to the freezing point. In fact, before 1964 this maximum was used to define the millilitre as the volume of 1 gram of water at the maximum density.[16] What is not so well known is that the density of supercooled water keeps decreasing as temperature goes down and that it becomes a very steep function of temperature.

It is easy to imagine that it is quite difficult to perform experiments on liquid water below the freezing point. Still, as early as the nineteenth century, experimenters succeeded in measuring the density down to about −10 °C. In the following century, the techniques to keep water liquid below 0 °C were improved; even so, not until in the 1960s real progress was made.

In most modern experiments, water was boiled and distilled, then thoroughly cleared capillaries were filled and flame sealed. After sealing, the tube contained liquid water and a volume of water vapour. Then, the position of the meniscus was measured at different temperatures. Usually, the tube was calibrated by making a measurement at two or more temperatures above 0 °C for which the density was accurately known.

It was found that the water could remain liquid at lower temperatures if the capillary diameter was smaller, and it is not surprising that three of the early experiments reaching −34 °C or lower were done using capillaries with an inside diameter of 4 μm. In the 1980s it became clear that the capillary diameter also influenced the properties of water itself, including the density. Specifically, a small capillary resulted in an excess density, when compared to the bulk value. C. M. Sorensen[17] began using larger capillaries, but was unable to reach temperatures under −25 °C. Finally, Hare and Sorensen[18] succeeded in cooling samples with an inside diameter of 300 μm down to −33 °C by using a special method to make very clean samples. They were also able to estimate the magnitude of the excess density effect and showed that it was within the experimental error, in their experiments.

At this time the Hare and Sorensen data seems to be the best available, representing the bulk liquid water density down to the lowest possible temperature that can be reached experimentally. For $T < -33$ °C we have to extrapolate the density, which is not as easy as it seems. The problem is that when the temperature decreases, the
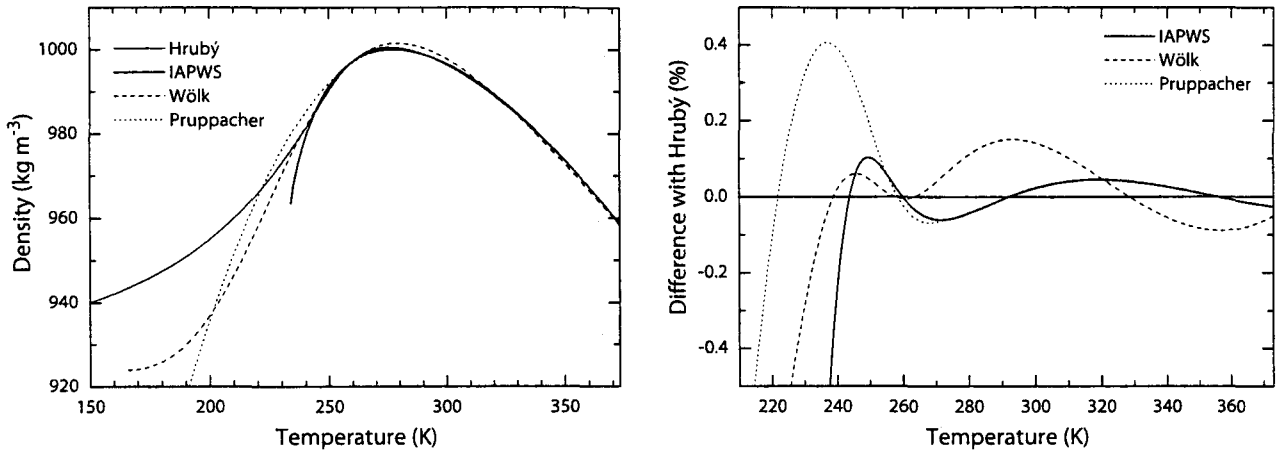
Figure 3.1: Left: density of water as a function of temperature. Right: differences of the models relative to the to the Hrubý model.

density versus temperature curve becomes very steep. In fact, when the expansivity $\alpha = -\rho^{-1}(\partial\rho/\partial T)_p$ is extrapolated, it seems to become infinite at some temperature near -45 °C. At this singular temperature (T_s), the density would then of course be an infinitely steep function of T, and extrapolation below T_s becomes impossible. According to some workers, notably Speedy and Angell,[19] T_s is a limit of stability, or spinodal, below which the normal form of liquid water simply does not exist. This hypothesis is supported by the fact that many other properties of water also seem to diverge at the same T_s.

The IAPWS95 formulation[20] is an extensive equation of state for water, that reproduces many properties to within the experimental error, in the entire temperature range where measurements have been made. It even reproduces the Hare and Sorensen data, although the equation of state is then used far below its lower limit of validity, which is the freezing point. The lowest temperature at which it can be evaluated is 233.56 K, several degrees below the lowest temperature of experimental data. An investigation by this author showed that this limit is caused by a spinodal; the slope of the density versus temperature curve is infinitely high. Another way to put this is that according to the IAPWS model, the spinodal pressure of water increases as temperature goes down, reaching atmospheric pressure at 233.56 K. Therefore, the IAPWS equation seems to support Speedy and Angell's stability limit conjecture.

However, there is some doubt whether this limit of stability really exists. There are nucleation experiments in which liquid water is believed to be formed, at temperatures far below T_s.[12,21] There are theories in which it is assumed that liquid water is connected to an amorphous form of ice, also called 'glassy water', that exists below 130 K.[22]

A physically reasonable assumption is then that as water is cooled, it becomes more and more ice-like, and approaches a state similar to amorphous ice. Among the models based on this assumption are the 'mixture models', in which it is assumed that water is a mixture of two components with different partial volumes (by mass) $v_1(T)$ and $v_2(T)$. In the mixture model by Vedamuthu et al.,[23] the specific volume is then $v(T) = f(T)v_1(T) + [1 - f(T)]v_2(T)$. Here $f(T)$ is the mass fraction of

one component, whose value was determined by fitting the model to accurate density measurements by Kell[24]. Unfortunately, the model was not meant to be used below 225 K, where the mass fraction f becomes larger than unity.

Another model that has been used frequently[2,25–28] is the fit given by Pruppacher and Klett[29] at temperatures as low as 200 K. Pruppacher and Klett mention that they fitted their function, which is a parabola, 'to the experimental data of Dorsch and Boyd (1951)', and give a validity range of −50 °C to 0 °C. An investigation by the current author revealed that Dorsch and Boyd[30] did not measure density, but included a graph of Mohler's data[31] of 1912; second, Mohler's data only go down to −13 °C. Furthermore, Kell[16] mentions that Mohler's results are high relative to values found by others and that they have therefore 'been eliminated from further consideration'. Figure 3.1 shows that the Pruppacher and Klett fit is indeed higher than the IAPWS data for temperatures lower than 255 K. Apparently, the fit by Pruppacher and Klett is of limited value.

Like the two-state models, the density fit employed by Wölk et al.[12] tries to account for the ice-like behaviour of supercooled water at low temperatures. Their fit includes a term which scales the density depending on how far the temperature is from the critical temperature, and a tanh term which accounts for the step-like change from liquid water to amorphous ice. In Figure 3.1, the Wölk model is seen to decrease strongly – although not as steeply as the IAPWS model – and then reaches a constant value at about 165 K.

Finally, we note that the differences between the models are quite large in the range where we will need them, 200–240 K. For the evaluation of nucleation theories, we choose the Hrubý model.

3.2 Surface tension

The surface tension of supercooled water is about as difficult to measure as its density. Despite the importance of accurate surface tension data for the validation of nucleation theories, only two measurements series have been published: one in 1951 by Hacker[32] and the second in 1990 by Floriano and Angell.[33]

In his report, Hacker mentions two problems which complicate surface tension measurements: First, most methods require a knowledge of the liquid density (which, at that time, was not known for highly supercooled water) and second, some methods need a large value of liquid to be supercooled, which increases the probability of freezing. The method Hacker used circumvents both problems. He placed water at the end of an open capillary (diameter 364 μm) and measured the pressure that was needed to flatten the meniscus at that end. The applied pressure is proportional to the surface tension. Because of the amount of data collected (702 measurements in the temperature range 27 °C to −22.2 °C), the uncertainty in Hackers final (averaged) results is quite low: 0.08%.

Nearly forty years later, Floriano and Angell[33] measured the surface tension of supercooled water, mainly because they were unaware of Hacker's results and wanted to 'remove a deficiency' in the knowledge of water. These authors used a method that was totally different from Hacker's, namely the capillary rise effect. This well-known effect (the rise of water inside a small vertically placed capillary) is caused by
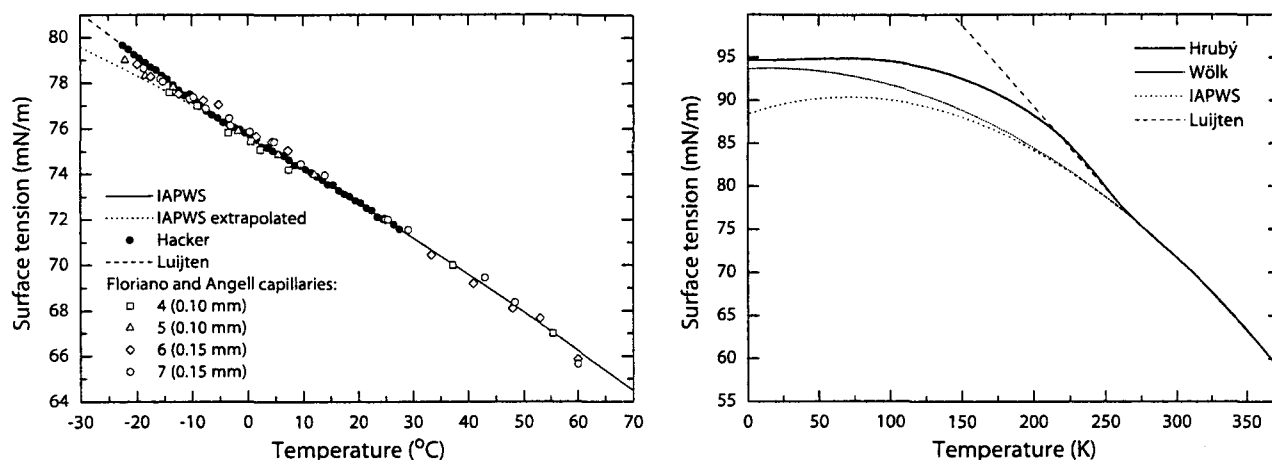
Figure 3.2: Surface tension of water; experimental data and models.

the pressure difference that exists across a curved meniscus. The amount the water rises is proportional to the surface tension and also depends on the density. The latter parameter was known with sufficient accuracy by 1990, solving Hacker's first problem. The second problem was solved by only cooling the uppermost 1 cm of the water column (this can be done because the force producing the capillary rise is located at the water surface).

Floriano and Angell made much fewer measurements than Hacker (63 in the temperature range 60 °C to −27.2 °C) and used capillaries with an inside diameter ranging from 73 μm to 299 μm. The results of Hacker and of Floriano and Angell are shown in Figure 3.2.

In Hacker's data there seems to be a point near −5 °C where the slope abruptly changes. Floriano and Angell's results do not seem to support this 'kink' although the scatter is too large to draw a definitive conclusion.

The IAPWS release on Surface Tension of Ordinary Water Substance[34] recommends an equation for the temperature range of 0.01 °C to the critical temperature. It can be seen that down to −5 °C there is agreement with both experimental data sets. Below −5 °C, Hacker's data clearly deviates from the IAPWS equation. Luijten[2] assumed that the surface tension would continue to increase with decreasing temperature, with the same slope as the part of Hacker's results below −5 °C. Luijten's linear fit is also shown in Figure 3.2. It appears that Luijten's fit leads to unlikely large surface tension values at low temperature. Furthermore, it does not satisfy the thermodynamic constraint of a vanishing temperature derivative at 0 K, which was proposed by Lamanna.[27] In contrast, the fit used by Wölk et al.[12] does satisfy the constraint and agrees well with the IAPWS data above 240 K (Fig. 3.2), but like the IAPWS equation it does not reproduce the change of slope of Hacker's data.

In our experimental temperature range, 200–240 K, there is not much difference between Luijten's fit and the values from the Hrubý model. To be consistent, we choose the latter for the evaluation of nucleation theories.
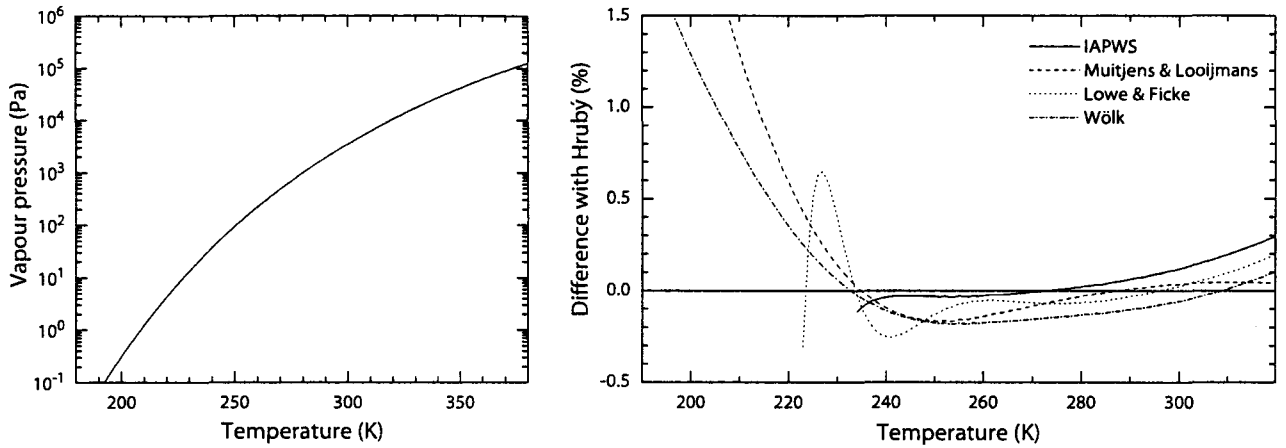
Figure 3.3: Vapour pressure as a function of temperature. Left: vapour pressure according to all models (differences are not visible on this scale). Right: differences of the models, relative to the Hrubý model.

3.3 Vapour pressure

The vapour pressure is the pressure that exists over a liquid when it is in equilibrium with its vapour; the vapour pressure is a function only of temperature; see Fig. 3.3. Although it can be measured directly, some expressions are based on the Clausius-Clapeyron equation, which reads

$$\frac{\mathrm{d}p_v(T)}{\mathrm{d}T} = p_v(T)\frac{L(T)}{RT^2}. \tag{3.1}$$

when ideal gas behaviour is assumed. Here p_v is the vapour pressure, L [J mol^{-1}] is the latent heat of phase change and R is the gas constant. Muitjens and Looijmans,[35] who used this equation to obtain the vapour pressure, further assumed that $\mathrm{d}L/\mathrm{d}T$ is constant and equal to $c_{p,v} - c_l$. Eq. 3.1 can then be integrated, yielding

$$p_v(T) = p_v^{\text{ref}} \exp\{[(c_{p,v} - c_l)\ln(T/T_{\text{ref}}) - L_0(1/T - 1/T_{\text{ref}})]/R\}. \tag{3.2}$$

Many authors[25–28] have used Eq. 3.2 with the constants that were determined by Muitjens and Looijmans, but citing Vargaftik[36] as the source. In reality, Vargaftik's book was only used to obtain $p_v^{\text{ref}} = p_v(T_{\text{ref}})$. Wölk et al.[12] used an equation originally given by Wagner[37], which is similar to Eq. 3.2, but additionally includes a term proportional to the temperature in the exponent.

In their book, Pruppacher and Klett[29] show the expression of Lowe and Ficke[38] of 1974, which is a sixth degree polynomial fit of an integration of the Clausius-Clapeyron equation in which the virial equation of state for water vapour was used. The validity range is −50 °C to 50 °C; because of the nature of polynomial fits the expression cannot be extrapolated (it diverges already slightly below −50 °C).

The vapour pressure values that we will use are based on an extended version of the Hrubý model; an extension which is not shown in section 3.5. Therefore, a table of vapour pressure values is given in appendix C. Figure 3.3 shows that in the range where IAPWS vapour pressure data is available, all models agree to within 0.3% with the IAPWS data. Below 234 K, the differences become larger; at 200 K, the deviation
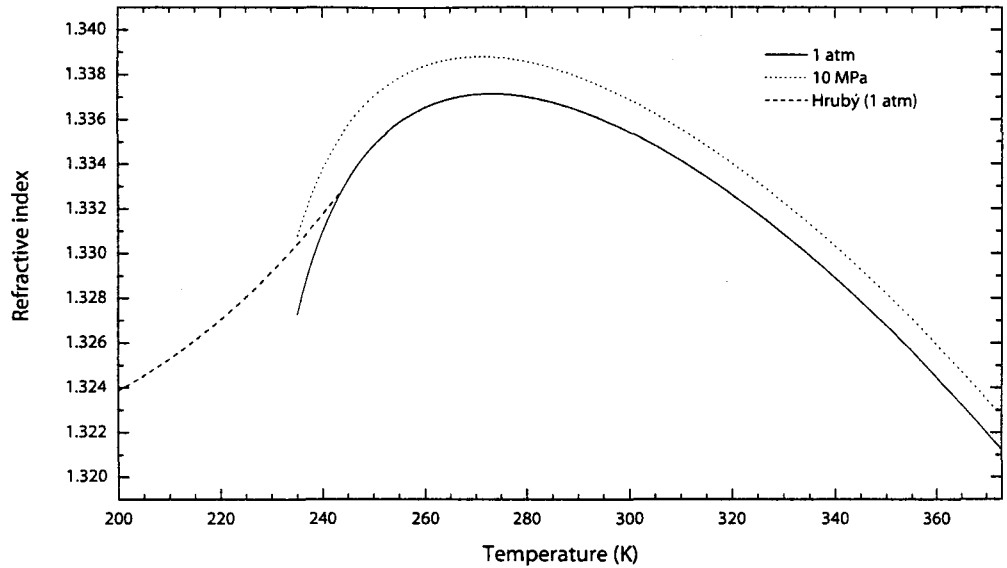
Figure 3.4: Index of refraction of water as a function of temperature, for a wavelength of 514.2 nm. Solid line: using IAPWS density, 101325 Pa; dotted line: IAPWS density, 1 MPa. Dashed line: Hrubý model density, 101325 Pa.

of the Hrubý model from the Wölk fit is 1.3%; the difference with the Muitjens and Looijmans fit is 1% higher. Such differences might seem small, but if the error in the vapour pressure (and therefore also in the supersaturation) is 2.3%, the error in the theoretical nucleation rate can be as high as 70%.

3.4 Index of refraction

Knowledge of the index of refraction is required to calculate theoretical light scattering and extinction by water droplets, quantities that we will need later. Since these processes take place at temperatures at which the refractive index has never been measured, this quantity must be extrapolated.

Although the index of refraction depends on temperature (and also on pressure) most authors[2,25,26,28] simply took a constant value of 1.334. We will now see if this approach is justified.

The IAPWS published a release[39] in 1997 that gives the refractive index as a function of temperature and density, valid for temperatures between -12 °C and 500 °C. To include the dependence of density on temperature and pressure, it must be used in combination with the density values of the IAPWS 95 formulation.[20]

In Figure 3.4 the refractive index of water is shown, at atmospheric pressure (101325 Pa), for a wavelength of 514.2 nm, and using the IAPWS density (solid curve). The IAPWS relation for obtaining the refractive index was used partially outside its validity range. The behaviour looks similar to the IAPWS density curve (Figure 3.1), including the steep decrease at low temperatures.

If the Hrubý model for density is used, the decrease is more gradual (dashed curve), and the refractive index reaches a value of about 1.324 at 200 K, only about 1% lower than the maximum value near 273 K. The influence of pressure is also de-

picted in Figure 3.4; the refractive index has been calculated using IAPWS density values at a pressure of 10 MPa (dotted curve). The difference with the values at atmospheric pressure is only 0.1% to 0.3%, so that the pressure dependence can be safely ignored.

In section 5.4 we will further investigate the effect of the recreative index on the scattering.

3.5   A model for density and surface tension of supercooled water*

A thermodynamic model was developed to predict the density and surface tension of supercooled water (down to the glass transition at 130 K) and amorphous ice (down to 0 K), based on the hypothesis that water is a mixture of a low-density structure and a high-density structure. Below 224 K density and surface tension are predicted for a second liquid/amorphous phase. At 77 K, the computed densities agree with measurements for low- and high-density amorphous ices. A first theoretical interpretation of the surface tension anomaly is given. The observed dependencies of the apparent density and surface tension on the capillary radius are explained qualitatively.

Recent experimental studies[12,21,40] indicate that water nucleates from the vapor phase in the form of liquid nanodroplets at least down to 205 K. The observed dependence of the nucleation rate on temperature is very smooth[†], thus excluding a transition from vapor→liquid to vapor→crystal nucleation. To analyze results by applying nucleation theory, density and surface tension have to be estimated deep in the supercooled regime. Density measurements[18] exist only down to 240 K at atmospheric pressure. Experimental values of the surface tension exist down to 246 K.[33]

The existing accurate analytical representation of thermodynamic properties of water[20,41] (further referred to as IAPWS-95) cannot be used at low temperatures, because it predicts an ultimate lower limit of stability of the liquid phase: the liquid-vapor spinodal retraces the region of positive pressures. At normal pressure ($p_n =$ 101325 Pa), the lower (anomalous) spinodal point is located at 233.6 K and 0.9588 g cm^{-3} (see Fig. 3.5). For the surface tension, the IAPWS also developed an equation[34,42] which is valid only above the triple point ($T_t = 273.16$ K) and does not agree with some experimental data[32] below that temperature.

One of the explanations[22] of the anomalous behavior of supercooled water is that it can exist in two phases: a low-density liquid (LDL), existing at low pressures, and a high-density liquid (HDL), stable at high pressures. Both liquid phases are metastable with respect to hexagonal ice Ih. The phase separation can occur below the hypothesized liquid-liquid critical point (estimated coordinates 220 K and 100 MPa[22]). It is further assumed that LDL is a liquid form of the low-density amorphous ice (LDA); the glass transition occurs at $T_g \approx$ 130 K[‡]. Analogously, HDL is a hypothetical liquid

---

*This section contains the text of an article, written by J. Hrubý and the present author, and has been submitted for publication in Physical Review Letters.

†The opposite conclusion of Peeters et al.[21] was due to an error in data processing; see Labetski et al.[40]

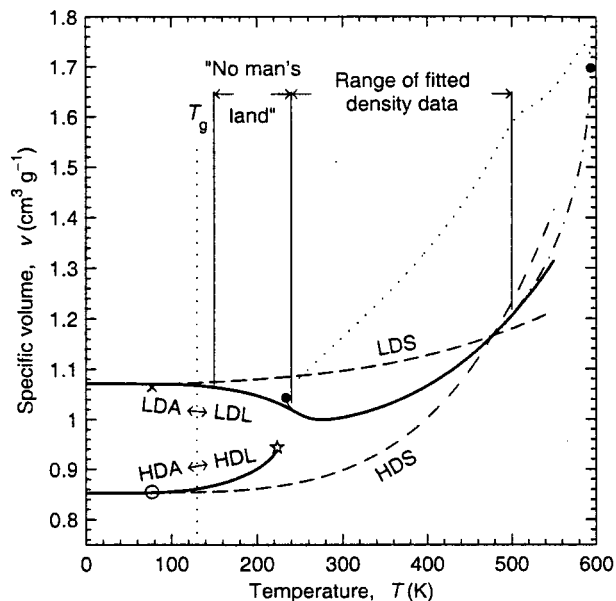‡Recent simulations[45] lead to a suspicion that LDA and LDL are different phases, rather than a

Figure 3.5: Specific volume of liquid and amorphous water at normal pressure. Solid lines: present model (LDL/LDA and HDL/HDA); star: spinodal point (HDL→LDL); dashed lines: pure low- and high-density structures. Dash-dotted line: IAPWS-95 formulation;[41] filled circles: spinodal points (liquid→vapor); connecting dotted line: unstable solution ($\partial p/\partial v > 0$). Cross and open circle: experimental volume of LDA and HDA, respectively.[43,44] In the 'no man's land' experiments on the liquid phase are impossible. T_g is the glass transition temperature.

form of the high-density amorphous ice (HDA).

The present model is related to the family of two-state models.[23,46–48] We assume that liquid and amorphous water consist of two incompatible structures: a low-density structure (LDS) and a high-density structure (HDS). The LDA/LDL phase is rich in LDS, and the HDA/HDL phase is rich in HDS. At any instant of time, a molecule is a member of either the low-density structure or the high-density structure. The composition can be given by the structural fraction x, defined as

$$x = \frac{N_{HDS}}{N_{LDS} + N_{HDS}} = \frac{\text{number of HDS members}}{\text{total number of molecules}}.\tag{3.3}$$

We adopt the simplest model for the specific volume, namely, a molar average of the "components":

$$v = (1 - x)v_{LDS} + x\, v_{HDS}.\tag{3.4}$$

We assume that the structures resemble some crystalline forms of ice on the local scale. In particular, we expect that LDS is related to hexagonal ice Ih and cubic ice Ic (0.9313 g cm^{-3} and 0.9343 g cm^{-3}, respectively,[49,50] at 143.15 K). The proximity of LDA and Ic is supported by the fact that LDA relaxes spontaneously into the cubic ice, which relaxes further into the stable Ih ice.[50] However, only for Ih sufficiently accurate data exist. Therefore, we approximate the specific volume of the LDS as the volume of ice Ih: $v_{LDS} \approx v_{Ih}$. We developed a new equation for the volume of ice Ih based on the lattice constants by Röttger *et al.*:[49]

$$v_{Ih,n} = a_1 + a_2 t(1 - y - ty) + a_3 t^2(1 - y)$$
$$+ a_4(1 + t + \tfrac{1}{2}t^2)y + a_5 t^3 y,\tag{3.5}$$

where $t \equiv T/a_6$ and $y \equiv \exp(-t)$; the values of a_1 to a_6 are given in Table 3.1. Eq. (3.5) is plotted in Fig. 3.5 (labeled LDS). It satisfies the theoretical requirement

glassy and liquid form of a single phase.

of vanishing first and second derivatives with respect to T at 0 K. Furthermore, at 71 K it reproduces the experimentally observed weak minimum of the specific volume of ice Ih (in Röttger et al.[49] located at 73 K). At high temperatures Eq. (3.5) reduces into a parabola, enabling a plausible extrapolation.

We expect the high-density structure to be related to some high-pressure crystalline ices. Because it is not clear which particular crystalline structure (if any) corresponds to HDS, no a priori choice was made for the specific volume of HDS. We assumed it in the form

$$v_{\text{HDS,n}}/b_1 = 1 + (T/b_2)^{b_3},\tag{3.6}$$

where b_1, b_2, b_3 are unknown parameters.

The water molecules are free to join LDS or HDS. For a given temperature T and pressure p, the structural fraction x_ϕ corresponding to a thermodynamic phase ϕ can be found as a local minimum of a Gibbs function:

$$\partial g(p,T,x)/\partial x\big|_\phi = 0, \quad \partial^2 g(p,T,x)/\partial x^2\big|_\phi > 0,\tag{3.7}$$

where ϕ = LDA/LDL or HDA/HDL. We developed an approximate Gibbs function $g(T,p,x)$ based on the following arguments: (i.) The molecules can be considered as $N = N_{\text{LDS}} + N_{\text{HDS}}$ sites of a lattice, occupied by either LDS or HDS members. The number of different configurations is $N!/(N_{\text{LDS}}!N_{\text{HDS}}!)$. (ii.) The probability that a molecule is a HDS member does not depend on the memberships of the neighbors. (This is a crude approximation, because we expect that especially at low temperatures clusters or networks of the dislike structures exist.) Then the mean potential energy of the system is $\frac{1}{2}Nc[(1-x)^2 u_{11} + 2(1-x)xu_{12} + x^2 u_{22}]$, where c is the number of neighbors and u_{11}, u_{12}, u_{22} are mean energies of the LDS-LDS, LDS-HDS, and HDS-HDS interactions, respectively. At normal pressure, the resulting Gibbs function can be written as

$$
\begin{aligned}
g_n(T,x) &= g_{\text{LDS,n}}(T) + R\left(h_{1\text{n}}x + h_2 x^2\right)\\
&\quad + RT\left[(1-x)\ln(1-x) + x\ln x\right].
\end{aligned}\tag{3.8}
$$

The function $g_{\text{LDS,n}}(T)$ (Gibbs free energy of pure LDS at normal pressure) has no significance for this study. For a general pressure the Gibbs function is obtained as

$$g(p,T,x) - g_n(T,x) = \int_{p_n}^{p} v\,\mathrm{d}p' \approx v_n(T,x)\,(p - p_n).\tag{3.9}$$

The last approximation neglects the compressibility of the structures.

A comprehensive study based on a Gibbs function similar to Eq. (3.8) has been elaborated by Ponyatovsky et al.[48] Their model is more complex by considering a finite entropy difference between the HDS and LDS (in their terminology excited and ground states; entropy is given as $-\partial g(p,T,x)/\partial T$). In our derivation we do not find a justification for a considerable entropy difference. In future work, rather a nonideal entropy of mixing should be considered due to a temperature-dependent correlation (weakening with increasing T) of the memberships of neigboring molecules in LDS or HDS.
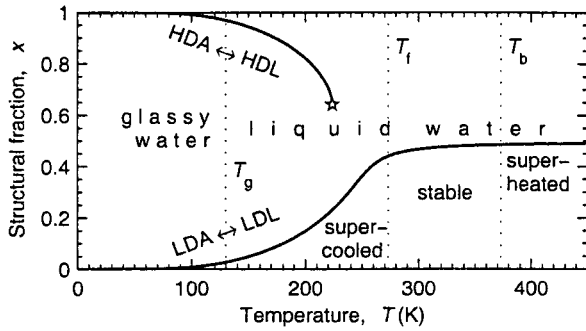
Figure 3.6: Composition of the high-density and low-density phases of water at normal pressure, described by the structural fraction (the fraction of molecules taking part in the high-density structure). T_g, T_f and T_b: temperatures of glass transition, fusion and boiling, respectively.

Condition (3.7) was applied to equation (3.8) to find the structural fraction x_ϕ of the metastable phases. The solution, shown in Fig. 3.6, can be found by iterating equation

$$x_\phi = \left\{1 + \exp[(h_{1n} + 2x_\phi h_2)/T]\right\}^{-1},$$
(3.10)

starting from $x = 0$ for LDA/LDL and $x = 1$ for HDA/HDL. For a general pressure, the same method can be used with $h_1 \approx h_{1n} + (v_{HDS,n} - v_{LDS,n})(p - p_n)$.

The values of the five unknown parameters b_1, b_2, b_3, h_{1n}, and h_2 were obtained by fitting to densities ($\rho \equiv 1/v$) computed from the IAPWS-95 equation of state[20] by Wagner and Pruß[41] in the range 240 to 500 K; see Table 3.1. The fit is within 0.05% except at 240 K where the volume is by 0.1% below IAPWS-95 (Fig. 3.5). The model provides an unexpectedly good approximation of densities at 77 K of the LDA (experiment[43] 0.94±0.02 g cm^{-3}/ model 0.934) and HDA[44] (1.17±0.02 / 1.172).

The above given thermodynamic model is able to represent the main physical features: (a.) The high-density structure has a higher potential energy than the low-density structure. Therefore, LDS is more frequent at low pressures. (b.) Because $v_{HDS} < v_{LDS}$, increasing the pressure leads to a higher population of the high-density structure. (c.) The states for which the structures are mixed have a high potential energy, forming a barrier separating basins (in the configuration space) rich in LDS and rich in HDS. This represents the hypothesis that the two competing structures cannot be combined in some "elegant" manner and that the interface between the microscopic domains, occupied by LDS or HDS, contains unsaturated H-bonds and other defects increasing the potential energy. (d.) At high temperatures, the mixed states are probable because of the combinatorial effect. (The negative of the term in the second line of Eq. (3.8) is $T \times$ entropy of mixing.) At low temperatures, the potential energy prevails, leading to a phase separation.

Above the triple point, the surface tension σ of water is accurately described by the IAPWS correlation.[34,42] Early measurements[51] down to 265 K indicated, that the σ vs. T curve has a second inflection close to the triple point (the first is at 530 K[34]). In 1951, Hacker[32] performed detailed measurements of the surface tension of supercooled water down to 250.95 K. The average values of individual measurements (in total 702) for 1 K intervals as given in Hacker[32] are shown in Fig. 3.7. These measurements indicate an almost sudden change of slope, a "kink", at about 267 K. More recently, Floriano and Angell[33] measured down to 254.35 K using a capillary of internal diameter 0.298 mm (comparable with 0.364 mm of Hacker) and down to
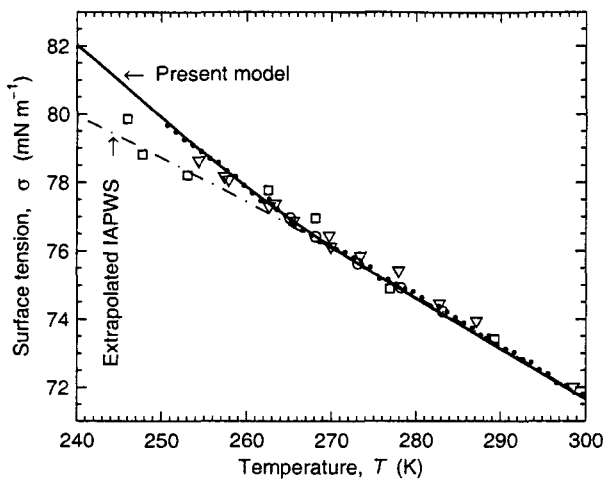
Figure 3.7: Surface tension of water. Solid line: present model. Filled circles: data by Hacker.[32] Squares and triangles: data by Floriano and Angell[33] (capillary diameter 0.077 and 0.298 mm, respectively). Open circles: data from the International Critical Tables.[51] Dash-dotted line: IAPWS equation[34] (valid for T>273 K).

245.95 K with a 0.077 mm capillary. The scatter of the individual 0.298 mm measurements is about the same as the scatter in Hacker's data. However, Hacker averaged the very high number of individual measurements. His averaged data is in excellent agreement with earlier measurements[51] and with the IAPWS correlation above T_t.

Considering water as a mixture of two structures, "components" LDS and HDS, the surface tension can be described with the Macleod-Sugden correlation.[52] Because the density of saturated vapor is much smaller than the density of liquid in the temperature range considered, this relation can be written in the form:

$$\sigma(T,x)\,/c_1 = \left[\, \mathbf{P}(x) \;/\; c_2 v(T,x)\,\right]^n\,. \tag{3.11}$$

Here, x and v are computed for a given temperature using Eqs. (3.4) and (3.10). The normalizing factors c_1, c_2 ensure dimensional consistency of the equation and enable comparison with engineering literature. $\mathbf{P}$ is a parameter called *parachor*. For simple mixtures, we can assume

$$\mathbf{P}(x) = (1 - x)\mathbf{P}_{\text{LDS}} + x\mathbf{P}_{\text{HDS}}\,. \tag{3.12}$$

The values of n, $\mathbf{P}_{\text{LDS}}$, and $\mathbf{P}_{\text{HDS}}$ as shown in Table 3.1 were obtained by fitting the model to data by Hacker (251 to 273 K) and IAPWS (273 K to 373 K). It is remarkable that just three parameters fit the relatively complex curve well within the experimental accuracy.

The model gives the second inflection point at 287.7 K. In addition, there is a third inflection at 248 K. The tangents at the inflection points intersect at 263 K, which can be considered as the location of the kink. The interpretation of the kink is that (i.) the hypothetical pure HDS has a significantly lower surface tension than the hypothetical pure LDS, (ii.) the structural fraction rapidly changes in favor of LDS upon cooling. Fig. 3.8 shows the extrapolation of the surface tension down to 0 K, where it becomes flat. Also shown is the prediction of the surface tension for the dense phase HDL/HDA.

As shown in Fig. 3.7, the 0.077 mm data by Floriano and Angell follow the smooth extrapolation of the IAPWS correlation. Although this data is not quite conclusive, it seems that this observation is related to the so far unexplained dependence of the
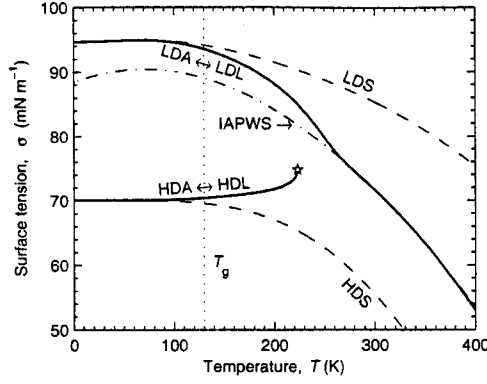
Figure 3.8: Prediction of surface tension of liquid and amorphous water in a broad temperature range.

Table 3.1: Model parameters.

a_1 (m^{3}kg^{-1})	1.21779×10^{-3}	b_1 (m^{3}kg^{-1})	8.5266×10^{-4}
a_2 (m^{3}kg^{-1})	-4.33629×10^{-5}	b_2 (K)	607.66
a_3 (m^{3}kg^{-1})	4.38031×10^{-6}	b_3	4.1571
a_4 (m^{3}kg^{-1})	-1.46258×10^{-4}	P_{LDS}	52.9316
a_5 (m^{3}kg^{-1})	-9.88480×10^{-6}	P_{HDS}	39.4034
a_6 (K)	55.83	n	4.511
h_{1n} (K)	493.99	c_1 (N m^{-1})	10^{-3}
h_2 (K)	-486.47	c_2 (kg m^{-3})	18015.268

Note: c_2 is numerically equal to $10^3 M$, $M = 18.015268$ kg/kmol[41]

apparent density on the capillary diameter. Hare and Sorensen[18] indicated that this dependence could be explained by a surface layer of higher density, whose thickness increases as temperature is decreased.

Using Gibbsian surface thermodynamics[53] we found that (according to the present model) the surface layer is indeed enriched with the dense structure (HDS). Although this was computed for the liquid-vapor interface, we assume that the results are also applicable to the liquid-glass interface, because the thickness of the surface layer would be much larger than the reach of intermolecular forces. The surface enrichment explains qualitatively the apparent dependencies of both density and surface tension on the capillary diameter. A quantitative explanation was not achieved; the computed effects are too small. The "watery" ($x \approx 0.5$) surface layer of the "icy" ($x \rightarrow 0$) supercooled water might be related to the phenomenon of liquid-like surface of ice Ih.[54]

4. Experimental methods

Our experiments were based on the nucleation pulse method, which limits the formation of droplets to a short period of time (10^{-4} s) with known thermodynamic conditions, called the pulse. After the pulse, the droplets grow to a detectable size ($d \gtrsim 0.5$ µm); during this growth period the conditions are such that no new droplets are formed.

The separation of nucleation and growth ensures that a monodispersed droplet cloud is formed; that is, a collection of droplets which all have the same size. For such a droplet cloud, the number density n can be determined; the nucleation rate during the pulse is then found by

$$J = \frac{n}{\Delta t},$$
(4.1)

where Δt is the pulse duration.

4.1   Expansion wave tube

One of the ways to realize the nucleation pulse method experimentally is in a shock tube, that consists in its most basic form of a high-pressure section (HPS) and a low-pressure section (LPS), initially separated by a diaphragm; see Figure 4.1. The test gas mixture, which consists of one or more vapours in a carrier gas, is placed in the HPS; the LPS contains gas without any vapour. When the diaphragm is broken, an expansion wave (indicated by 1 in Fig. 4.1) travels into the HPS and a compression wave or shock wave (2) travels into the LPS. Our shock tube has a locally widened LPS; the interaction of the shock wave with this geometry results in a weak expansion wave (3) and an equally weak compression wave (4) which are sent in the direction of the HPS. When the shock wave reaches the end of the LPS, it reflects back (not shown).

Near the end wall of the HPS, a pressure history shown in the centre of Fig. 4.1 is realized. When the expansion wave arrives, the pressure decreases rapidly (a→b). A short time after the pressure drop ends, the weak expansion and compression wave cause a small dip in the pressure (c→d→e); this is the pulse. After that, the pressure remains approximately constant, until the reflection of the shock wave arrives.

Schematically, the temperature profile looks the same as the pressure profile. The changes in temperature cause the supersaturation to increase from its initial value to a larger value (shown at the left side of Fig. 4.1), which is however still too small to result in the formation a large amount of droplets. The small temperature dip during the pulse is enough to increase the supersaturation by a substantial factor; the nucleation rate then becomes several orders of magnitude higher. After the pulse, the nucleation process is quenched; the droplets that have been formed will be able to grow since the supersaturation remains larger than unity.
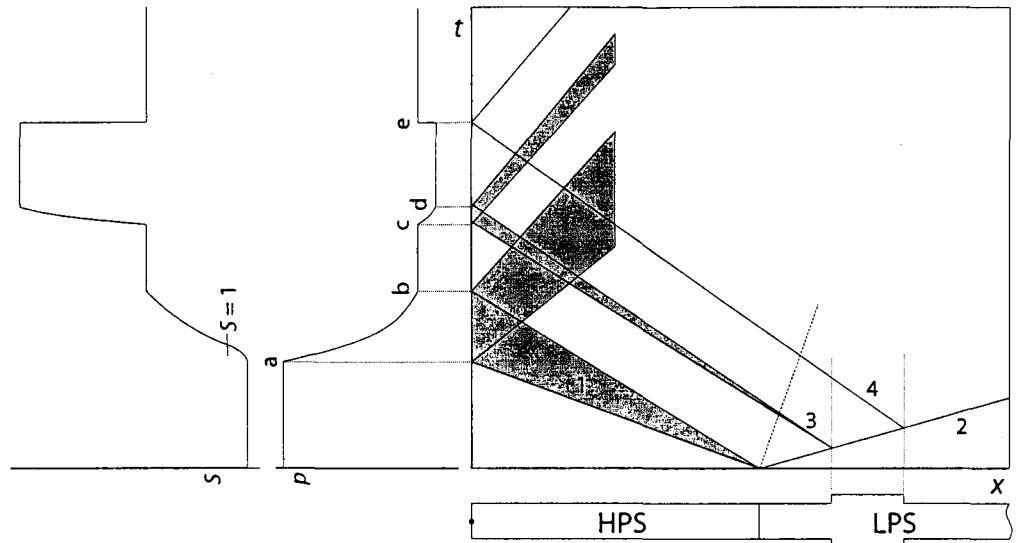
Figure 4.1: Right: schematic x-t plot of the waves in the expansion tube. Centre: pressure at the end wall of the HPS. Left: supersaturation at the end wall.

4.1.1   Setup

The HPS was made of stainless steel, had a length of 1.25 m and an inner diameter of 36 mm. The LPS, which was made of aluminium, was much longer; it had a length of 9.23 m. The pressure at the end wall of the HPS was recorded by a piezo-electric pressure transducer attached to a charge amplifier. The initial wall temperature of the HPS was measured with a thermocouple.

The test gas mixture consisted of the carrier gas helium, and a small but accurately known amount of water vapour (molar fraction 0.02%–0.5%). The helium gas had a purity of 99.999%.

Our aim was to obtain nucleation pulse pressures of about 1 bar (10^5 Pa), and pulse temperatures in the range 200–240 K. The initial temperature of the setup was laboratory temperature, ranging from 22.6 °C to 24.1 °C. For these conditions, the initial HPS pressure needed to be between 1.8 bar and 2.7 bar, while the initial LPS pressure was about 1.1 bar.

4.1.2   Thermodynamic state

It is impossible to measure the temperature directly because it changes too rapidly. Therefore, the temperature was calculated from the pressure, assuming an isentropic expansion:

$$\frac{T}{T_0} = \left(\frac{p}{p_0}\right)^\alpha . \tag{4.2}$$

The gas mixture is assumed to behave ideally. In that case the exponent α is given by $\alpha = (\gamma - 1)/\gamma$, with γ the ratio of the isobaric and isochoric heat capacities: $\gamma = c_p/c_v$. The γ of the gas mixture deviates somewhat from the γ of the carrier gas because of the vapour in the mixture.

To find the size of this deviation, we first consider the general case: a gas mixture with any number of components. We assume that one of the heat capacities of the mixture can be calculated by weighted averaging, where the weight factor is the molar fraction, if we use molar heat capacities:

$$c_{v,m} = \sum_i y_i c_{v,i} \quad \text{or} \quad c_{p,m} = \sum_i y_i c_{p,i}. \tag{4.3}$$

Here the subscripts m and i indicate properties of the mixture and of component i, respectively, and y_i is the molar fraction. When we further assume that the relation $c_p = c_v + R$ is valid, both for the mixture and for the individual components, it can be easily derived that

$$\gamma_m = 1 + \left[\sum_i \left(\frac{y_i}{\gamma_i - 1} \right) \right]^{-1}, \tag{4.4}$$

where γ_m is the γ of the mixture. In the case of a single vapour in a carrier gas, this relation simplifies to

$$\gamma_m = 1 + \left[\frac{y_v}{\gamma_v - 1} + \frac{1 - y_v}{\gamma_g - 1} \right]^{-1}, \tag{4.5}$$

where γ_v belongs to the vapour and γ_g belongs to the carrier gas. Similar formulas were used by several authors.[2,12,25,55] For helium, the ideal value $\gamma_{He} = 5/3$ was taken. The γ_{H_2O} value of water depends on the temperature and therefore changes during the expansion. However, the effect of the water vapour on the γ_m value of the mixture is quite small (in our experiment with the highest amount of water vapour, the γ changed only by 0.2%), so that an average value of $\gamma_{H_2O} = 1.33$ could be used. The final temperature correction due to the γ_m correction was only 0.15 K at most.

4.2 Mixture preparation

Because the nucleation rate strongly depends on the supersaturation, it is essential to know the vapour fraction of the test gas mixture with the highest accuracy. Therefore, a large part of the setup, called the mixture preparation device (MPD), was dedicated to producing the mixture.

The MPD consisted of three parts: a mass flow control part, a saturation part, and a heated part. We will first discuss the saturation section. Here, the carrier gas was saturated with water vapour by bubbling it through liquid water in a vessel at a constant temperature T_{sat} and pressure p_{sat}. The vessel, which we will call saturator, was fully filled with glass beads and partially with high-purity water. We used two of these saturators, connected in series. The vessels themselves were immersed in a water bath which was kept at a constant temperature (Fig. 4.4).

In the saturators, the saturated vapour fraction y_s is given by

$$y_s = \frac{p_s(T_{sat})}{p_{sat}} f_e(p_{sat}, T_{sat}), \tag{4.6}$$

Here the subscript 'sat' denotes a condition (pressure or temperature) inside the saturator, while subscript 's' indicates saturation: p_s is the saturated vapour pressure
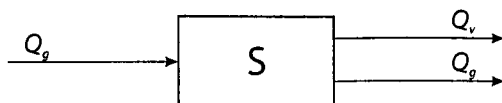
Figure 4.2: Gas flows (Q_g) and vapour flow (Q_v) entering and leaving a saturator.
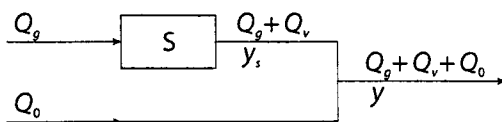
Figure 4.3: Mixing of the gas/vapour mixture and a dry gas stream.

of water without the presence of a carrier gas. The quantity f_e, called enhancement factor, is a factor that accounts for the influence of the carrier gas on the vapour-liquid equilibrium, and is usually slightly larger than unity. It is taken from Luijten[2]:

$$f_e(p, T) = \exp\left\{\frac{M[p - p_s(T)]}{\rho_\ell RT}\right\}.$$
(4.7)

Consider the saturator unit S which is shown schematically in Fig. 4.2. Carrier gas enters the saturator at a molar flow rate Q_g. If there is no accumulation, the carrier gas leaves the saturator at the same rate Q_g, together with the vapour at a rate of Q_v. Since the vapour fraction of the mixture y_s is by definition equal to $Q_v/(Q_g + Q_v)$, the flow rate of the vapour is

$$Q_v = \frac{y_s}{1 - y_s}Q_g = Y_sQ_g,$$
(4.8)

where $Y_s = y_s/(1 - y_s)$ is introduced to simplify the notation. To increase the range of achievable vapour fractions, the vapour/gas mixture can be diluted with a second pure carrier gas stream which has a flow rate Q_0 (see Fig. 4.3). After mixing, the final vapour fraction y is given by

$$y = \frac{y_s(Q_g + Q_v)}{Q_0 + Q_g + Q_v} = \frac{y_s(1 + Y_s)Q_g}{Q_0 + (1 + Y_s)Q_g},$$
(4.9)

where Eq. 4.8 was used in the second step. Using the definition of Y_s, the result can be simplified to:

$$y = \frac{y_s}{1 + (1 - y_s)Q_0/Q_g},$$
(4.10)

which shows that it is the ratio of the two carrier gas flow rates that determines the final vapour fraction. This ratio is determined before the start of the mixing process and it is kept constant during it. If y is the desired vapour fraction, Eq. 4.10 can be rewritten to find the flow rate ratio:

$$\frac{Q_g}{Q_0} = \frac{y(1 - y_s)}{y_s - y}.$$
(4.11)

Before the experiment, the saturated fraction y_s is known from the saturator pressure and temperature in combination with Eq. 4.6.

In the MPD, the mass flow controllers (MFCs, see Fig. 4.4) were used to control both the vapour fraction and the pressure. If, for example, the pressure p_{sat} decreased,
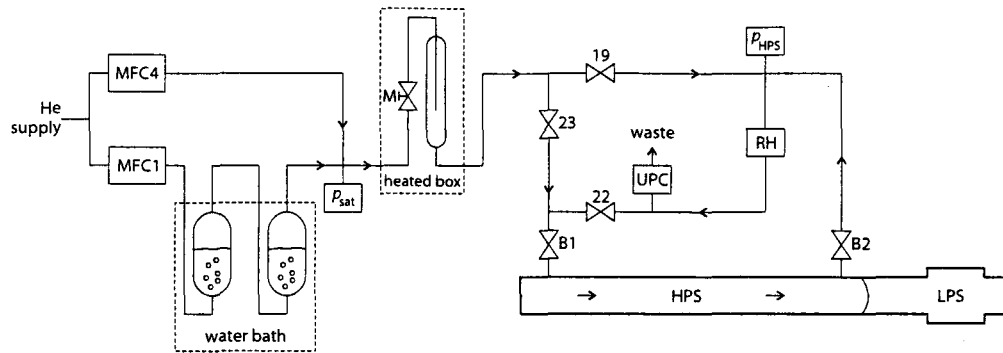
Figure 4.4: Schematic view of the mixture preparation device and the flushing section. MFC: mass flow controller; UPC: upstream pressure controller; RH: relative humidity sensor. The numbering of MFCs and valves follows Hrubý.[56]

the MFCs increased the gas flow rates slightly, while the ratio of the rates was kept constant.

In the heated part of the MPD ('heated box' in Fig. 4.4) the pressure was reduced from the saturator pressure to the desired HPS pressure. This was done by means of metering valve M, with which the flow rate could be accurately adjusted. The heated box also contained a static mixer, a cylindrical vessel in which fluctuations in the mixture composition were smoothed out. This vessel was heated to 80 °C to minimize wall adsorption.

4.3 Optical detection

To measure the droplet density at the end wall of the HPS, we used optical methods. If a light beam passes through a droplet cloud, part of the light is scattered, so that the main beam is attenuated. The amount of attenuation depends on the droplet density, so it might seem sufficient to measure the intensity change of the transmitted light to find the droplet density. However, the attenuation also depends on the size of the droplets, which is not known. The intensity of the scattered light does provide this information; if the wavelength of the light is of the same order as the droplet size, the scattered light intensity shows peaks and valleys as a function of the droplet size. For any droplet density, these extrema occur at the same droplet size.

Summarizing, the droplet density is found as follows: While the droplets grow, the scattered intensity shows extrema at certain times, which are used to determine the droplet size at those times. The size and the extinction together are sufficient to obtain the density.

Figure 4.5 shows how the extinction and scattering signals look during an experiment; the pressure at the end wall is also shown. We see that after the end of the pressure pulse ($t \approx 7$ ms) droplets are detected: the extinction I/I_0 curve decreases, while the scattered light shows peaks and valleys as the droplets grow.
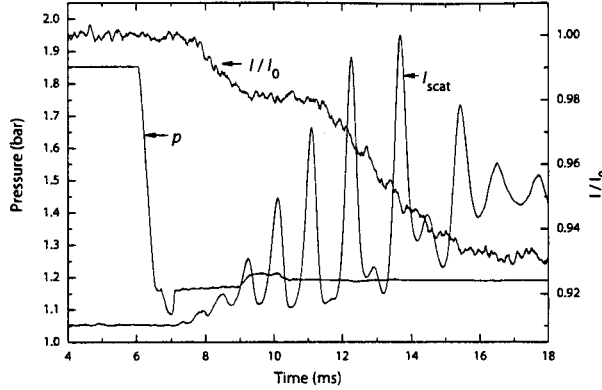
Figure 4.5: Example of pressure and optical signals during an experiment.

4.3.1 Mie theory

The theory that describes the scattering of light by small particles was first derived by G. Mie in 1908.[57] Here we will only show the basic part of the theory.[58]

We will first look at the scattering by a single particle illuminated by a light source. The intensity of the incident light is called I_0 (energy per unit time and area), the intensity of the scattered light at a distance r form the particle is called I. The incident light is a plane wave travelling in the positive z direction. Since I is proportional to I_0 and inversely proportional to r^2, it can be written as

$$I = \frac{F(\theta, \phi)}{k^2 r^2} I_0, \tag{4.12}$$

where k is the wave number $k = 2\pi/\lambda$ with λ the wavelength of the incident light, and $F(\theta, \phi)$ a dimensionless function that describes the dependence of the intensity on the angle.

Generally, the scattering by an object can be described by

$$\begin{pmatrix} E_l \\ E_r \end{pmatrix} = \begin{pmatrix} S_2 & S_3 \\ S_4 & S_1 \end{pmatrix} \frac{e^{-ikr+ikz}}{ikr} \begin{pmatrix} E_{l0} \\ E_{r0} \end{pmatrix}. \tag{4.13}$$

E_l is the amplitude parallel with the scattering plane and E_r is the amplitude perpendicular to it; see Fig. 4.6. The amplitude functions S_1 to S_4 generally depend on θ and ϕ. For a spherical particle, however, S_3 and S_4 are zero, so that

$$E_r = S_1(\theta) \frac{e^{-ikr+ikz}}{ikr} E_{r0} \quad \text{and} \quad E_l = S_1(\theta) \frac{e^{-ikr+ikz}}{ikr} E_{l0}. \tag{4.14}$$

S_1 and S_2 are independent of ϕ because the geometry is now axially symmetric around the z axis. The intensity of the scattered light is found by the square of the absolute value of the amplitude:

$$\begin{aligned} I &= |E_r|^2 + |E_l|^2 \\ &= \frac{|S_1(\theta)|^2}{k^2 r^2} |E_{r0}|^2 + \frac{|S_2(\theta)|^2}{k^2 r^2} |E_{l0}|^2. \end{aligned} \tag{4.15}$$

We now define the incident light to be linearly polarized in the x direction, so at an angle of ϕ with the plane of scattering. Then $E_{l0} = E_0 \cos \phi$ and $E_{r0} = E_0 \sin \phi$, so that

$$I = \frac{i_1(\theta) \sin^2 \phi + i_2(\theta) \cos^2 \phi}{k^2 r^2} I_0, \tag{4.16}$$
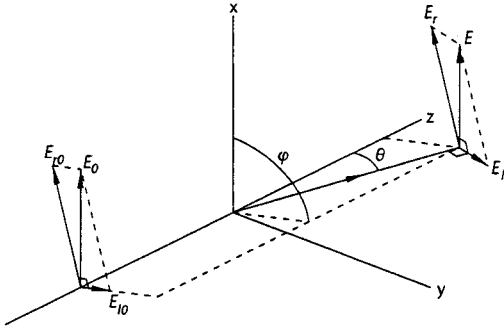
Figure 4.6: Scattering of light by a particle. Light travels in the positive z direction and is scattered by a particle in the origin. The angle of the scattering plane with the x-z plane is ϕ; the angle of the scattered light with the z-axis is θ.

where $i_1(\theta) = |S_1(\theta)|^2$ and $i_2(\theta) = |S_2(\theta)|^2$. By comparing this result with Eq. 4.12, we see that

$$F(\theta, \phi) = i_1(\theta) \sin^2 \phi + i_2(\theta) \cos^2 \phi. \tag{4.17}$$

The total energy flux in a solid angle given by $\theta_1 < \theta < \theta_2$ and $\phi_1 < \phi < \phi_2$ is found by integrating the intensity:

$$\begin{aligned} P &= \int_{\theta_1}^{\theta_2} \int_{\phi_1}^{\phi_2} I(\theta, \phi) \, r^2 \sin\theta \, d\theta \, d\phi \\ &= \frac{I_0}{k^2} \int_{\theta_1}^{\theta_2} \int_{\phi_1}^{\phi_2} F(\theta, \phi) \sin\theta \, d\theta \, d\phi \end{aligned} \tag{4.18}$$

In the last step, Eq. 4.12 was used. We see that P is independent of r, as it should be. For the spherical particle, the integration can be simplified using Eq. 4.16:

$$P = \frac{I_0}{k^2} \int_{\theta_1}^{\theta_2} [i_1(\theta) f_1 + i_2(\theta) f_2] \sin\theta \, d\theta, \tag{4.19}$$

with $f_1 = \int_{\phi_1}^{\phi_2} \sin^2 \phi \, d\phi$ and $f_2 = \int_{\phi_1}^{\phi_2} \cos^2 \phi \, d\phi$.

Extinction

If light travels through a cloud of identical particles, the attenuated light intensity is given by the law of Lambert-Beer:

$$I = I_0 \exp(-\beta d), \tag{4.20}$$

where d is the extinction length and β is the extinction coefficient, which is in the case of spherical particles equal to

$$\beta = n\pi r_d^2 Q_{\text{ext}}. \tag{4.21}$$

Here, r_d is the radius of a particle and n is the droplet density (number per unit of volume). The parameter Q_{ext}, called the extinction efficiency, is

$$Q_{\text{ext}} = \frac{4}{\alpha^2} \text{Re}\{S(0)\}. \tag{4.22}$$

where $S(0) = S_1(0) = S_2(0)$ and α is defined in the next section.
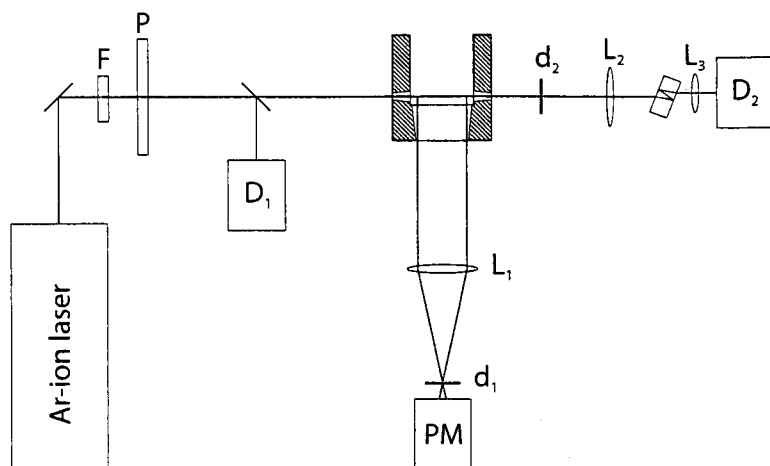
Figure 4.7: Schematic top view of the optical setup located at the end wall of the HPS.

Size parameter

The functions that depend on the size of the particle can be expressed as a function of the dimensionless quantity α, the so-called size parameter, defined as

$$\alpha = \frac{2\pi r_d}{\lambda} = k r_d. \tag{4.23}$$

In section 5.4, where we will show scattering graphs, the scattering intensity [or rather the function $F(\alpha)$] is shown as a function of the size parameter.

4.3.2   Setup

See Figure 4.7 for illustration. An Ar-ion laser produced a vertically polarized light beam with a total power of 200 mW at several wavelengths; the two lines with the highest amount of power were at 488.0 and 514.5 nm. The filter F was used to remove all wavelengths except the 514.5 nm line. To be certain of the polarization, the beam passed through a polarizer P with a vertical plane of polarization.

A small part of the light was deflected and recorded by photodiode D_1; this signal is called the reference signal, because it showed the intensity fluctuations of the beam, which were about 3.5%. The beam crossed the tube through windows in the side wall, which were slightly inclined to prevent internal reflections. The distance from the beam to the end wall of the HPS was 5 mm. The end wall contained a larger window, which allowed the scattered light to be measured by photomultiplier PM. The lens L_1 and the diaphragm d_1 ensured that only light scattered at 90° was recorded.

The main beam which left the tube passed through pinhole d_2 to remove the forward scattered light. Lenses L_2 and L_3 focused the beam on photodiode D_2. Before the light reached this photodiode, it was attenuated by recording only the second internal reflection of a glass plate, which was required because of the high intensity of the main beam.

4.4   Experimental procedure

All devices were switched on, including the laser and its cooling fan. The ventilation of the laser created an air circulation which had a considerable influence on the

temperature of the test section. Apart from that, it was found that the vibrations of the ventilation system could cause a 50 Hz fluctuation in the laser beam position; therefore, the ventilation tube was tightly fastened.

A new diaphragm was placed in the tube, and the tube was closed. Then both the LPS and HPS were evacuated; the HPS down to about 10 Pa. After the flow rate ratio of the mass flow controllers had been chosen, metering valve M was opened (Fig. 4.4). As the pressure in the MPD started decreasing, the MFCs slowly opened to supply gas. Valves 19 and 22 were initially closed; 23, B1 and B2 were open, so that the gas mixture flowed through the HPS, then trough the humidity sensor RH and finally reached the pressure controller (UPC). This device could control the gas flow to maintain a constant pressure in the HPS, and was initially closed.

While the pressure in the HPS increased, we slowly filled the LPS with helium to minimize the force on the diaphragm. In the HPS, when the pressure reached the preset value, the UPC opened to let gas out, which started the flushing process. Flushing means that the gas mixture flows through the HPS for some time at constant pressure, which was required to establish adsorption equilibrium with the tube walls and to remove foreign particles. As gas flowed through the RH sensor, the humidity could be monitored. Usually, its value was observed to strongly oscillate while the system of pressure and flow controllers equilibrated. We flushed the HPS at a rate of roughly 3.5 normal litre per minute, for about one hour, so that about 200 normal litre of gas was used.

After the entire system had stabilized, the gas flow was determined by the pressure difference over the metering valve ($p_{sat} - p_{HPS}$) and the amount this valve had been opened. Valve 19 was opened and 23 was closed, so that the gas flow bypassed the HPS and flowed directly to waste. Then the valves B1 and B2 were closed, isolating the HPS. The laser was set to a power of 200 mW and the amplifier of the dynamic pressure transducer was set in the 'operate' mode. Finally, the trigger was armed and the diaphragm was broken.

The data acquisition system that we used (LeCroy, type 6810) recorded the signals from the pressure transducer, the photomultiplier and the two photodiodes. All signals were sampled at a frequency of 100 kHz. The data acquisition system was used with a so-called pre-trigger operation of 5 ms, which means that after the experiment, the initial values of the signals (as they were during the 5 ms before the trigger occurred) were available. This was required to obtain the initial output voltages of the pressure transducer and photodiodes.

After the experiment, the offsets of the photodiodes were recorded by measuring their output voltage in the dark.

4.5 Accuracy

In this section, we will calculate the accuracy of the measurements, and the accuracy of quantities that are based on the measurements, such as temperature and vapour fraction. First, we introduce some notation, which is taken from Hrubý.[56]

$E(y)$ means the uncertainty in the quantity y. Hereafter, we will frequently use the word error for the uncertainty, although these terms are not exactly the same. The

notation $E(y|x)$ means the error in y caused by the error in x, and can be found by:

$$E(y|x) = |\partial y/\partial x| E(x).$$ (4.24)

We will also use the relative error, defined by $\varepsilon(y) = E(y)/|y|$. A relative error caused by the (relative) error in another quantity can be found by

$$\varepsilon(y|x) = \left| \frac{x}{y} \frac{\partial y}{\partial x} \right| \varepsilon(x) = \left| \frac{\partial \ln y}{\partial \ln x} \right| \varepsilon(x).$$ (4.25)

4.5.1 Thermodynamic state

Accuracy of temperature and pressure measurements

The initial pressure of the HPS, p_0, was measured by the Druck PMP4070, range 0–10 bar. This pressure transducer was compared with a more accurate one of the same type (range 0–3.5 bar); it was found that the maximum error was 0.3%.

The initial temperature of the HPS, T_0, was determined by a thermocouple (NiCr-NiAl) in good thermal contact with the wall, connected to a Keithley 871A digital thermometer. We assume that the maximum error is 0.1 K.

The pressure changes in the HPS, $\Delta p(t)$, were recorded by a Kistler 603B piezo-electric pressure transducer, connected to a Kistler 5001 charge amplifier. The accuracy is $0.5\%^2$.

Accuracy of the pulse temperature

To find the error in the temperature, we rewrite Eq. 4.2 as a function of the three measured quantities specified above:

$$T = T_0 \left(\frac{p_0 - \Delta p}{p_0} \right)^\alpha,$$ (4.26)

where Δp is defined such that $p = p_0 - \Delta p$. Applying the formula for relative error propagation, Eq. 4.25, we find:

$$\varepsilon(T|T_0) = \varepsilon(T_0);$$ (4.27)

$$\varepsilon(T|p_0) = \alpha \frac{\Delta p}{p} \varepsilon(p_0);$$ (4.28)

$$\varepsilon(T|\Delta p) = \alpha \frac{\Delta p}{p} \varepsilon(\Delta p).$$ (4.29)

The initial temperature T_0 was approximately the same for all experiments, so the error in T caused by T_0 is always the same. The last two equations show that the errors in p_0 and Δp propagate by the same factor $\alpha \Delta p/p$. Both α and p had nearly the same values in all experiments; in contrast, Δp differed much. The experiments in which Δp was large, so the ones with a low nucleation temperature, will have the largest error in the temperature. The total relative error in the temperature is

$$\varepsilon(T) = \left[\varepsilon^2(T|T_0) + \varepsilon^2(T|p_0) + \varepsilon^2(T|\Delta p) \right]^{1/2}.$$ (4.30)

Accuracy of the pulse pressure

Because $p = p_0 - \Delta p$, the error in the pressure can be written immediately as:

$$E(p) = \left[E^2(p_0) + E^2(\Delta p) \right]^{1/2}. \tag{4.31}$$

For low temperatures, p_0, Δp and their errors are all higher, and so is therefore the error in p.

4.5.2 Vapour fraction

For error analysis, we can use the approximation $y \ll 1$, so that Eq. 4.10 simplifies to:

$$y \approx y_s(p_{\text{sat}}, T_{\text{sat}}) \frac{Q_g}{Q_g + Q_0}, \tag{4.32}$$

which shows that a relative error in y_s causes the same relative error in y, that is, $\varepsilon(y|y_s) = \varepsilon(y_s)$.

Saturator pressure

We measured the pressure after the saturators p_{sat} with a Druck PMP1400, range 0–100 bar. After calibration, the accuracy is assumed to be equal to a difference of ± 1 in the last digit of the display, which corresponds to 0.02 bar. Using Eq. 4.6, we find:

$$\varepsilon(y|p_{\text{sat}}) = \varepsilon(y_s|p_{\text{sat}}) = \left| -1 + p_{\text{sat}} \frac{\partial \ln f_e(p, T_{\text{sat}})}{\partial p} \right|_{p_{\text{sat}}} \left| \varepsilon(p_{\text{sat}}). \right. \tag{4.33}$$

Using Eq. 4.7, it was found that $\partial f_e / \partial p \approx 10^{-8}$ Pa^{-1}, so that we can safely make the approximation

$$\varepsilon(y|p_{\text{sat}}) \approx \varepsilon(p_{\text{sat}}). \tag{4.34}$$

Saturator temperature

The temperature inside the saturators T_{sat} was measured by a platina resistor thermometer with an accuracy of 0.02 K. Eq. 4.6 gives

$$\varepsilon(y|T_{\text{sat}}) = \varepsilon(y_s|T_{\text{sat}}) = \left| \frac{1}{p_s(T_{\text{sat}})} \frac{\mathrm{d}p_s(T)}{\mathrm{d}T} \right|_{T_{\text{sat}}} + \frac{\partial \ln f_e(p_{\text{sat}}, T)}{\partial T} \right|_{T_{\text{sat}}} \left| E(T_{\text{sat}}). \right. \tag{4.35}$$

The derivative of $\ln f_e$ with respect to temperature was found to be much smaller than the other term between the modulus lines, so that

$$\varepsilon(y|T_{\text{sat}}) \approx \frac{p_s'(T_{\text{sat}})}{p_s(T_{\text{sat}})} E(T_{\text{sat}}). \tag{4.36}$$

In the range of saturator temperatures that we used, we could make the approximation $p_s'(T_{\text{sat}})/p_s(T_{\text{sat}}) \approx 0.06$ K^{-1}.

Mass flow controllers

After calibration of an MFC, the accuracy is given by[56]

$$\varepsilon(Q) = 0.002 Q_{\text{full}}/Q + 0.007, \tag{4.37}$$

where Q_{full} is the flow rate of the MFC at full scale (the flow rate at the maximum output voltage). Applying Eq. 4.25 to Eq. 4.32, the error in the fraction due to the error in the flow rates is eventually found to be

$$\varepsilon(y|Q_g) = \frac{Q_0}{Q_g + Q_0} \varepsilon(Q_g); \tag{4.38}$$

$$\varepsilon(y|Q_0) = \frac{Q_0}{Q_g + Q_0} \varepsilon(Q_0). \tag{4.39}$$

The error propagation is determined by the fraction $Q_0/(Q_g + Q_0)$, which is a measure of the amount of dilution. It appears that a large amount of dilution will increase the error in the vapour fraction.

Total error

The total error in the vapour fraction is

$$\varepsilon(y) = \left[\varepsilon^2(y|p_{\text{sat}}) + \varepsilon^2(y|T_{\text{sat}}) + \varepsilon^2(y|Q_g) + \varepsilon^2(y|Q_0) \right]^{1/2}. \tag{4.40}$$

A complete numerical evaluation of the error in the vapour fraction of all experiments is shown in appendix B.1.

4.5.3 Nucleation rate

Theoretical nucleation rate

We already know the uncertainties of p, T and y, and since the theoretical nucleation rate J can be written as a function of those quantities, we could use the error propagation formulas to calculate the error in J. However, it is not correct to do so, because the errors in p and T are not independent; both p and T depend on p_0 and Δp.

The correct way to proceed is to write J as a function of the independent, measured quantities p_0, Δp, T_0 and y. We could then use the error propagation formulas, but this resulted in complicated expressions which did not give new insights. Instead, we used a simpler way to find the error:

$$E(\ln J|X) = \left| \ln\{J[x]\} - \ln\{J[x + E(x)]\} \right|. \tag{4.41}$$

The error in $\ln J$ caused by a quantity X was calculated by substituting the expected value of X and the value of X with the maximum error, and then subtracting the two results. We chose to express the error as an error in $\ln J$, not in J, because J and its error were quite large numerically. As a result, the error in J could be described by an error factor f_{err}, in the following way:

$$\ln J - E(\ln J) < \ln \hat{J} < \ln J + E(\ln J), \tag{4.42}$$

where $\hat{J}$ is the real nucleation rate and J is the measured value. Exponentiating yields

$$J\, f_{\mathrm{err}}^{-1} < \hat{J} \quad < J\, f_{\mathrm{err}}, \tag{4.43}$$

with $f_{\mathrm{err}} = \exp\left[E(\ln J)\right]$. A complete numerical evaluation of the error in the theoretical nucleation rate J^{stan} of all experiments is shown in appendix B.2.

Experimental nucleation rate

Because $J = n/\Delta t$, the error in the experimental nucleation rate is caused by the errors in the density n and pulse duration Δt. In the next chapter we will see that n can be determined quite accurately, but Δt cannot. The error in J is therefore completely determined by the error in Δt, which is about 30%.

5. Data analysis

5.1 General

First the voltage recorded by the charge amplifier $V(t)$ is converted to a pressure $p(t)$:

$$p(t) = \kappa[V(t) - V_0] + p_0, \tag{5.1}$$

where p_0 is the known pressure in the HPS before the start of the experiment, and V_0 is the voltage at that time. The constant κ, with units of pressure per voltage, is determined by the settings of the charge amplifier; its value must be found by calibration.

The offsets of the extinction and reference signals are taken into account, and the extinction signal $I(t)$ is normalized with respect to the reference signal $R(t)$.

$$I_{\text{corr}}(t) = [I(t) - I_{\text{off}}]\frac{R(0) - R_{\text{off}}}{R(t) - R_{\text{off}}}. \tag{5.2}$$

Note that the time-independent value in the numerator $R(0) - R_{\text{off}}$ is not important since only the relative changes from the initial value are important. To obtain this initial value, the signal that has been recorded right before the start of the experiment (about 5 ms) is averaged. Next, the extinction and scattering signals are filtered, by means of a running average over 11 points.

To assign a single thermodynamic state to the nucleation pulse, the pressure signal during the pulse must be averaged. The beginning and ending time of the pulse are determined by the experimenter. There is some ambiguity in the choice of these times, especially the beginning time. Luijten[2] has shown that the final results are 'quite insensitive' to this choice. Still, the uncertainty in the total pulse duration can be as much as 30%.

In the next step, the temperature is calculated using the isentropic expansion relations as described in section 4.1.2.

Finally, the positions of the extrema in the scattering signal must be identified. This procedure is currently not automated; the experimenter can best distinguish the peaks from the noise. To obtain the droplet density, two methods are available. The one that has been used in the past[2,25,28] will be called the 'old method'.

5.2 Old method

Denoting the scattering extremum number with i, the time at which it is observed with t_i, and the corresponding size with α_i, we derive from the extinction formulas Eqs. 4.20 and 4.21 that

$$n_i = \frac{4\pi \ln[I_0/I(t_i)]}{\alpha_i^2 Q_{\text{ext}}(\alpha_i)\lambda^2 d}. \tag{5.3}$$
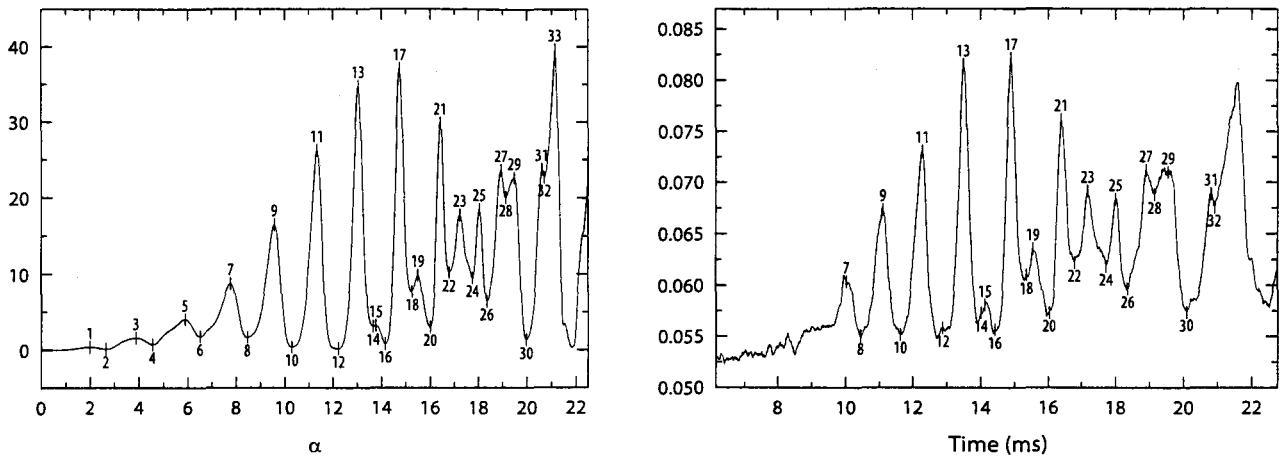
Figure 5.1: Scattered light intensity of experiment 35. Left: theoretical, right: experimental.

The extinction length d is approximated by the internal diameter of the high pressure section, which is 36 mm.

The measured droplet densities during the droplet growth period differ from the density at the end of the nucleation pulse, because the gas mixture is compressed after the end of the pulse, and so is the droplet cloud. Assuming isentropic behaviour, we can relate a density change of a gas to a pressure change:

$$\frac{\rho}{\rho_0} = \left(\frac{p}{p_0}\right)^{1/\gamma}. \tag{5.4}$$

We assume that the droplet density changes in the same way as the gas density, so that the droplet density at the end of the pulse can be found by

$$n_{\text{pulse},i} = \frac{n_i}{C_i} \quad \text{with} \quad C_i = \left[\frac{p(t_i)}{p_{\text{pulse}}}\right]^{1/\gamma} > 1. \tag{5.5}$$

The nucleation rate is then $J_i = n_{\text{pulse},i}/\Delta t$, where Δt is the pulse duration. Concluding: with this method we obtain a value for the nucleation rate for every Mie extremum that we can identify.

5.3 New method

Although the method described above looks perfect theoretically – and provides excellent results in some cases – it has a practical drawback. Generally, because of the very small amount of light extinction, there is much noise on the intensity signal. Since the old method only takes one sample of the extinction signal per Mie extremum, the resulting droplet density might be far from the real value. The present author looked for a way in which the entire extinction signal could be used, instead of selecting just several data points. Specifically, applying Eq. 5.3 on the whole signal would be an improvement. This is impossible in principle because the size parameter α is only known at times when scattering extrema are observed, not in between. However, if we assume the droplet growth to be well-behaved – which is the case in all
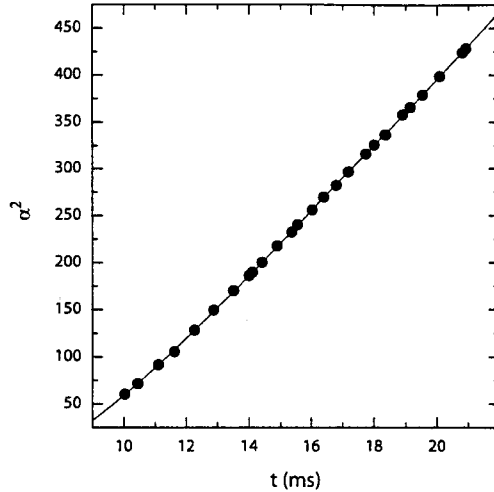
Figure 5.2: Droplet growth of experiment 35: square of the size parameter α versus time. Circles: values obtained from the extrema in the scattered light; line: fourth-order polynomial fit.

experiments – we can interpolate the droplet size between the known values. Even better, we can fit the points in the α-t diagram with some appropriate curve.

Fitting the data points requires knowledge of the underlying physical relations. We know from droplet growth theory that in the diffusion-controlled regime, the square of the droplet radius grows proportional to time, so that α^2 is also proportional to the time. It seems therefore appropriate to fit the points in an α^2-t diagram with a line, as a first approximation. For most experiments the points were observed to deviate somewhat from this ideal behaviour and finally it was found that a fourth-order polynomial was necessary to reproduce the α^2-t curve accurately. As an example, Fig. 5.1 shows the theoretical scattered intensity as a function of α, and the experimental intensity as a function of time. By matching the extrema, the α^2-t plot of Fig. 5.2 is obtained (circles). The polynomial fit is shown as a line.

Now that the droplet size can be approximated at any instant of time by means of the $\alpha^2(t)$ fit, it is in principle possible to apply Eq. 5.3 at every data point and get a value for n at all those points. The final value of n could then be obtained by simply taking the average. There is, however, a better way to find n. We first rewrite Eq. 5.3, including the density correction:

$$n = \frac{4\pi \ln[I_0/I(t)]}{\alpha(t)^2 Q_{\text{ext}}[\alpha(t)]C(t)\lambda^2 d}. \tag{5.6}$$

We make a graph, in which we plot a point for each time t, with the vertical coordinate equal to the numerator in Eq. 5.6, and the horizontal coordinate equal to the denominator. We then obtain n as the slope of the best fitting line, going through the origin.* In practice, the time-independent quantities can be left out, and what is plotted is

on the vertical axis: $Y(t) = \ln[I_0/I(t)]$,   (5.7)

on the horizontal axis: $X(t) = \alpha^2(t) Q_{\text{ext}}[\alpha(t)]C(t)$;   (5.8)

---

*The result obtained by fitting a line is different from taking the average. If a quantity a is found by $a = y/x$, the simple average is $\bar{a} = \sum y_n/x_n$. The slope of the line of best fit is $a_{\text{fit}} = \sum x_n y_n / \sum x_n^2$. If this is written as $a_{\text{fit}} = \left[\sum x_n^2(y_n/x_n) \right]/ \sum x_n^2$, we see that the slope is a weighted average with weight factor x_n^2.
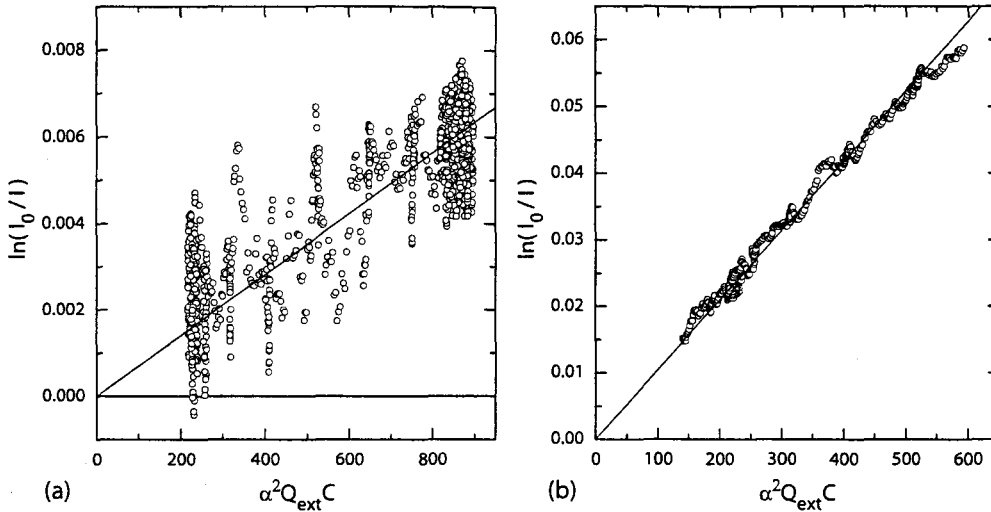
Figure 5.3: Plot of the quantities of Eqs. 5.7 and 5.8. Circles: experimental values; line: best fitting line through the origin. a: experiment 35; b: experiment 25.
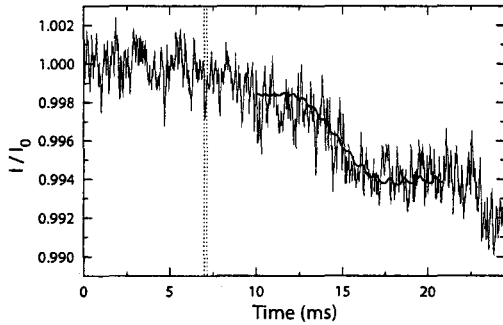
Figure 5.4: Light extinction of experiment 35. Thin line: experimental light intensity, scaled with the initial intensity. Thick line: expected intensity from Eq. 5.10. Dotted vertical lines: begin and end time of the nucleation pulse.

see Fig. 5.3a. To illustrate the advantages of the new method, an experiment with a particularly noisy extinction signal was selected. In other cases the deviations from the line are much smaller (Fig. 5.3b).

If the slope of the best fitting line is called s, the droplet density n_{fit} is found by

$$n_{\text{fit}} = \frac{4\pi}{\lambda^2 d} s. \tag{5.9}$$

Based on the value of n that has been obtained and the droplet growth $\alpha(t)$ fit that was found earlier, it is possible to calculate the intensity signal from Eq. 5.6 that we would expect when n is assumed to be constant:

$$I_{\text{expected}}(t) = I_0 \exp\left(-\frac{\lambda^2 d}{4\pi} n_{\text{fit}} \alpha^2 Q_{\text{ext}} C\right) = I_0 \exp[-s\, X(t)]. \tag{5.10}$$

This expected signal can be visually compared with the observed one; for the example this is shown in Fig. 5.4. We will see that this feature can be an aid to the identification of extrema in the scattering signal, which we will illustrate in the next section.

5.3.1   Example of the new method

In experiment 25 the scattering signal shown in Fig. 5.5 was observed; for comparison the theoretical scattering versus size diagram is shown next to it. In Fig. 5.5 we can
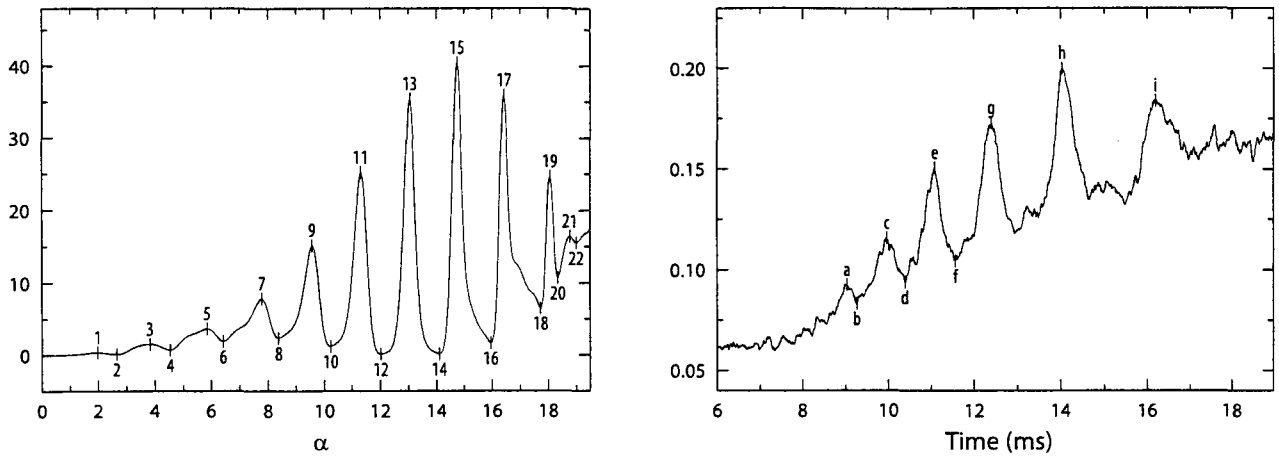
Figure 5.5: Scattered light intensity of experiment 25. Left: theoretical, right: experimental.

clearly see several Mie extrema, which have been marked by letters. A problem of this experiment was that it was unclear to which theoretical extrema – and to which droplet sizes – they corresponded. Three identifications that were considered are shown in Table 5.1.

Table 5.1: Identification of extrema in the scattered light of Fig. 5.5.

	a	b	c	d	e	f	g	h	i
I	3	4	5	6	7	8	9	11	13
II	5	6	7	8	9	10	11	13	15
III	7	8	9	10	11	12	13	15	17

Using the old data analysis method, it was not easy to choose an identification. In this case, III was chosen, based on the shapes of the observed peaks.

When this experiment was later reanalyzed with the new data analysis method, it was clear which identification was the correct one. Figure 5.6 shows the expected intensity superimposed on the experimental signal, for the three options. It is clear that option II gives the best match, and is very likely the correct one.

In some cases the fit was not that good, and the amount of light extinction gradually decreased below the expected value. One way to explain this is that the droplet density decreases during the measurement period. A second explanation is that the extinction length (d in Eq. 5.10) decreases, which would occur if the cloud of droplets shrunk. A decrease like this is possible if the thermal boundary layers at both windows grow during the experiment and cause droplets at the boundaries of the cloud to evaporate.

5.4 Scattering

In this section we will investigate the influence of several parameters on the scattered intensity as a function of the droplet size. We will use the formulas from section 4.3.1 to calculate the theoretical scattering, and we will try to match the experimental scat-
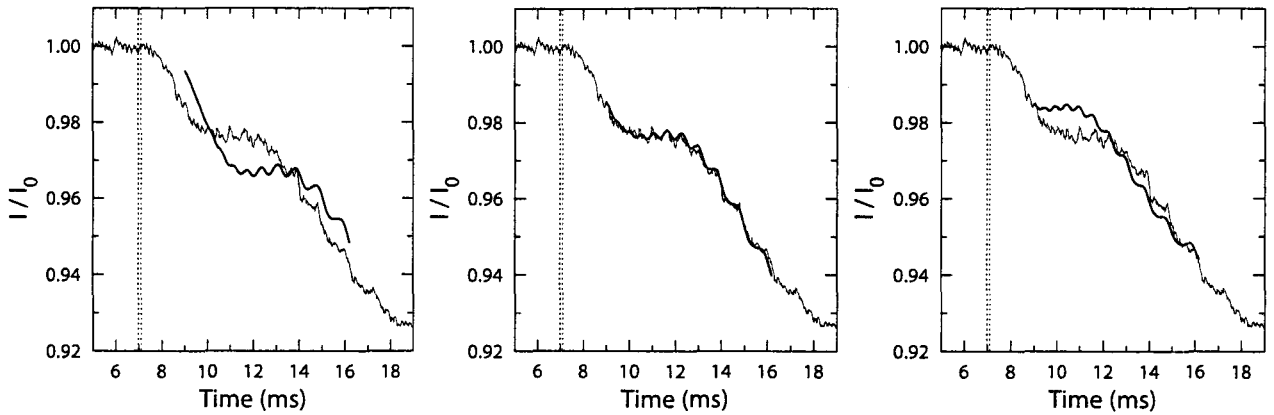
Figure 5.6: Extinction of experiment 25. Thin line: experimental scaled intensity I/I_0; thick line: expected intensity from Eq. 5.10. The three figures show the expected intensity for identifications I, II and III of Table 5.1. Dotted vertical lines: begin and end time of the nucleation pulse.

tering signals as well as possible. Obtaining the correct theoretical scattering diagram is important for the data analysis, since it is the only way to identify the experimental extrema and to obtain the right droplet size, corresponding to an extremum. Figure 5.7 shows two experimental scattering signals in which many extrema were observed, and which are therefore suitable for comparison with the theory.

5.4.1 Angle

The setup has been designed such that the light that is scattered at an angle of 90° is recorded. In practice, the optical alignment is never perfect, and the horizontal scattering angle will always deviate slightly from 90°. It was found that differences as small as 0.5° will make a difference in the observed pattern of peaks, so that knowledge of the exact angle is required for an accurate analysis.

A convenient way to determine the scattering angle is to adjust the angle that is used to make a theoretical plot, until it matches the result obtained experimentally.
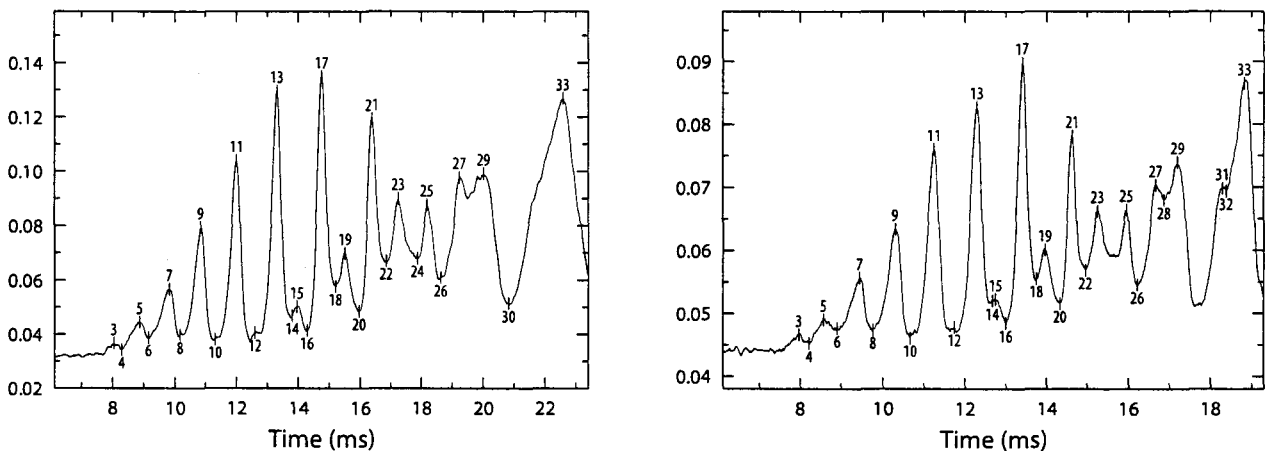
Figure 5.7: Experimental scattered intensity signal of experiments 29 (left) and 39 (right). The extrema have been numbered.
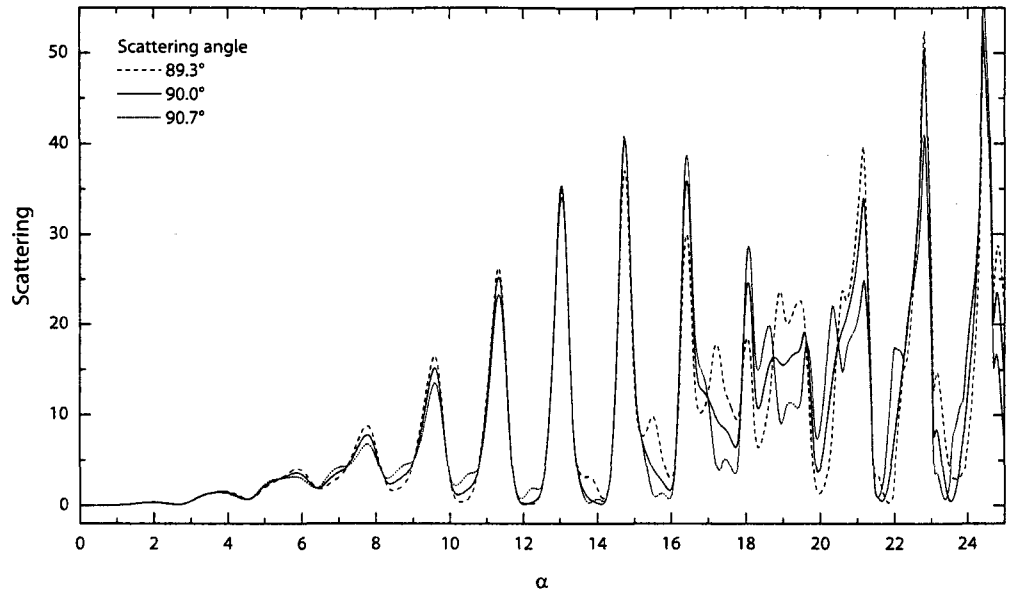
Figure 5.8: Scattering as a function of the size parameter for three scattering angles: 89.3°, 90.0° and 90.7°. Width of size distribution: 0.25; refractive index: 1.33.

Figure 5.8 shows the scattering intensity for three angles: 89.3°, 90.0° and 90.7°. We see that the change of angle modifies the valleys, notably near $\alpha = 14$ and $\alpha = 15$. The region between $\alpha = 17$ and $\alpha = 21$ is most sensitive to changes in the angle, and it is this region which was compared with the experimental signal to find the angle.

Based on a comparison with the experimental scattering (Fig. 5.7) an angle of 89.3° was chosen, except for experiment 25, which was analyzed using the 90.0° scattering. (After experiment 25, changes were made to the optical setup, resulting in a different angle.) The advantage of a slight deviation from 90° is that smaller peaks appear in some valleys (e.g., those indicated by numbers 15 and 19 in Fig. 5.7), which makes it easier to identify the extrema in the experimental signals.

The influence of the other scattering angle, the angle of the scattering plane with the horizontal plane, is much smaller. In fact, even for a deviation of 10° from the horizontal plane, there is almost no difference with the case of horizontal scattering. Eq. 4.17 shows why the effects are so small: for ϕ close to 90°, the factor $\cos^2 \phi$ is very small (e.g., $\cos^2 80° \approx 0.03$), so that $F(\theta, \phi)$ is very insensitive to ϕ in this region.

5.4.2   Refractive index

The analysis in section 3.4 showed that we can safely assume that the refractive index is always between 1.32 and 1.34. Figure 5.9 shows the theoretical scattering patterns for refractive indices of 1.32, 1.33 and 1.34. The differences between them are most apparent at high α values; above $\alpha = 17$, the shapes of the peaks and valleys clearly change. At lower α values the heights of the peaks change; the α positions of the peaks are also slightly different.

The only significant changes are at high α values. But at low temperatures, where we expect the refractive index to be lower, this region of the scattering curve is never
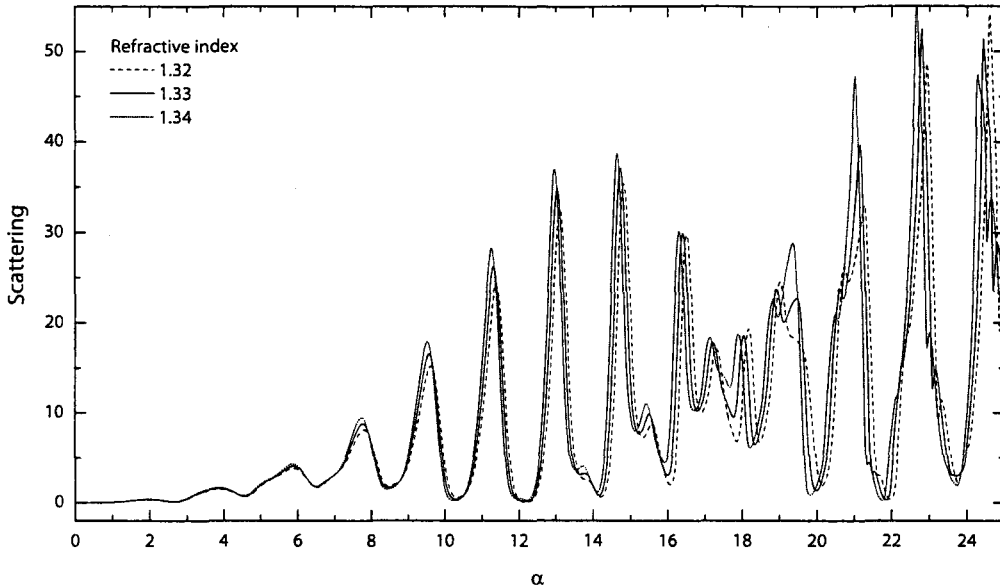
Figure 5.9: Scattering as a function of the size parameter for three values of the refractive index: 1.32, 1.33 and 1.34. Scattering angle: 89.3°; width of size distribution: 0.25.

observed – below 220 K, the highest α value seen was only $\alpha \approx 7$. Therefore, a refractive index of 1.33 was used for all experiments.

5.4.3 Size distribution

We generally assume that the droplet cloud is monodispersed, that is, that all droplets have the same size. In reality, there is at any time in the experiment a distribution of droplet sizes, because of the finite duration of the nucleation pulse. The result of this is that the diagram of scattering versus time looks smoother, due to the contribution of the different droplet sizes at each time. The size distribution can be described by a function $n(r)$, which has a unit of m^{-1} and is normalized such that $\int_0^\infty n(r)\, dr = 1$. The observed scattered light intensity is then

$$F = \int_0^\infty n(r) F_0(r)\, dr. \tag{5.11}$$

Here $F_0(r)$ is the F of a particle with a certain radius r. Looijmans[25] already investigated the effect of a size distribution on F; he used a so-called lognormal distribution. We will take a much simpler distribution

$$n(r, r_0) = \begin{cases} \frac{1}{2\Delta r} & \text{if } r_0 - \Delta r < r < r_0 + \Delta r, \\ 0 & \text{otherwise}, \end{cases} \tag{5.12}$$

which is a constant distribution centred about r_0 and with a width of $2\Delta r$. The scattered intensity is then

$$F(r_0) = \frac{1}{2\Delta r} \int_{r_0-\Delta r}^{r_0+\Delta r} F_0(r)\, dr, \tag{5.13}$$

which is simply a moving average over a width of $2\Delta r$.
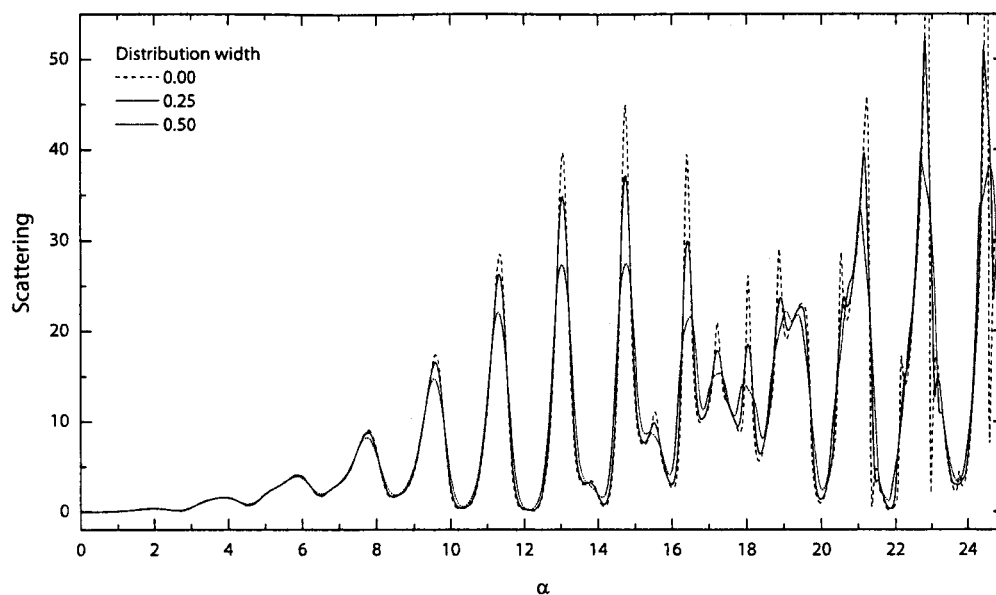
Figure 5.10: Scattering as a function of the size parameter for three values of the size distribution: 0, 0.25 and 0.50. Scattering angle: 89.3°; refractive index: 1.33.

Figure 5.10 shows the smoothed scattered intensity $F(r_0)$ for size distributions with widths of 0, 0.25 and 0.50, in α units. For the analysis of all experiments, a width of 0.25 was chosen since it matches the experimental signal best, although the the monodispersity varies slightly from one experiment to another, and generally decreases during the droplet growth.

6. Results

In this chapter we present the results of our nucleation experiments, and we compare them to measurements by Peeters and by Wölk et al. Peeters's data was obtained in 2001 using the same setup as we used. This data was corrected by the current author, see appendix A.1. Wölk et al. measured nucleation rates of water in argon between 10^{11} and 10^{15} m^{-3}s^{-1} in a nucleation pulse chamber, in which the nucleation pulse method was realized by means of valves which connected pressure-controlled volumes to the main chamber volume.[12] With this method well-reproducible pressure pulses could be obtained. For more information about the data by Wölk et al., see appendix A.2.

Figure 6.1 shows the experimental conditions as a function of the temperature. Note that to obtain a constant nucleation rate at low temperature, the vapour pressure must be decreased, while the supersaturation must be increased. The new experiments are at somewhat higher supersaturations than those of Peeters, and are also higher than Wölk's. Each of the three measurement sets has a temperature range of 40 K, but the temperature interval of Wölk's data is located 20 K higher. A feature of Wölk's data is that it consists of five isothermal sets; a deliberate division, which was made possible by the reproducibility of the experimental nucleation temperatures.

In Figure 6.2, the experimental nucleation rates are shown as a function of temperature, scaled with the theoretical predictions of the standard theory. The lower the temperature, the higher the deviation from the theoretical predictions. At 200 K, the experimental nucleation rate is about six orders of magnitude higher than predicted. Although all three data sets show this trend, there are some differences between them. The new data is about one to two orders below Peeters's results, while the data of Wölk lie exactly in between them. The scatter in the new data and those of Peeters is
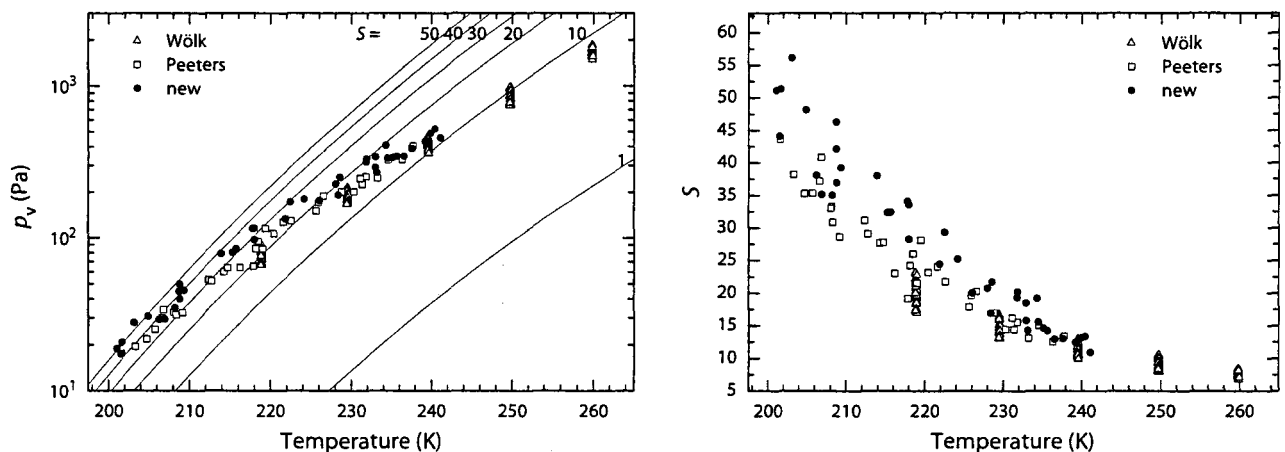
Figure 6.1: Vapour pressure (left) and supersaturation (right) of the nucleation pulse in the experiments, as a function of the temperature. In the vapour pressure graph, the lines are lines of constant supersaturation.
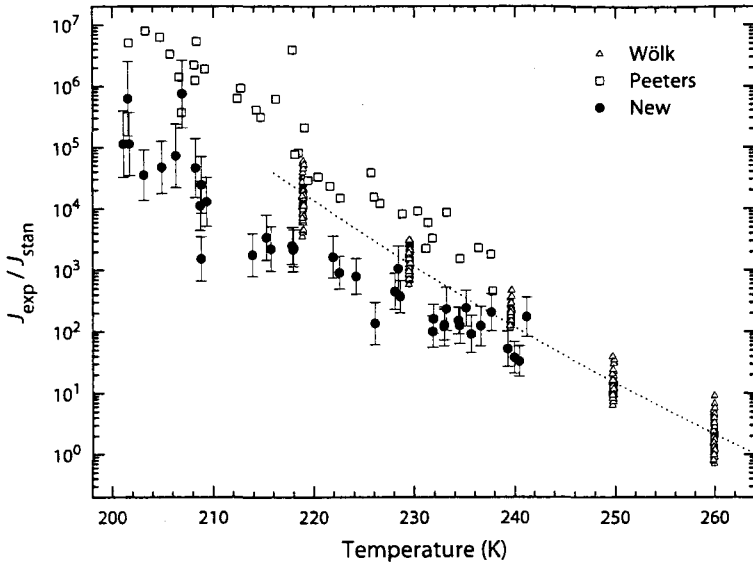
Figure 6.2: Ratio of experimental and theoretical nucleation rates. The error bars give the uncertainty due to the theoretical nucleation rate only. The dotted line is a fit through the data of Wölk *et al.* of the form $\exp(A_1 + B_1/T)$; see Eq. 6.5.

about the same and seems to increase at low temperatures.

6.1   Empirical correction

At this time, there is no theory which correctly predicts nucleation rates for an extended range of conditions. An equation capable of doing so would be valuable for the analysis of all kinds of industrial and natural processes, and – until better theories are found – such expressions can be obtained by modification of the theoretical expressions we do have. Commonly, the nucleation rate prediction is corrected by an additional factor:

$$J_{\text{corr}}(T, S) = f(T, S)\, J_{\text{theo}}(T, S). \tag{6.1}$$

Here and everywhere else we express J as a function of T and S (another option is to write it as a function of T and p_v). We will assume that the correction can always be written as a product:

$$J_{\text{corr}}(T, S) = f_T(T) f_S(S)\, J_{\text{theo}}(T, S). \tag{6.2}$$

6.1.1   Temperature correction

The most obvious problem of all nucleation theories is their failure to predict the temperature dependence of the rates: they may be correct at some temperature, but several orders off at another. Wölk *et al.*[59] suggested, on the basis of theoretical and experimental grounds, that the discrepancy could be described by

$$\ln\left(\frac{J_{\text{exp}}}{J_{\text{class}}}\right) = A + \frac{B}{T}, \tag{6.3}$$

where J_{class} is the classical nucleation theory, without the $1/S$ correction; it is $J_{\text{class}} = S \times J_{\text{stan}}$, where J_{stan} is given by Eq. 2.41. An appropriate correction is then

$$J_{\text{corr}}^T(T, S) = \exp(A + B/T) J_{\text{class}}(T, S). \tag{6.4}$$

Wölk *et al.* determined the constants A and B based on their experimental data of the nucleation of water. By comparing the corrected predictions with a large amount of measurements by others, they found that their new expression worked well in a large temperature range.

We chose to use J_{stan} instead of J_{class}, so that our corrected nucleation rate is

$$J_{corr,1}^{T}(T, S) = \exp(A_1 + B_1/T) J_{stan}(T, S).\tag{6.5}$$

We used different expressions for the properties of water, which is another reason that we found different values for the constants A_1 and B_1. To obtain them, we fitted the data by Wölk with a line $A_1 + B_1/T$ in a diagram of $\ln(J_{exp}/J_{stan})$ versus T. The resulting values are given in Table 6.2, and Fig. 6.2 shows the fit graphically. The fitted function appears to represent the temperature dependence of Wölk's data well. There is still some scatter in the vertical direction; one of its causes will be explained in the next section.

6.1.2 Supersaturation correction

In the diagrams by Wölk *et al.* that are similar to Fig. 6.2, the deviation of the data from the fit is shown as an error bar, leading to the assumption that the deviation is caused by random experimental scatter. This is, however, not the case. At each nucleation temperature, experiments were performed in a range of supersaturations. We found that data points which were higher than the fitted line in Fig. 6.2 were experiments with a lower supersaturation, and vice versa.

That there is a dependence on supersaturation can be seen clearly in a graph of the ratio of experimental and theoretical nucleation rates versus the supersaturation: Figure 6.3. In the top graph, we see two effects at the same time; first, the well-established effect of temperature, which causes jumps from one isothermal data set to the next (which is why the five sets can be distinguished easily) and second, the proposed supersaturation dependence, which causes each isothermal set to have a downward slope. This negative slope is the reason that experiments with a high supersaturation are lower in Fig. 6.2. The 'scatter' in this figure can be seen as a 'side view' of each set in Fig. 6.3.

A nice property of Wölk's data is that the entire supersaturation range is covered; some supersaturation values are even included in two isothermal sets. It is precisely this property that allowed us to find the exact form of the supersaturation dependence. Namely, we shifted each isothermal set vertically until it touched – or overlapped – an adjacent set; see the bottom graph of Fig. 6.3. One way to view this process is that we 'normalize' the different isothermal sets to one, arbitrary temperature, so that the only effect that remains is the pure supersaturation effect. It is however only allowed to do this when the supersaturation effect itself does not depend on the temperature, and we assumed that this is the case.

It appeared from Fig. 6.3 that the supersaturation dependence was linear (when plotted on this logarithmic scale); in a plot of $\ln(J_{exp}/J_{stan})$ versus S, the slope that was found was -0.38 ± 0.08. The uncertainty is caused by the shifting of the isotherms 'by hand' which is rather inaccurate. When it was found that the effect was
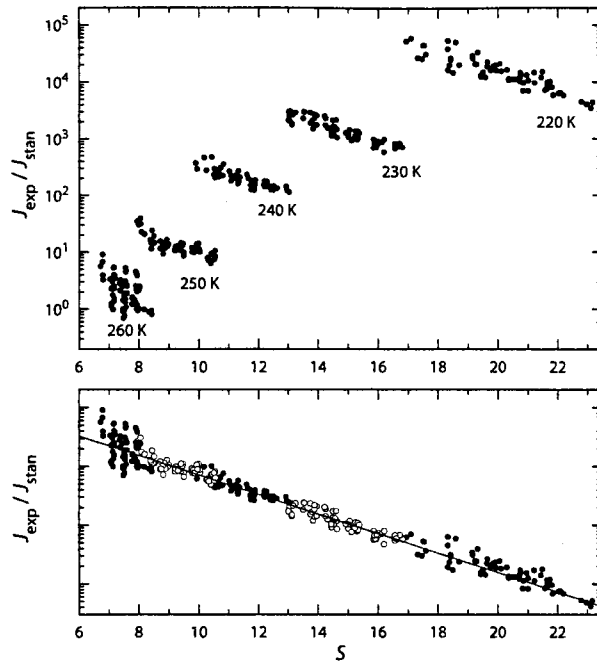
Figure 6.3: Ratio of experimental and theoretical nucleation rates as a function of supersaturation; data of Wölk *et al.* In the bottom graph the isotherms have been shifted vertically – normalizing them to a single temperature – to show the pure supersaturation dependence.

Table 6.1: Slope of the supersaturation dependence of $\ln(J_{exp}/J_{stan})$ of each isotherm of the data by Wölk *et al.* The slopes were obtained by linear regression; the uncertainty shown is the standard deviation.

T	slope of S dependence
220 K	-0.380 ± 0.022
230 K	-0.368 ± 0.022
240 K	-0.358 ± 0.028
250 K	-0.366 ± 0.038
weighted average	-0.37 ± 0.01

linear, the accuracy of the slope was improved by fitting a line to each individual isothermal set. Table 6.1 shows the resulting slopes and their uncertainties, obtained by linear regression. Remarkably, the slope values are consistent; the weighted average and final result is -0.37 ± 0.01. The $T = 260$ K set was not included because of its limited supersaturation range and large scatter.

Since the dependence on supersaturation of the data was known, the theory could be corrected for it:

$$J_{corr,2}^{S} = \exp(CS) J_{stan}. \tag{6.6}$$

This expression is introduced to include the supersaturation dependence; it is not meant to produce exact nucleation rates. Its use becomes clear in Fig. 6.4, where we plotted the ratio of the experimental rates and the supersaturation-corrected values of Eq. 6.6. By scaling the data in this way, we compensate for the supersaturation dependence; what remains is the 'pure' temperature dependence, which is stronger than before. This is because in the original data, the supersaturation and temperature dependence compensated each other: at low temperatures, where the nucleation rate is much higher than the theoretical value, the supersaturation is high as well, so that
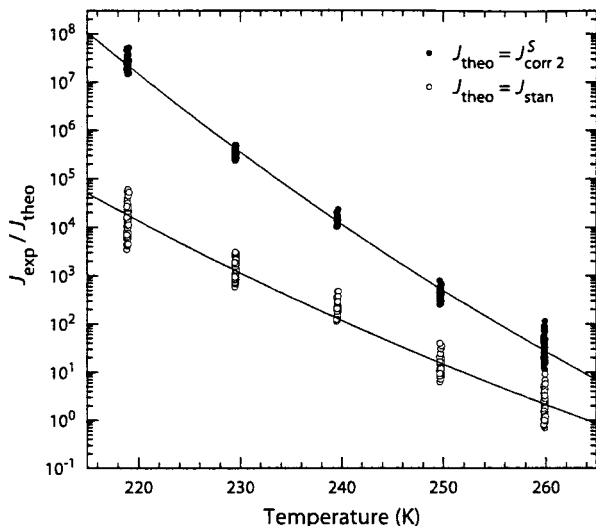
Figure 6.4: Ratio of experimental and theoretical nucleation rates; data by Wölk *et al.*, for the standard theory (open circles) and for the supersaturation-corrected theory (filled circles) Fits in the form of $A + B/T$ are shown (lines).

Table 6.2: Constants in the temperature and supersaturation corrections, with standard deviation.

parameter	value	standard deviation
A_1	-47.4	$\pm$ 0.5
B_1 (K^{-1})	1.25×10^4	$\pm$ 0.01×10^4
A_2	-69.4	$\pm$ 0.3
B_2 (K^{-1})	1.889×10^4	$\pm$ 0.008×10^4
C	-0.37	$\pm$ 0.01
A_3	-12.7	$\pm$ 0.6
B_3 (K^{-4})	7.1×10^{10}	$\pm$ 0.1×10^{10}
A_4	-62	$\pm$ 2
B_4 (K^{-1})	1.93×10^4	$\pm$ 0.04×10^4
D	-5.55	

the ratio of experimental and theoretical rates moves down.

We recalculated the temperature correction; the new expression, including the supersaturation correction, is:

$$J^{T,S}_{\text{corr},2} = \exp(A_2 + B_2/T)\exp(CS)J_{\text{stan}}, \tag{6.7}$$

where we have chosen the same form for the temperature correction as before.

Again, the constants are shown in Table 6.2 and the fit in Fig. 6.4. To show once more the differences between the temperature-only correction (Eq. 6.5) and the correction that includes the supersaturation (Eq. 6.7), Fig. 6.5 displays the ratio of the experimental nucleation rates and the predictions, for each of the two corrections. We see again that the supersaturation dependence has been successfully eliminated and that the maximum deviations have become smaller – the scatter that remains is truly due to experimental noise.
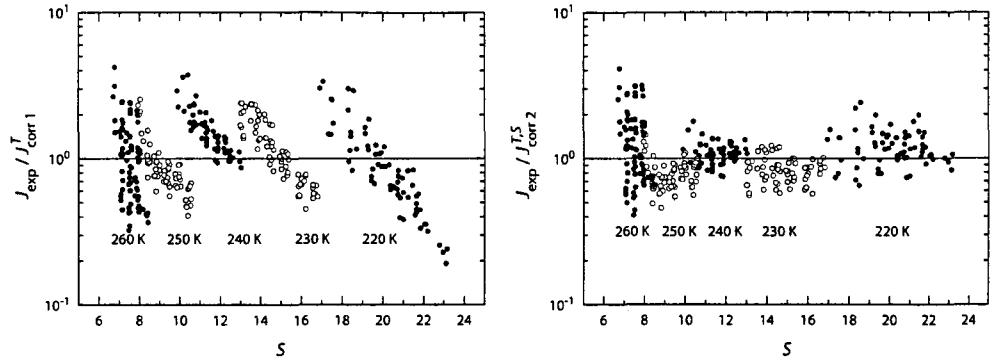
Figure 6.5: Deviations of experimental nucleation rates of Wölk*et al.* from the corrected theories. Left: temperature-corrected theory; right: temperature- and supersaturation-corrected theory.

6.1.3 Application to other data

When the supersaturation correction of Wölk's data had been obtained, a logical next step was to apply it to Peeters's data and our new data as well. Figure 6.6b shows the result: the ratio of J_{exp} and J_{corr}^S versus the temperature. A comparison with the original results (Fig. 6.6a) shows two differences. First, the three data sets move closer together. The new data and Wölk's nearly overlap; Peeters's results are also closer, but still somewhat higher. Second, the scatter in all data sets decreases. For Wölk's data this is no surprise; but that we observe it for the other data sets as well means that they have a similar supersaturation dependence.

It appears that the remaining temperature dependence of our new data set and that of Peeters is slightly larger than that of Wölk's data; an attempt to describe it by the $1/T$ function we used before was unsatisfactory, because the curvature of the fitted function was too small. In fact, a fourth power of T was required to reproduce the dependency, and the full correction is

$$J_{corr,3}^{T,S} = \exp(A_3 + B_3/T^4)\exp(CS)J_{stan}, \tag{6.8}$$

where the constants can be found in the table and the fit is displayed in Fig. 6.6b.

6.1.4 Alternative supersaturation correction

Although the supersaturation correction seems to be an improvement, it has one problem: it is too strong. This is shown in Fig. 6.7, which displays the nucleation rate (not a ratio, but the pure rate this time) as a function of the supersaturation. The data of Wölk is shown, together with the predictions of the T-corrected and the T, S-corrected theories. The slope of the T, S-corrected theory clearly matches the data better, but at high supersaturations this theory predicts a *decreasing* nucleation rate with increasing supersaturation. This behaviour is of course unphysical. According to the Nucleation Theorem[3]

$$\frac{\partial \ln J_{exp}}{\partial \ln S} = n_{exp}^* + 1, \tag{6.9}$$

where J_{exp} is the experimental nucleation rate and n_{exp}^* is the actual amount of molecules in the critical cluster.so that a slope of approximately zero in the J versus S
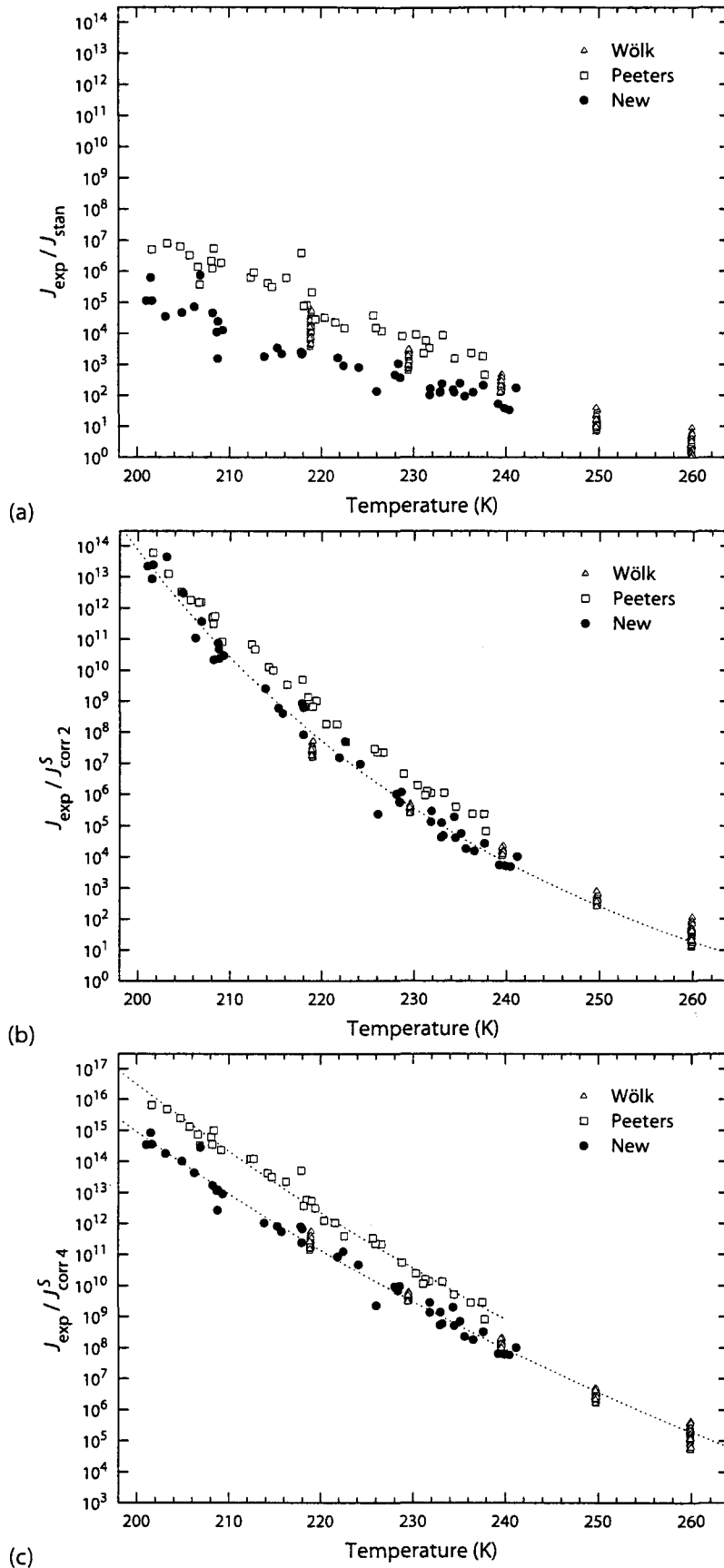
Figure 6.6: Ratio of experimental and theoretical nucleation rates; comparison of different corrections. a: standard theory; b: strong supersaturation correction; c: weak supersaturation correction.
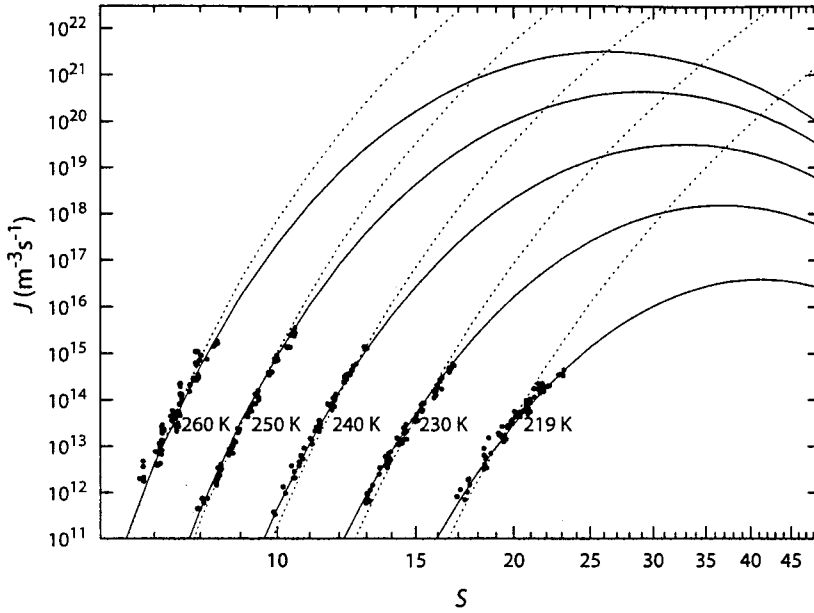
Figure 6.7: Nucleation rates as a function of supersaturation. The theory corrected for temperature and supersaturation $J_{\text{corr},2}^{T,S}$ (solid lines) fits the Wölk data (dots) better than the temperature-corrected theory $J_{\text{corr},1}^{T}$ (dashed lines), but at high supersaturations it predicts the unrealistic decrease of the nucleation rate.

plot means that each molecule in the vapour is a critical cluster; a limit of stability, which could be seen as the spinodal. A negative slope has no physical meaning.

In the standard theory, the critical cluster size is (Eq. 2.21)

$$n_{\text{stan}}^{*} = \left(\frac{2\,\Theta}{3 \ln S} \right)^{3}. \tag{6.10}$$

Taking the logarithm of the expression for the standard theory (Eq. 2.41), and then differentiating with respect to $\ln S$ yields

$$\frac{\partial \ln J_{\text{stan}}}{\partial \ln S} = n_{\text{stan}}^{*} + 1, \tag{6.11}$$

so that we obtain for the T, S-corrected expression, using either Eq. 6.7 or Eq. 6.8,

$$\frac{\partial \ln J_{\text{corr},3}^{T,S}}{\partial \ln S} = n_{\text{stan}}^{*} + 1 + CS. \tag{6.12}$$

Since the T, S-corrected theory agrees with the experimental nucleation rates, the Nucleation Theorem of Eq. 6.9 can be used to obtain the critical cluster size:

$$n_{\text{exp}}^{*} = \frac{\partial \ln J_{\text{corr},3}^{T,S}}{\partial \ln S} - 1 = n_{\text{stan}}^{*} + CS. \tag{6.13}$$

This equation shows that the classical critical size is corrected by an amount CS. Since $C < 0$, at high enough S values the corrected critical size will eventually be zero. We do not expect that this is the case in reality; after all, experiments have been performed at much higher supersaturations.

Whatever the theoretical interpretations may be, it is clear that the supersaturation correction in the previous form is too strong, at least when extrapolated to higher supersaturation values. Therefore, a weaker supersaturation correction was considered:

$$J_{\text{corr},4}^{S} = \exp(D \ln S)\, J_{\text{stan}} = S^{D}\, J_{\text{stan}}, \tag{6.14}$$

where $D < 0$. We wanted the new expression to agree as well as possible with Wölk's data in a $\ln(J_{exp}/J_{stan})$ plot similar to Fig. 6.3. In this plot, the previous correction has a constant slope of C, while the new correction has the form $D \ln S$ with a varying slope of D/S. A full agreement is therefore never possible. We chose to match the two slopes at a single supersaturation value that we call S', so that

$$D = C S'. \tag{6.15}$$

We took $S' = 15$, which is close to the centre of Wölk's experimental supersaturation range; this yielded $D = -5.55$.

For this weaker correction, the critical size is

$$n_{exp}^* = \frac{\partial \ln J_{corr,4}^S}{\partial \ln S} - 1 = n_{stan}^* + D, \tag{6.16}$$

so that a constant amount of about 6 molecules is subtracted from the classical critical cluster size. This means that we will have the same problem of a vanishing slope when the classical critical size is about 6, but this only happens at extremely high supersaturations.

The result of the new correction is shown in Fig. 6.6c. At low temperatures, the new data and those of Peeters do not overlap like they did in the case of the previous supersaturation correction (Fig. 6.6b). Still, the scatter is considerably lower than in the uncorrected case of Fig. 6.6a. Another change is that the Wölk data better follows our results; Wölk's three data sets at 220, 230 and 240 K completely agree with our data.

The temperature dependence of the results in Fig. 6.6c is less curved than in Fig. 6.6b, so that we could use a $1/T$ correction again:

$$J_{corr,4}^{T,S} = \exp(A_4 + B_4/T)S^D J_{stan}. \tag{6.17}$$

The constants A_4 and B_4 were obtained by fitting to the new data only. The result is also shown in Fig. 6.6c together with a similar fit through Peeters's data.

To compare the two types of corrections, Eqs. 6.8 and 6.17, Figure 6.8 shows the remaining deviations. It can be seen that the second correction succeeds even better in reducing the scatter at low temperatures than the first one. The three data sets of
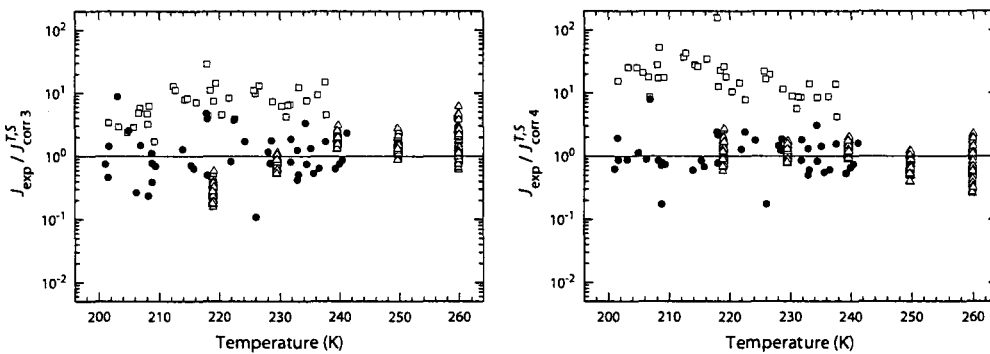
Figure 6.8: Deviations of experimental nucleation rates from the corrected theories. Left: strong supersaturation correction; right: weak supersaturation correction.

Wölk at 200, 230 and 240 K are well described by the second correction; the two data sets at high temperature deviate somewhat from the prediction. An explanation is that we chose $S' = 15$, the centre of the experimental range. The sets at 250 and 260 K are at $S < S'$ and therefore our new supersaturation correction is too strong in this case; the two sets are shifted down too much.

6.2 Nucleation theories

Figure 6.9 shows our experimental data together with those by Peeters and by Wölk et al., scaled with the predictions of four theories: the standard theory, the one by Girshick and Chiu (GC), the Reiss-Kegel-Katz theory (RKK), and a recent theory by Hrubý.[60] Although the differences between the theories are large, no theory gives the correct nucleation rate for an extended temperature range. Still, we can express the quality of a theory by two parameters: first, the average absolute deviation of the rates, and second, the slope of the temperature dependence of the scaled rates. There is no significant difference in the supersaturation dependence; if there were, we would see a difference in the amount of scatter.

The theory by Kashchiev could not be evaluated because the spinodal pressure of water was not known. A literature search yielded no results. The author then tried to find the spinodal pressure from an equation of state, but since water is such an unusual substance, it is hard to find a suitable equation of state. The 'cubic plus association' (CPA) equation of state[61] was chosen because it takes into account the hydrogen bonding between water molecules. Complicated equations of state like this have several adjustable parameters; the CPA has five. The values of these parameters must be determined by fitting the model to known equilibrium properties; in this case the vapour pressure and the liquid density. The problem that the author encountered was that water's properties could be well represented with a broad range of parameter values. The spinodal pressure, however, varied much in this range of parameter space, so it could not be determined.

The GC theory is closest to the experimental nucleation rates. The Hrubý theory
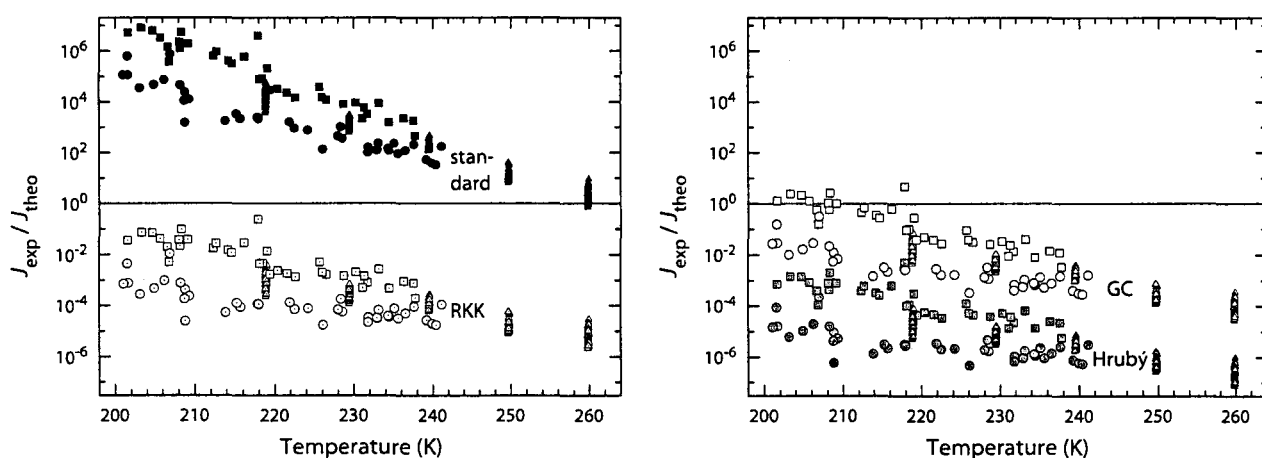
Figure 6.9: Experimental data of this work (circles), Peeters (squares) and Wölk et al.(triangles), scaled with the standard theory, the Girshick and Chiu theory (GC), the Reiss-Kegel-Katz theory (RKK), and the theory by Hrubý.[60]

has the largest absolute deviation, averaged over the entire temperature range.

Looking at the temperature dependence, the standard theory clearly has the largest slope. The GC and RKK theories both show a smaller slope, and the Hrubý theory has the best temperature dependence.

The supersaturation dependence of all theories is nearly the same, so that the supersaturation correction is also the same for all theories, and equal to the form derived in the previous section. After this correction is applied, the temperature dependence of all theories changes strongly; it becomes considerably less accurate. If we return to Fig. 6.6a (not corrected); the difference between the ratio of nucleation rates at low and high temperature is about six orders of magnitude, when we only include the new data and Wölk's data. In Fig. 6.6c (weak S correction) this difference has increased to ten orders of magnitude.

For all theories in Fig. 6.9, the supersaturation correction influences the temperature dependence in the same way. For example, for the Hrubý theory, the difference between the ratios at low and high temperature is about three orders of magnitude (again only considering the new data and Wölk's). When the weak S correction is applied, this difference increases to seven orders. We will come back to this issue in the discussion.

7. Conclusions & Discussion

The objective of this research was to obtain a reliable measurement set of homogeneous nucleation rates of water, at temperatures between 200–240 K, and at near-atmospheric pressure. One of the reasons was that earlier data by Peeters[21] showed interesting behaviour at a temperature of 207 K; below this temperature vapour-to-solid nucleation seemed to occur instead of vapour-to-liquid nucleation. At higher temperatures there was a substantial difference with the measurements of Wölk et al.,[12] which led to doubts concerning the reliability of Peeters's data in the entire temperature range. For example, it was suspected that thermal boundary layers could have influenced the results.

An investigation by the current author revealed a mistake in Peeters's data processing method. It was possible to correct the measurements for this error, and the corrected results did not show a transition in nucleation behaviour. They were also much closer to the measurements by Wölk et al. than the original results had been.

The measurement set of the present work deviated somewhat from Peeters's data, although the temperature trends of both data sets were the same. The new data also did not entirely agree with the data by Wölk et al.

The search for an expression that could accurately reproduce the measurements by Wölk et al. led to a correction of the supersaturation dependence of the classical nucleation theory. When this corrected theory was used to analyze the new data, it was then found to agree with the results of Wölk et al., and the apparent original difference could be fully attributed to a difference in the experimental supersaturations. The validity of the supersaturation correction was further supported by the fact that it reduced the scatter of both Peeters's data and the new data. There remained a difference between the new data and Peeters's, which is believed to be caused by inaccuracies of the calibration of the dynamic pressure transducer.

We have shown that the correction of the theoretical supersaturation dependence can be seen as a correction of the theoretical critical cluster size. The fact that such a correction is required is not surprising, because in most theories small clusters are viewed as drops with macroscopic properties (the capillarity approximation); a questionable assumption, certainly in the case of clusters of a few dozen molecules.

Despite the plausibility of a supersaturation correction, almost all empirical and theoretical expressions use the classical dependence on supersaturation. Even the recent theory of Kashchiev, which takes into account the influence of a spinodal, results in a correction factor which only depends on the temperature.

An effect of the supersaturation correction is that the temperature dependence of all theories more strongly deviates from experimental observation. For example, if a theory is correct at some temperature, then the deviation at a second temperature, 60 degrees lower, can be as much as a factor 10^{10}. This serious discrepancy may have one of the following causes:

First, the error in the supersaturation and temperature dependencies might repres-

ent the failure of the capillarity approximation. As the temperature goes down and the supersaturation increases, the critical cluster becomes smaller, and its properties differ more from the bulk values. This would then explain the rapid increase of the deviation of nucleation theories with decreasing temperature.

Second, the effects could be a property of water, in the sense that at low temperatures a special form of water nucleates from the vapour; a substance with properties that are very different from those of liquid water. It is even possible that ice is directly formed from the vapour, instead of supercooled liquid water. However, we do not believe that this is the case, because at temperatures as low as 233 K the observed scattering indicates a refractive index of at least 1.325. At this temperature, ice is believed to have a refractive index of about 1.31, so it seems unlikely that ice was formed in our experiments.

To obtain a reliable and more accurate supersaturation correction, the analysis of more experimental data is required. From the data set that was observed using our experimental setup, it was not possible to directly determine the supersaturation correction, because we did not perform isothermal measurements (experiments at the same temperature but with different supersaturations). Only from such data sets, the true supersaturation dependence of the nucleation rate can be found, so it would be preferable to perform such experiments, especially at low temperatures near 200 K.

References

[1] H. Reiss, W. K. Kegel, and J. L. Katz, *J. Phys. Chem. A* **102**, 8548 (1998).

[2] C. C. M. Luijten, *Nucleation and droplet growth at high pressure*, Ph.D. thesis, Eindhoven University of Technology (1998).

[3] D. Kashchiev, *Nucleation; Basic Theory with Applications* (Butterworth-Heinemann, Oxford, 2000).

[4] D. Chandler, *Introduction to Modern Statistical Mechanics* (Oxford University Press, 1987).

[5] J. Lothe and G. M. Pound, *J. Chem. Phys.* **36**, 2080 (1962).

[6] H. Reiss, J. L. Katz, and E. R. Cohen, *J. Chem. Phys.* **48**, 5553 (1968).

[7] R. Kikuchi, *Adv. Colloid Interface Sci.* **7**, 67 (1977).

[8] H. Reiss, *Adv. Colloid Interface Sci.* **7**, 1 (1977).

[9] H. Reiss, W. K. Kegel, and J. L. Katz, *Phys. Rev. Lett.* **78**, 4506 (1997).

[10] R. Becker and W. Döring, *Ann. Phys.* **24**, 719 (1935).

[11] S. L. Girshick and C.-P. Chiu, *J. Chem. Phys.* **93**, 1273 (July 1990).

[12] J. Wölk and R. Strey, *J. Phys. Chem. B* **105**, 11683 (2001).

[13] G. J. M. Koper and H. Reiss, *J. Phys. Chem.* **100**, 422 (1996).

[14] D. Kashchiev, *J. Chem. Phys.* **118**, 1837 (2002).

[15] I. Kusaka, *J. Chem. Phys.* **118**, 5510 (2003).

[16] G. S. Kell, *J. Chem. Eng. Data* **12**, 66 (1967).

[17] C. M. Sorensen, *J. Chem. Phys.* **79**, 1455 (1983).

[18] D. E. Hare and C. M. Sorensen, *J. Chem. Phys.* **87**, 4840 (1987).

[19] R. J. Speedy and C. A. Angell, *J. Chem. Phys.* **65**, 851 (1976).

[20] IAPWS, *Release on the IAPWS Formulation 1995 for the Thermodynamic Properties of Ordinary Water Substance for General and Scientific Use* (September 1996), URL http://www.iapws.org/relguide/IAPWS95.pdf.

[21] P. Peeters, J. J. H. Gielis, and M. E. H. van Dongen, *J. Chem. Phys.* **117**, 5647 (2002).

[22] O. Mishima and H. E. Stanley, *Nature* **396**, 329 (1998).

[23] M. Vedamuthu, S. Singh, and G. W. Robinson, *J. Phys. Chem.* **98**, 2222 (1994).

[24] G. S. Kell, *J. Chem. Eng. Data* **20**, 97 (1975).

[25] K. N. H. Looijmans, *Homogeneous nucleation and droplet growth in the coexistence region of n-alkane/methane mixtures at high pressures*, Ph.D. thesis, Eindhoven University of Technology (1995).

[26] M. J. E. H. Muitjens, *Homogeneous condensation in a vapour/gas mixture at high pressures in an expansion cloud chamber*, Ph.D. thesis, Eindhoven University of Technology (1996).

[27] G. Lamanna, *On Nucleation and Droplet Growth in Condensing Nozzle Flows*, Ph.D. thesis, Eindhoven University of Technology (2000).

[28] P. Peeters, *Nucleation and Condensation in Gas-Vapor mixtures of Alkanes and Water*, Ph.D. thesis, Eindhoven University of Technology (2002).

[29] H. R. Pruppacher and J. D. Klett, *Microphysics of Clouds and Precipitation* (Reidel, Dordrecht, Holland, 1978).

[30] R. G. Dorsch and B. Boyd, *X-ray diffraction study of the internal structure of supercooled water*, Technical Note 2532, National Advisory Committee for Aeronautics (October 1951), URL http://naca.larc.nasa.gov/reports/1951/naca-tn-2532/naca-tn-2532.pdf.

[31] J. F. Mohler, *Phys. Rev.* **35**, 236 (1912).

[32] P. T. Hacker, *Experimental values of the surface tension of supercooled water*, Technical Note 2510, National Advisory Committee for Aeronautics (October 1951), URL http://naca.larc.nasa.gov/reports/1951/naca-tn-2510/naca-tn-2510.pdf.

[33] M. A. Floriano and C. A. Angell, *J. Phys. Chem.* **94**, 4199 (1990).

[34] IAPWS, *IAPWS Release on Surface Tension of Ordinary Water Substance* (September 1994), URL http://www.iapws.org/relguide/surf.pdf.

[35] M. Muitjens and K. Looijmans, *Temperatuurafhankelijkheid van enkele grootheden van water, pentaan, nonaan*, Internal report, R-1070-D, Eindhoven University of Technology (1990).

[36] N. B. Vargaftik, *Tables on the Thermophysical Properties of Liquids and Gases* (Wiley, New York, 1975), 2nd edition.

[37] P. E. Wagner, *Aerosol Research III, Wien* p. 209 (1981).

[38] P. R. Lowe and J. M. Ficke, *The computation of saturation vapor pressure*, Tech. Paper No. 4-74, Environmental Prediction Research Facility, Naval Postgraduate School, Monterey, CA (1974).

[39] IAPWS, *Release on the Refractive Index of Ordinary Water Substance as a Function of Wavelength, Temperature and Pressure* (September 1997), URL http://www.iapws.org/relguide/rindex.pdf.

[40] D. G. Labetski, V. Holten, and M. E. H. van Dongen, *J. Chem. Phys.* **120**, 6314 (2004).

[41] W. Wagner and A. Pruß, *J. Phys. Chem. Ref. Data* **31**, 387 (2002).

[42] N. B. Vargaftik, B. N. Volkov, and L. D. Voljak, *J. Phys. Chem. Ref. Data* **12**, 817 (1983).

[43] M. G. Sceats and S. A. Rice, in *Water - A Comprehensive Treatise*, edited by F. Franks (Plenum Press, New York, 1982), volume 7, pp. 83–214.

[44] O. Mishima, L. D. Calvert, and E. Whalley, *Nature* **314**, 76 (1985).

[45] V. P. Shpakov, P. M. Rodger, J. S. Tse, D. D. Klug, and V. R. Belosludov, *Phys. Rev. Lett.* **88**, 155502 (2002).

[46] W. C. Röntgen, *Ann. Phys. Chem.* **45**, 91 (1892).

[47] L. S. Bartell, *J. Phys. Chem. B* **101**, 7573 (1997).

[48] E. G. Ponyatovsky, V. V. Sinitsyn, and T. A. Pozdnyakova, *J. Chem. Phys.* **109**, 2413 (1998).

[49] K. Röttger, A. Endriss, J. Ihringer, S. Doyle, and W. F. Kuhs, *Acta Cryst. B* **50**, 644 (1994).

[50] P. V. Hobbs, *Ice physics* (Oxford University Press, London, 1974).

[51] T. F. Young and W. D. Harkins, in *International Critical Tables*, edited by E. W. Washburn (McGraw-Hill, New York, 1928), volume IV, pp. 446–475.

[52] B. E. Poling, J. M. Prausnitz, and J. P. O'Connell, *The Properties of Gases and Liquids* (McGraw-Hill, New York, 2001), 5th edition.

[53] J. S. Rowlinson and B. Widom, *Molecular theory of capillarity* (Oxford University Press, New York, 1982).

[54] X. Wei, P. B. Miranda, and Y. R. Shen, *Phys. Rev. Lett.* **86**, 1554 (2001).

[55] Y. Viisanen, R. Strey, and H. Reiss, *J. Chem. Phys.* **99**, 4680 (1993).

[56] J. Hrubý, *New mixture-preparation device for investigation of nucleation and droplet growth in natural gas-like systems*, Internal report, R-1489-D, Eindhoven University of Technology (1999).

[57] G. Mie, *Ann. Phys.* **25**, 377 (1908).

[58] H. C. van de Hulst, *Light scattering by Small Particles* (Dover, New York, 1981).

[59] J. Wölk, R. Strey, C. H. Heath, and B. E. Wyslouzil, *J. Chem. Phys.* **117**, 4954 (2002).

[60] J. Hrubý, in *Nucleation and Atmospheric Aerosols, 16th International Conference* (2004, to appear).

[61] E. C. Voutsas, I. V. Yakoumis, and D. P. Tassios, *Fluid Phase Equilibria* **158**, 151 (1999).

A. Data by others

A.1 Peeters

One of the objectives of this research was to confirm the measurements by Peeters *et al.*[21] When it was found that the findings of Peeters could not be reproduced, the current author started to investigate possible causes of the inconsistency. Finally, the source of the problem was traced to a single line of code in the computer program which was used by Peeters to calculate the vapour fraction from the mass flow controller settings. The mistake caused the vapour fraction to be nearly a factor of two lower than the real value, for some experiments. Since the supersaturation S is proportional to the vapour fraction, and the theoretical nucleation rate strongly depends on S, the ratio of experimental and theoretical nucleation rates was about five orders of magnitude too low for some experiments.

Fortunately, the experimental data of Peeters were still available and the correct vapour fraction could be calculated. Other changes that were made:

- The temperatures were recalculated using the corrected c_p/c_v which is influenced by the amount of water vapour in the mixture. Peeters used a c_p/c_v of 1.66592 for all experiments, which corresponds, coincidentally, to that of a mixture with an average vapour fraction. The maximum difference between the original temperatures and the new ones is therefore small: 0.09 K.

- Three errors in the nucleation pressure were found and corrected. Two of them were minor rounding errors, the other one (experiment 484) was a larger error (0.4% deviation).

- One rounding error in the nucleation rate was corrected.

The corrected data is shown in Table A.1.

A.2 Wölk

The data by J.Wölk *et al.* was taken as it appears in the published work,[12] with one modification: In the section labelled 'H$_2$O, Argon 230K, $T_0 = 10\,°C, \bar{\omega}_v = 0.003433$', the molar vapour fraction should be 0.003343 instead of 0.003433. This apparent typing error was discovered when it was found that the values of the supersaturation in this particular section of the table did not agree with the published vapour fraction. A comparison with the original graphs by J.Wölk revealed that the vapour fraction was erroneous, not the supersaturation.

exp	p_0 (bar)	T_0 (K)	p (bar)	T (K)	$y \times 10^4$	J $(\mathrm{m}^{-3}\mathrm{s}^{-1})$
425	1.678	295.75	0.9692	237.58	40.20	3.9×10^{15}
429	1.719	296.65	0.9721	236.31	33.68	3.1×10^{14}
430	1.738	296.65	0.9644	234.49	33.82	7.6×10^{15}
432	1.758	296.55	0.9485	231.76	26.87	3.2×10^{15}
433	1.778	296.45	0.9556	231.34	23.65	4.0×10^{14}
434	1.799	296.55	0.9554	230.30	21.12	1.9×10^{14}
435	1.819	296.45	0.9507	228.79	21.25	4.5×10^{15}
436	1.838	296.55	0.9371	226.57	20.17	7.4×10^{16}
437	1.859	296.55	0.9413	225.98	18.20	2.4×10^{16}
438	1.878	296.55	0.9482	225.67	15.91	3.8×10^{15}
439	1.938	296.45	0.9358	221.60	13.66	8.0×10^{16}
440	1.978	296.35	0.9326	219.42	12.40	4.0×10^{17}
442	1.978	296.65	0.9204	218.48	10.38	9.1×10^{16}
444	1.999	296.65	0.9359	219.04	9.058	4.3×10^{15}
448	2.099	296.45	0.9316	214.22	6.468	3.2×10^{16}
450	2.099	296.15	0.9741	217.89	6.726	8.2×10^{14}
451	2.099	296.15	0.9386	214.68	6.825	4.1×10^{16}
452	2.099	296.15	0.9553	216.20	6.719	3.9×10^{15}
455	2.113	295.95	0.9213	212.35	5.803	1.1×10^{17}
469	2.303	295.25	0.9725	209.15	3.335	2.0×10^{15}
470	2.303	295.35	0.9605	208.19	3.460	1.7×10^{16}
471	2.303	295.45	0.9583	208.07	3.381	2.2×10^{16}
477	2.503	294.85	1.0052	204.70	2.175	9.1×10^{15}
480	2.503	295.15	0.9855	203.30	1.975	1.6×10^{16}
482	2.518	295.45	0.9685	201.62	1.805	3.0×10^{16}
484	2.343	295.65	0.9588	206.82	3.531	9.1×10^{16}
486	2.343	295.45	0.9580	206.62	3.133	4.4×10^{16}
487	2.383	295.55	0.9629	205.71	2.615	1.4×10^{16}
491	2.108	295.65	0.9851	218.13	8.670	1.2×10^{16}
493	2.048	295.75	0.9817	220.42	10.93	1.6×10^{16}
494	1.999	295.85	0.9809	222.61	13.22	1.2×10^{16}
496	2.192	294.45	0.9721	212.71	5.377	5.0×10^{16}
498	1.737	295.45	1.0080	237.76	40.19	2.2×10^{15}
499	1.798	294.85	0.9994	233.19	24.84	1.7×10^{14}
500	1.838	295.05	0.9968	231.11	24.79	3.3×10^{15}
505	5.054	295.25	2.1136	208.33	1.484	1.5×10^{16}

Table A.1: Corrected experimental data of the water-helium experiments of Peeters.

B. New data

exp	p_0 (bar)	T_0 (K)	$y \times 10^4$		p (bar)		T (K)		n (m^{-3})	Δt (ms)	J (m^{-3}s^{-1})
025	1.775	296.75	34.2	± 0.2	0.990	± 0.007	235.1	± 0.4	1.38×10^{11}	0.13	1.1×10^{15}
027	1.775	296.45	35.2	0.2	0.970	0.007	232.9	0.5	4.67×10^{12}	0.16	2.9×10^{16}
028	1.775	296.55	34.8	0.2	0.958	0.007	231.8	0.5	1.70×10^{13}	0.16	1.1×10^{17}
029	1.775	296.95	34.8	0.2	0.994	0.007	235.6	0.4	3.56×10^{10}	0.12	3.0×10^{14}
030	1.775	296.75	33.2	0.2	0.956	0.007	231.8	0.5	2.96×10^{12}	0.13	2.3×10^{16}
031	1.775	297.25	27.9	0.2	0.966	0.007	233.1	0.5	1.10×10^{10}	0.15	7.4×10^{13}
032	1.775	297.25	30.2	0.2	0.964	0.007	232.9	0.5	7.06×10^{10}	0.14	5.1×10^{14}
035	1.663	296.75	36.7	0.2	0.942	0.006	236.5	0.4	9.30×10^{9}	0.16	5.8×10^{13}
039	1.613	296.35	46.2	0.2	0.943	0.006	239.2	0.4	1.76×10^{10}	0.14	1.3×10^{14}
042	1.713	296.95	45.2	0.3	1.017	0.006	241.2	0.4	6.21×10^{9}	0.16	3.9×10^{13}
043	1.853	296.65	45.2	0.3	1.088	0.007	239.9	0.4	1.14×10^{11}	0.13	8.8×10^{14}
044	1.853	296.75	48.1	0.3	1.093	0.007	240.4	0.4	2.62×10^{11}	0.13	2.0×10^{15}
045	1.893	296.75	32.1	0.3	1.049	0.007	234.5	0.4	2.20×10^{11}	0.14	1.6×10^{15}
046	1.913	296.85	35.5	0.3	1.095	0.007	237.6	0.4	5.90×10^{10}	0.15	3.9×10^{14}
047	1.903	296.85	38.9	0.3	1.052	0.007	234.3	0.4	3.42×10^{13}	0.13	2.6×10^{17}
048	1.955	296.85	24.8	0.2	1.016	0.008	228.6	0.5	8.20×10^{12}	0.12	6.8×10^{16}
049	1.955	296.95	22.5	0.2	1.009	0.008	228.0	0.5	2.43×10^{12}	0.13	1.9×10^{16}
050	1.955	296.95	19.0	0.2	1.013	0.008	228.4	0.5	4.36×10^{10}	0.12	3.6×10^{14}
051	2.015	296.75	18.1	0.2	0.999	0.008	224.2	0.5	6.16×10^{12}	0.08	7.7×10^{16}
052	2.013	296.85	17.6	0.2	0.978	0.008	222.5	0.6	3.56×10^{13}	0.09	4.0×10^{17}
053	2.015	297.05	13.9	0.2	0.971	0.008	221.9	0.6	1.12×10^{12}	0.10	1.1×10^{16}
054	2.095	296.65	12.0	0.2	0.968	0.008	217.8	0.6	3.33×10^{13}	0.09	3.7×10^{17}
055	2.095	296.85	9.0	0.1	0.943	0.009	215.7	0.6	2.46×10^{12}	0.12	2.1×10^{16}
058	2.095	296.75	12.0	0.2	0.969	0.008	218.0	0.6	3.18×10^{13}	0.11	2.9×10^{17}
059	2.095	296.25	10.0	0.1	0.972	0.008	218.0	0.6	9.14×10^{11}	0.10	9.1×10^{15}
060	2.095	296.05	8.5	0.1	0.944	0.009	215.3	0.6	2.60×10^{12}	0.13	2.0×10^{16}
062	2.407	296.25	4.00	0.09	1.00	0.01	208.8	0.7	4.97×10^{11}	0.09	5.5×10^{15}
066	2.407	295.85	4.50	0.06	1.01	0.01	209.3	0.7	1.52×10^{12}	0.10	1.5×10^{16}
067	2.407	295.75	3.51	0.06	1.00	0.01	208.2	0.7	1.96×10^{11}	0.10	2.0×10^{15}
068	2.639	295.85	2.91	0.06	1.05	0.01	204.9	0.7	3.74×10^{12}	0.09	4.2×10^{16}
069	2.639	296.35	2.74	0.07	1.07	0.01	206.9	0.7	9.19×10^{11}	0.10	9.2×10^{15}
070	2.639	296.25	2.74	0.07	1.07	0.01	206.2	0.7	3.93×10^{11}	0.15	2.6×10^{15}
073	2.659	296.45	2.04	0.07	1.01	0.01	201.7	0.8	1.61×10^{12}	0.10	1.6×10^{16}
074	2.659	296.35	1.72	0.06	1.01	0.01	201.5	0.8	5.93×10^{11}	0.14	4.2×10^{15}
075	2.659	296.20	1.87	0.06	1.01	0.01	201.0	0.8	1.05×10^{12}	0.13	8.1×10^{15}
077	2.106	297.25	8.6	0.2	0.924	0.009	213.9	0.6	6.34×10^{12}	0.10	6.3×10^{16}
082	2.617	296.65	2.75	0.06	1.02	0.01	203.1	0.8	8.62×10^{12}	0.10	8.6×10^{16}
083	2.403	296.85	4.52	0.07	1.00	0.01	208.7	0.7	2.47×10^{12}	0.09	2.7×10^{16}
084	2.400	296.85	5.02	0.07	1.00	0.01	208.8	0.7	1.94×10^{12}	0.09	2.2×10^{16}
087	1.939	296.05	17.9	0.2	0.987	0.008	226.1	0.5	5.41×10^{10}	0.13	4.2×10^{14}

Table B.1: Experimental data of this work.

B.1 Vapour fraction

exp	p_{sat} bar	T_{sat} K	Q_g L/min	$\varepsilon(Q_g)$ %	Q_0 L/min	$\varepsilon(Q_0)$ %	$y \times 10^4$	$\varepsilon(y)$ caused by (in %) p_{sat}	T_{sat}	Q_g	Q_0	$\varepsilon(y)$ %
025	5.20	290.53	3.91	1.0	0.48	2.6	34.2	0.4	0.1	0.1	0.3	0.5
027	5.20	295.82	3.80	1.0	1.95	1.2	35.2	0.4	0.1	0.3	0.4	0.7
028	5.20	295.83	4.20	0.9	2.23	1.1	34.8	0.4	0.1	0.3	0.4	0.7
029	5.20	295.82	3.37	1.0	1.79	1.2	34.8	0.4	0.1	0.3	0.4	0.7
030	5.20	295.36	3.20	1.0	1.80	1.2	33.2	0.4	0.1	0.4	0.4	0.7
031	5.20	295.82	2.59	1.1	2.35	1.1	27.9	0.4	0.1	0.5	0.5	0.8
032	5.20	295.82	2.83	1.1	2.16	1.2	30.2	0.4	0.1	0.5	0.5	0.8
035	5.20	292.15	4.31	0.9	0.67	2.1	36.7	0.4	0.1	0.1	0.3	0.5
039	4.35	290.68	2.79	1.1	0.00	—	46.2	0.5	0.1	0.0	0.0	0.5
042	3.98	290.68	3.42	1.0	0.40	3.0	45.2	0.5	0.1	0.1	0.3	0.6
043	3.98	290.67	3.05	1.0	0.36	3.3	45.2	0.5	0.1	0.1	0.3	0.6
044	3.98	290.67	3.60	1.0	0.17	6.0	48.1	0.5	0.1	0.0	0.3	0.6
045	3.98	290.68	2.18	1.1	1.26	1.5	32.1	0.5	0.1	0.4	0.5	0.9
046	3.98	290.68	2.40	1.1	1.02	1.6	35.5	0.5	0.1	0.3	0.5	0.8
047	4.00	290.68	2.65	1.1	0.77	1.9	38.9	0.5	0.1	0.2	0.4	0.7
048	5.04	290.69	2.39	1.1	1.46	1.4	24.8	0.4	0.1	0.4	0.5	0.8
049	5.00	290.68	1.92	1.2	1.52	1.3	22.5	0.4	0.1	0.5	0.6	0.9
050	6.00	290.69	1.72	1.3	1.32	1.4	19.0	0.3	0.1	0.5	0.6	0.9
051	6.00	290.68	1.80	1.2	1.55	1.3	18.1	0.3	0.1	0.6	0.6	0.9
052	6.00	290.68	1.77	1.2	1.60	1.3	17.6	0.3	0.1	0.6	0.6	0.9
053	6.00	290.69	1.40	1.4	1.99	1.2	13.9	0.3	0.1	0.8	0.7	1.1
054	6.00	290.68	1.20	1.5	2.17	1.2	12.0	0.3	0.1	1.0	0.7	1.3
055	6.00	290.69	0.86	1.8	2.33	1.1	9.0	0.3	0.1	1.3	0.8	1.6
058	6.00	290.67	1.19	1.5	2.13	1.2	12.0	0.3	0.1	1.0	0.7	1.3
059	6.00	290.67	1.02	1.6	2.39	1.1	10.0	0.3	0.1	1.1	0.8	1.4
060	6.00	290.67	0.88	1.8	2.58	1.1	8.5	0.3	0.1	1.3	0.8	1.6
062	8.00	290.68	0.54	2.4	2.85	1.1	4.00	0.3	0.1	2.1	0.9	2.3
066	14.09	290.68	1.19	1.5	2.61	1.1	4.50	0.1	0.1	1.0	0.7	1.3
067	14.09	290.68	0.77	1.9	2.40	1.1	3.51	0.1	0.1	1.4	0.8	1.7
068	14.09	290.69	0.63	2.2	2.47	1.1	2.91	0.1	0.1	1.7	0.9	2.0
069	14.09	290.68	0.46	2.7	1.94	1.2	2.74	0.1	0.1	2.2	1.0	2.4
070	14.09	290.68	0.44	2.8	1.86	1.2	2.74	0.1	0.1	2.3	1.0	2.5
073	14.09	290.68	0.33	3.5	1.98	1.2	2.04	0.1	0.1	3.0	1.0	3.2
074	14.09	290.68	0.28	4.0	2.04	1.2	1.72	0.1	0.1	3.6	1.0	3.7
075	14.09	290.67	0.30	3.8	2.01	1.2	1.87	0.1	0.1	3.3	1.0	3.4
077	6.00	290.68	0.69	2.1	2.01	1.2	8.6	0.3	0.1	1.5	0.9	1.8
082	14.19	290.67	0.53	2.5	2.20	1.1	2.75	0.1	0.1	2.0	0.9	2.2
083	14.19	290.67	0.78	1.9	1.69	1.3	4.52	0.1	0.1	1.3	0.9	1.6
084	14.17	290.67	0.88	1.8	1.62	1.3	5.02	0.1	0.1	1.1	0.8	1.4
087	6.02	290.68	1.00	1.6	0.87	1.8	17.9	0.3	0.1	0.8	0.8	1.2

Table B.2: Error analysis of the vapour fraction of the experiments of the current work.

B.2 Theoretical nucleation rate

exp	p_0 bar	$y \times 10^4$		T K	$E(^{10}\log J)$ caused by				$E(^{10}\log J)$	f_{err}
					p_0	Δp	T_0	y		
025	1.775	34.2	±0.2	235.1	0.12	0.25	0.07	0.06	0.29	2.0
027	1.775	35.2	0.2	232.9	0.10	0.21	0.05	0.07	0.25	1.8
028	1.775	34.8	0.2	231.8	0.09	0.20	0.05	0.06	0.24	1.7
029	1.775	34.8	0.2	235.6	0.12	0.26	0.07	0.08	0.30	2.0
030	1.775	33.2	0.2	231.8	0.10	0.21	0.05	0.07	0.25	1.8
031	1.775	27.9	0.2	233.1	0.14	0.30	0.07	0.11	0.35	2.3
032	1.775	30.2	0.2	232.9	0.13	0.26	0.06	0.09	0.31	2.1
035	1.663	36.7	0.2	236.5	0.13	0.28	0.07	0.07	0.32	2.1
039	1.613	46.2	0.2	239.2	0.11	0.25	0.07	0.06	0.29	1.9
042	1.713	45.2	0.3	241.2	0.12	0.27	0.08	0.09	0.32	2.1
043	1.853	45.2	0.3	239.9	0.10	0.22	0.06	0.08	0.26	1.8
044	1.853	48.1	0.3	240.4	0.09	0.21	0.06	0.07	0.25	1.8
045	1.893	32.1	0.3	234.5	0.11	0.24	0.06	0.10	0.29	2.0
046	1.913	35.5	0.3	237.6	0.12	0.26	0.07	0.10	0.31	2.0
047	1.903	38.9	0.3	234.3	0.09	0.19	0.05	0.07	0.22	1.7
048	1.955	24.8	0.2	228.6	0.11	0.22	0.05	0.07	0.26	1.8
049	1.955	22.5	0.2	228.0	0.12	0.25	0.05	0.09	0.29	2.0
050	1.955	19.0	0.2	228.4	0.15	0.31	0.07	0.11	0.37	2.3
051	2.015	18.1	0.2	224.2	0.12	0.24	0.05	0.08	0.29	1.9
052	2.013	17.6	0.2	222.5	0.11	0.22	0.04	0.07	0.27	1.8
053	2.015	13.9	0.2	221.9	0.15	0.29	0.05	0.11	0.34	2.2
054	2.095	12.0	0.2	217.8	0.13	0.25	0.04	0.10	0.30	2.0
055	2.095	9.0	0.1	215.7	0.16	0.29	0.05	0.13	0.36	2.3
058	2.095	12.0	0.2	218.0	0.13	0.25	0.04	0.10	0.30	2.0
059	2.095	10.0	0.1	218.0	0.16	0.30	0.05	0.13	0.36	2.3
060	2.095	8.5	0.1	215.3	0.16	0.30	0.05	0.14	0.37	2.3
062	2.407	4.00	0.09	208.8	0.20	0.37	0.05	0.19	0.47	2.9
066	2.407	4.50	0.06	209.3	0.18	0.34	0.05	0.10	0.40	2.5
067	2.407	3.51	0.06	208.2	0.22	0.40	0.06	0.15	0.48	3.0
068	2.639	2.91	0.06	204.9	0.19	0.35	0.05	0.15	0.43	2.7
069	2.639	2.74	0.07	206.9	0.24	0.43	0.06	0.22	0.54	3.5
070	2.639	2.74	0.07	206.2	0.23	0.41	0.06	0.22	0.52	3.3
073	2.659	2.04	0.07	201.7	0.22	0.39	0.05	0.24	0.51	3.3
074	2.659	1.72	0.06	201.5	0.26	0.46	0.06	0.31	0.61	4.1
075	2.659	1.87	0.06	201.0	0.23	0.41	0.05	0.27	0.54	3.5
077	2.106	8.6	0.2	213.9	0.15	0.28	0.04	0.14	0.34	2.2
082	2.617	2.75	0.06	203.1	0.19	0.33	0.04	0.15	0.41	2.6
083	2.403	4.52	0.07	208.7	0.18	0.33	0.05	0.12	0.40	2.5
084	2.400	5.02	0.07	208.8	0.16	0.30	0.04	0.10	0.36	2.3
087	1.939	17.9	0.2	226.1	0.14	0.28	0.06	0.12	0.34	2.2

Table B.3: Error analysis of the theoretical nucleation rate J_{stan} of the standard theory for the experimental conditions of the current work.

C. Vapour pressure from the Hrubý model

This table contains the saturated vapour pressure $p_s(T)$ calculated from an extended version of the Hrubý model.

T (K)	p_s (Pa)	T (K)	p_s (Pa)	T (K)	p_s (Pa)
190	6.751×10^{-2}	227	9.790×10^{0}	264	3.063×10^{2}
191	7.944×10^{-2}	228	1.093×10^{1}	265	3.312×10^{2}
192	9.329×10^{-2}	229	1.218×10^{1}	266	3.579×10^{2}
193	1.094×10^{-1}	230	1.356×10^{1}	267	3.865×10^{2}
194	1.280×10^{-1}	231	1.509×10^{1}	268	4.171×10^{2}
195	1.495×10^{-1}	232	1.677×10^{1}	269	4.498×10^{2}
196	1.743×10^{-1}	233	1.861×10^{1}	270	4.847×10^{2}
197	2.030×10^{-1}	234	2.064×10^{1}	271	5.221×10^{2}
198	2.359×10^{-1}	235	2.287×10^{1}	272	5.620×10^{2}
199	2.736×10^{-1}	236	2.531×10^{1}	273	6.046×10^{2}
200	3.170×10^{-1}	237	2.799×10^{1}	274	6.500×10^{2}
201	3.666×10^{-1}	238	3.092×10^{1}	275	6.984×10^{2}
202	4.232×10^{-1}	239	3.413×10^{1}	276	7.500×10^{2}
203	4.879×10^{-1}	240	3.763×10^{1}	277	8.049×10^{2}
204	5.616×10^{-1}	241	4.146×10^{1}	278	8.634×10^{2}
205	6.454×10^{-1}	242	4.563×10^{1}	279	9.255×10^{2}
206	7.407×10^{-1}	243	5.018×10^{1}	280	9.916×10^{2}
207	8.488×10^{-1}	244	5.514×10^{1}	281	1.062×10^{3}
208	9.712×10^{-1}	245	6.053×10^{1}	282	1.136×10^{3}
209	1.110×10^{0}	246	6.639×10^{1}	283	1.216×10^{3}
210	1.266×10^{0}	247	7.275×10^{1}	284	1.300×10^{3}
211	1.443×10^{0}	248	7.966×10^{1}	285	1.389×10^{3}
212	1.642×10^{0}	249	8.716×10^{1}	286	1.483×10^{3}
213	1.865×10^{0}	250	9.528×10^{1}	287	1.583×10^{3}
214	2.117×10^{0}	251	1.041×10^{2}	288	1.689×10^{3}
215	2.399×10^{0}	252	1.136×10^{2}	289	1.800×10^{3}
216	2.715×10^{0}	253	1.239×10^{2}	290	1.919×10^{3}
217	3.069×10^{0}	254	1.350×10^{2}	291	2.044×10^{3}
218	3.465×10^{0}	255	1.470×10^{2}	292	2.176×10^{3}
219	3.908×10^{0}	256	1.600×10^{2}	293	2.316×10^{3}
220	4.401×10^{0}	257	1.739×10^{2}	294	2.463×10^{3}
221	4.951×10^{0}	258	1.890×10^{2}	295	2.619×10^{3}
222	5.562×10^{0}	259	2.052×10^{2}	296	2.783×10^{3}
223	6.242×10^{0}	260	2.226×10^{2}	297	2.956×10^{3}
224	6.997×10^{0}	261	2.414×10^{2}	298	3.138×10^{3}
225	7.835×10^{0}	262	2.615×10^{2}	299	3.330×10^{3}
226	8.763×10^{0}	263	2.831×10^{2}	300	3.533×10^{3}

Table C.1: Saturated vapour pressure from the Hrubý model of section 3.5.

D. Scattering and extinction graphs

This appendix contains the experimental scattering and extinction signals. The graphs on the left side show the scattering intensity as a function of the time in ms. Extrema that were used in the data analysis have been numbered. Note that the scale of the time axis is different for each experiment.

The graphs on the right side show the ratio of the transmitted light intensity and the initial intensity, $I(t)/I_0$, as a function of the time in ms. The thin line is the experimental signal; the thick line is the expected intensity as described in section 5.3. The first two vertical lines indicate the position of the nucleation pulse. If a third line is present, then the data range that was used to determine n was limited; the third line then indicates the end of the fitting range. This was usually done to limit the fit to an extinction of less than 10%, since multiple scattering begins to play a role at higher extinction values. To illustrate this better, the extinction level $I/I_0 = 0.9$ is indicated by a horizontal line.

Experiment 25
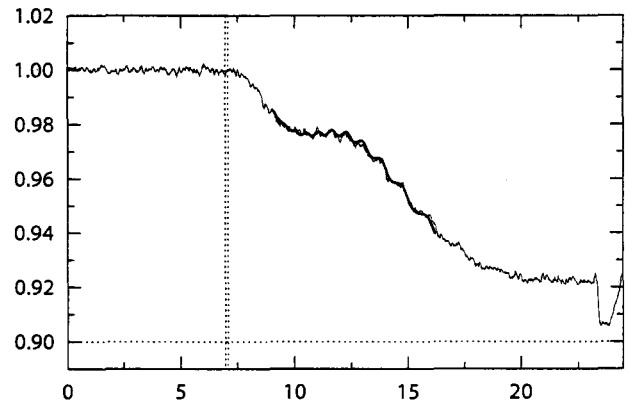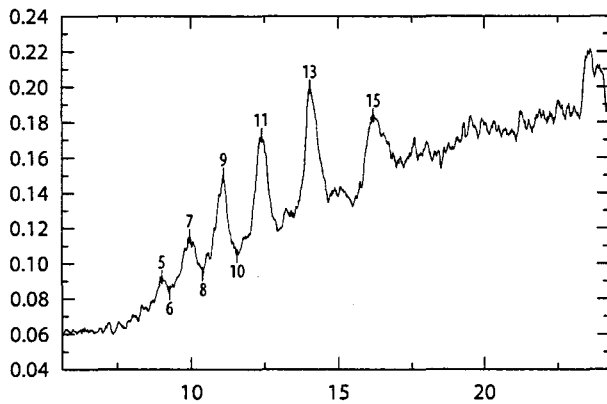
Experiment 27
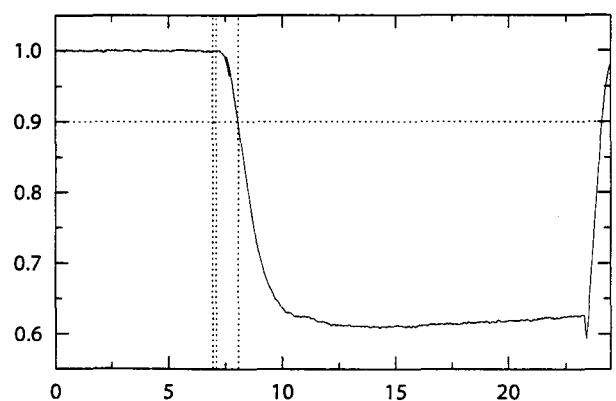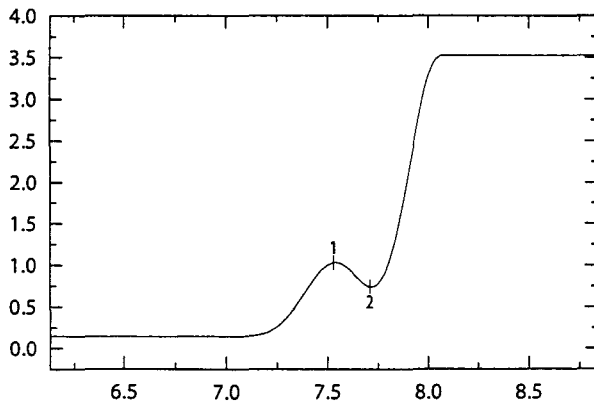
Experiment 28
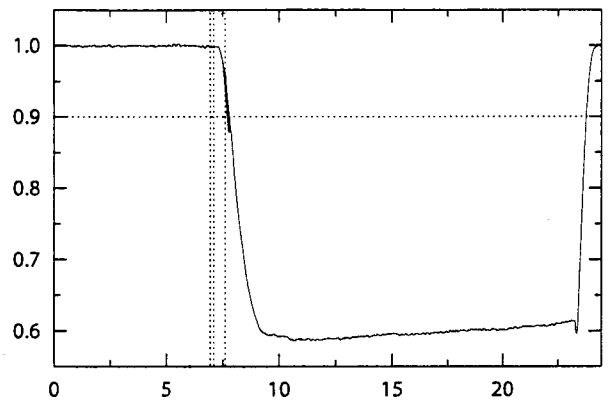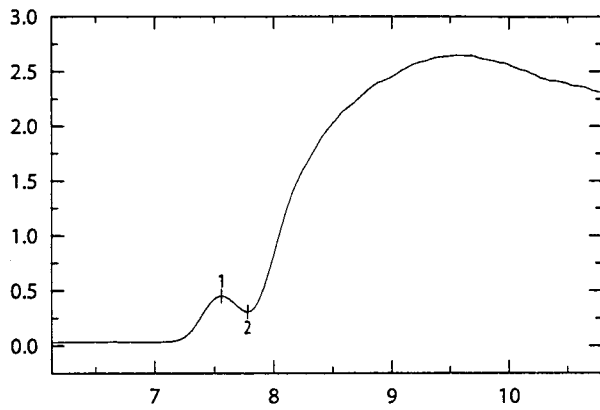
Experiment 29
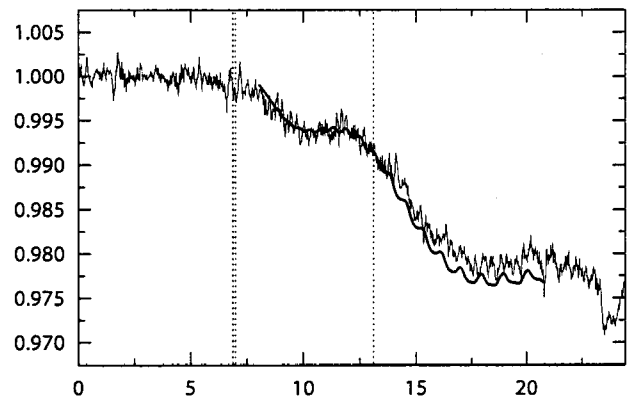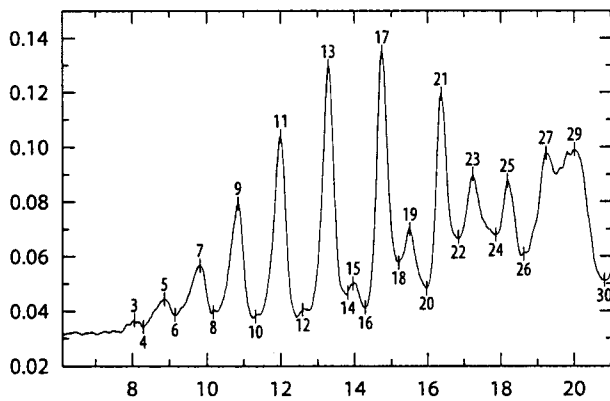
Experiment 30
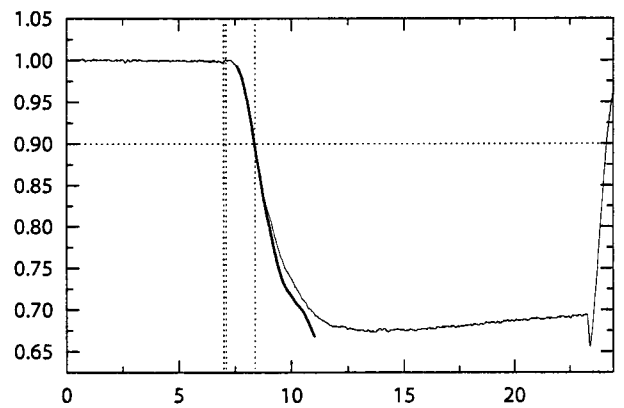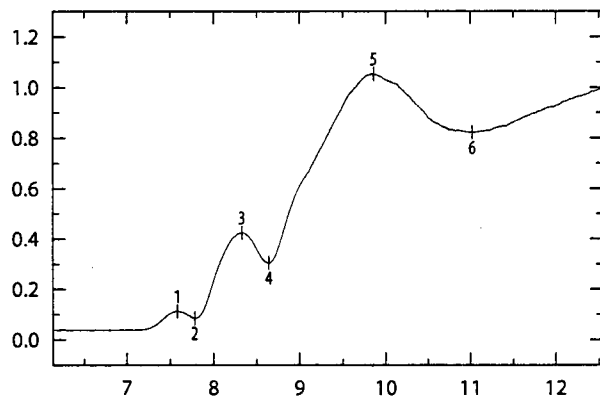
Experiment 31
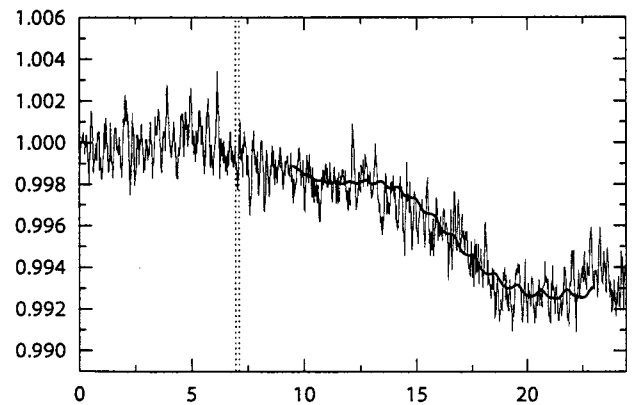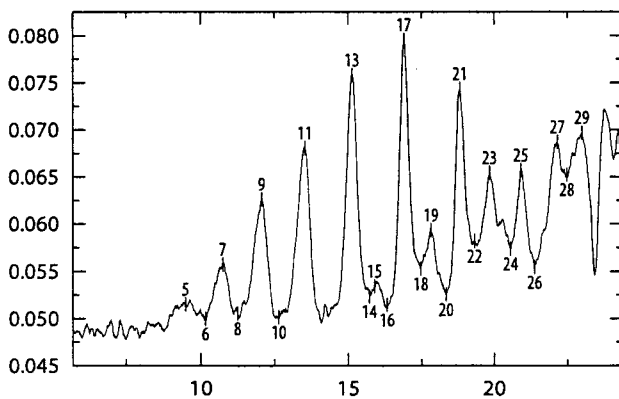
Experiment 32
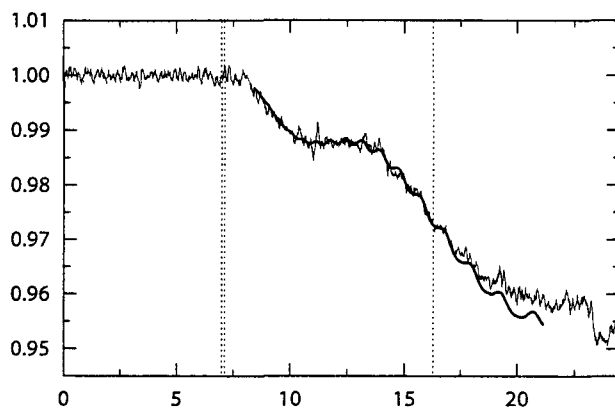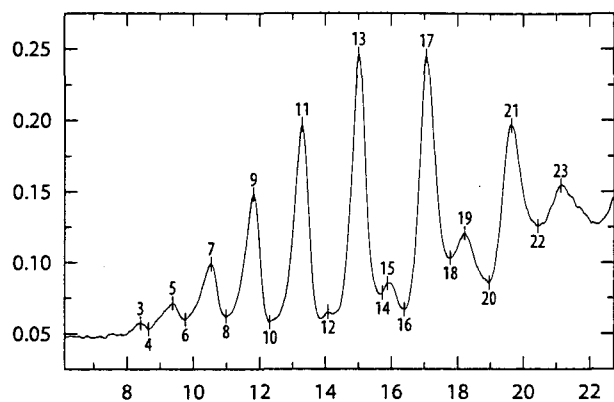
Experiment 35
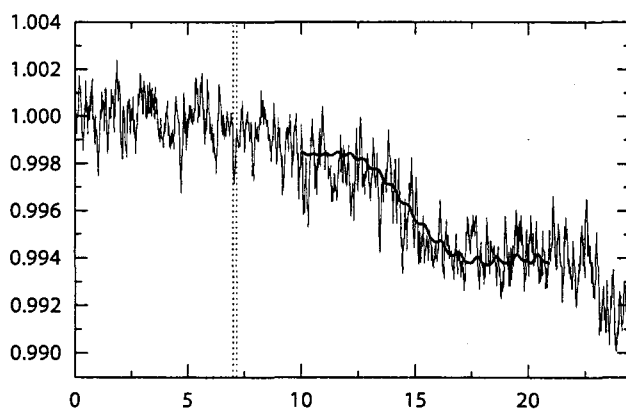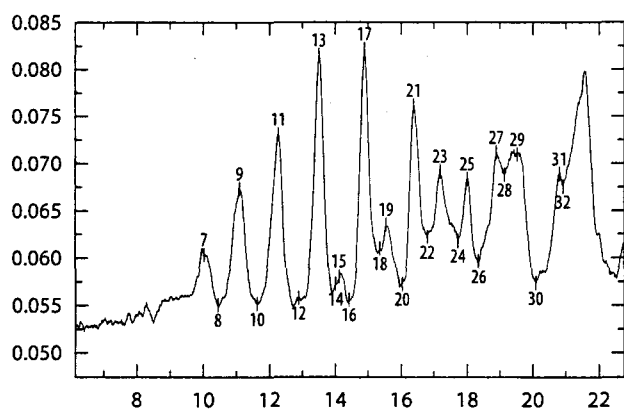
Experiment 39
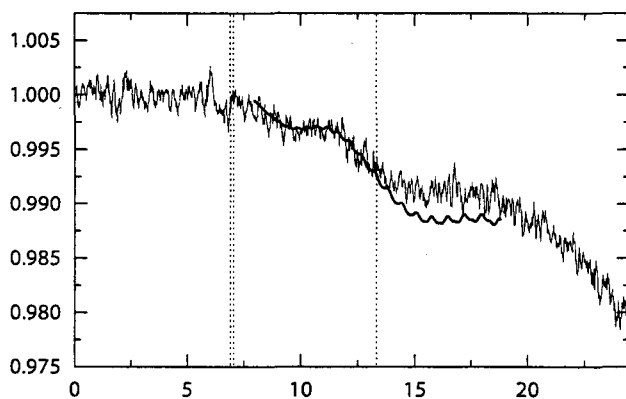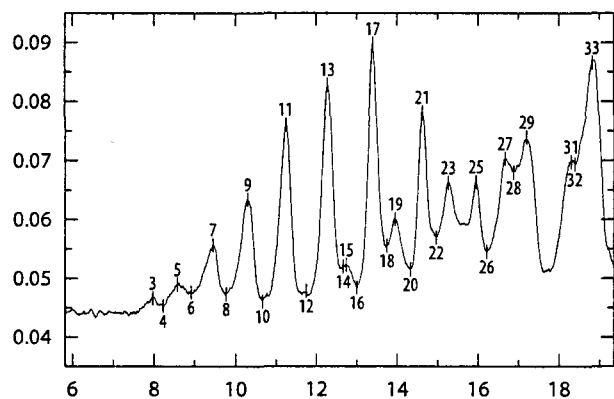
Experiment 42
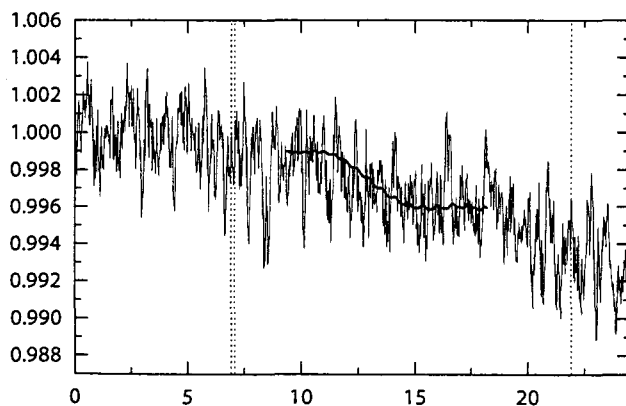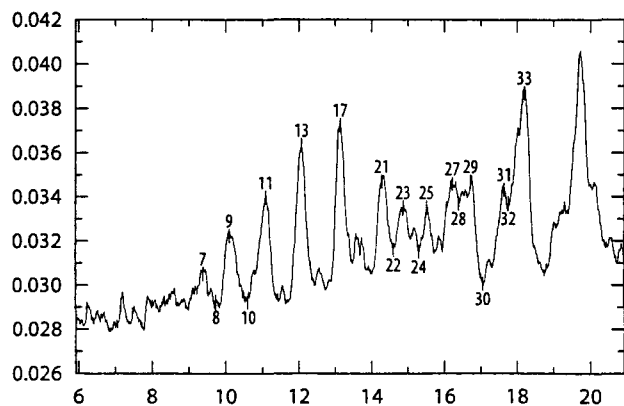
Experiment 43
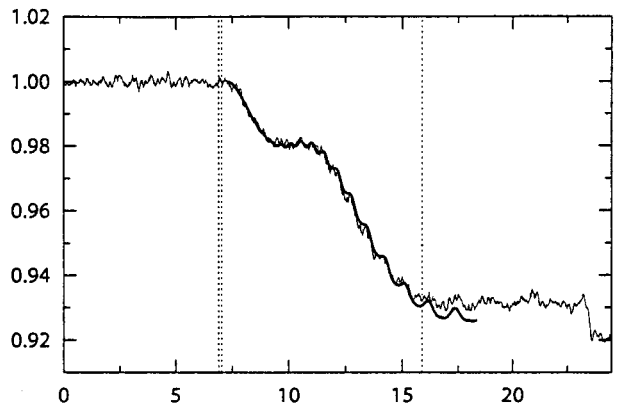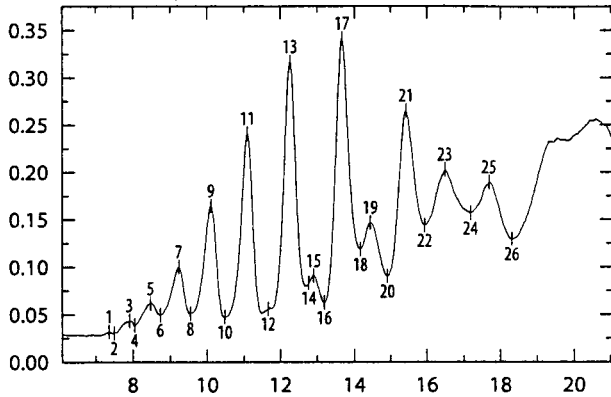
Experiment 44
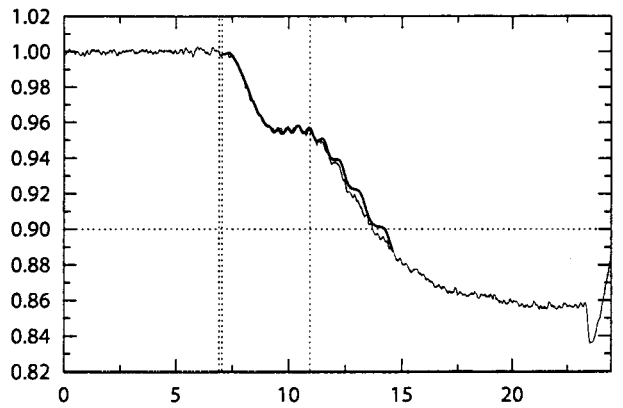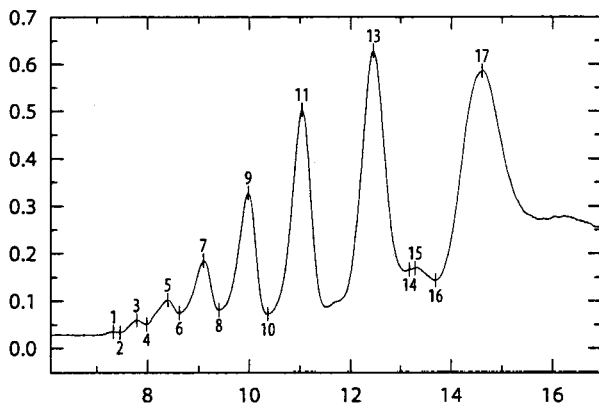
Experiment 45
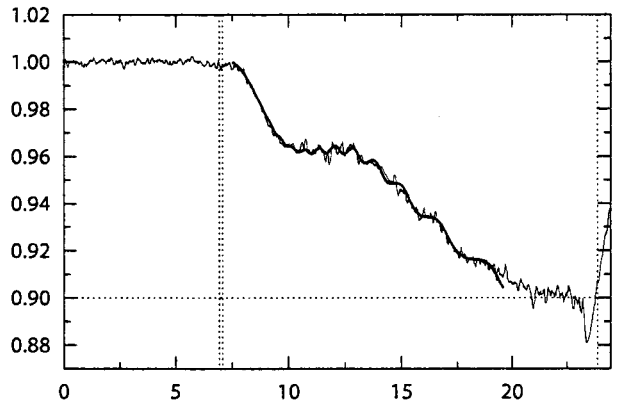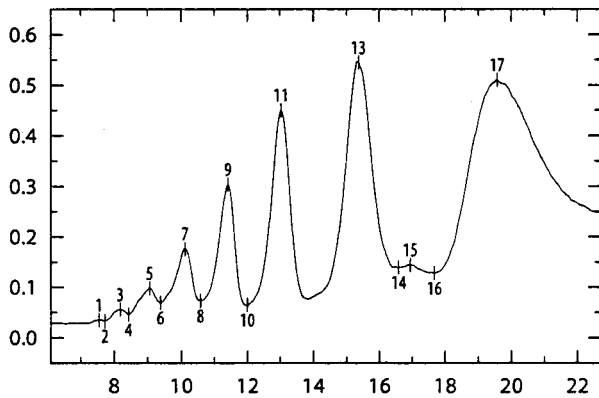
Experiment 46
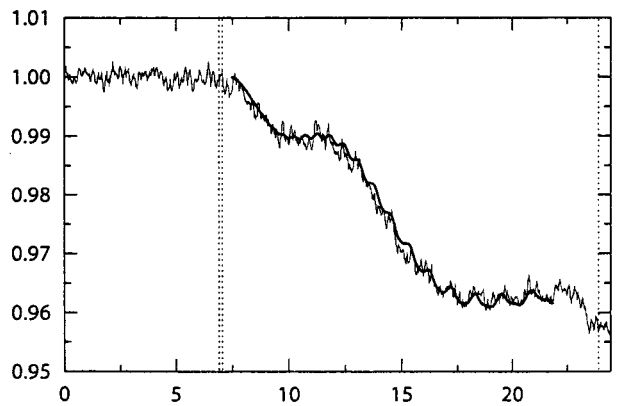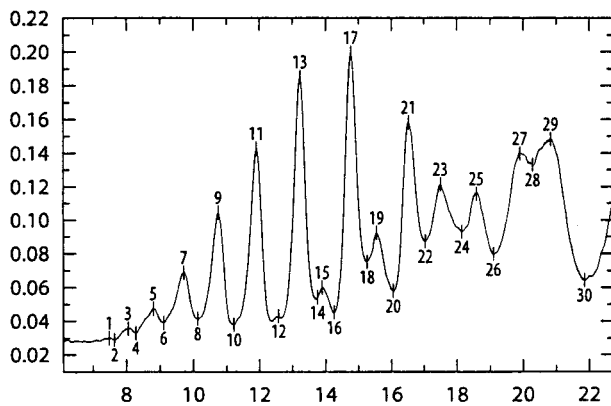
Experiment 47
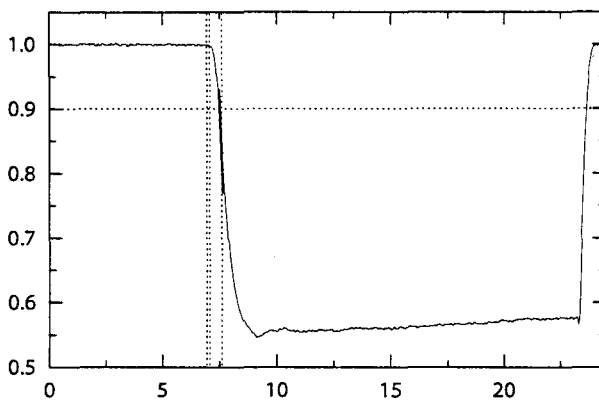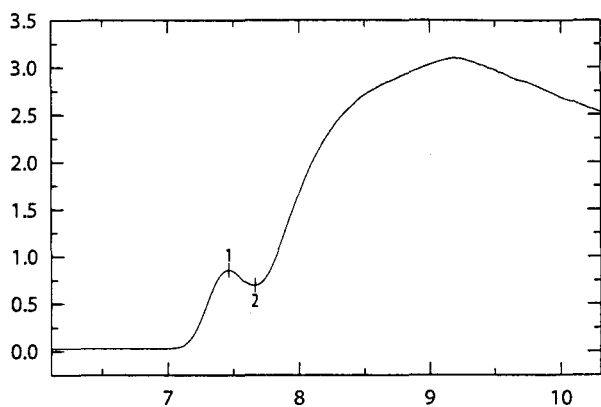
Experiment 48
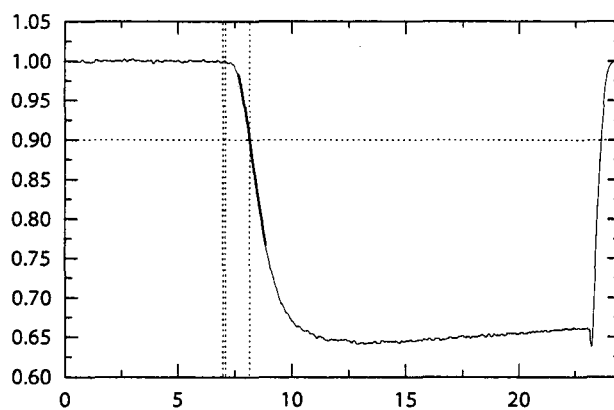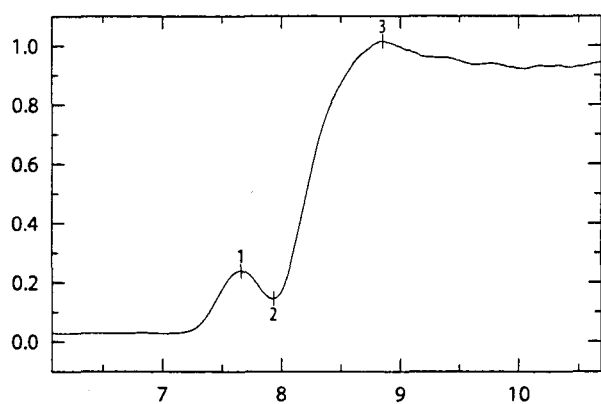
Experiment 49
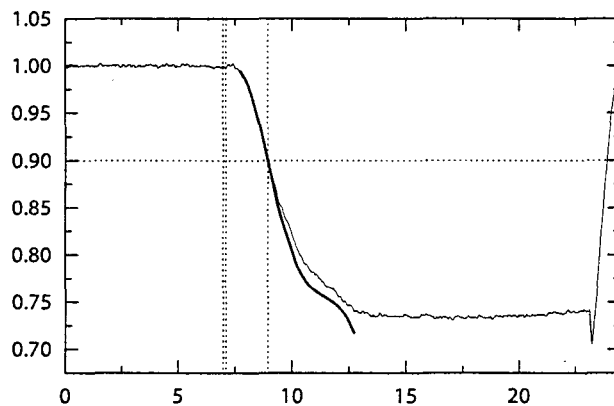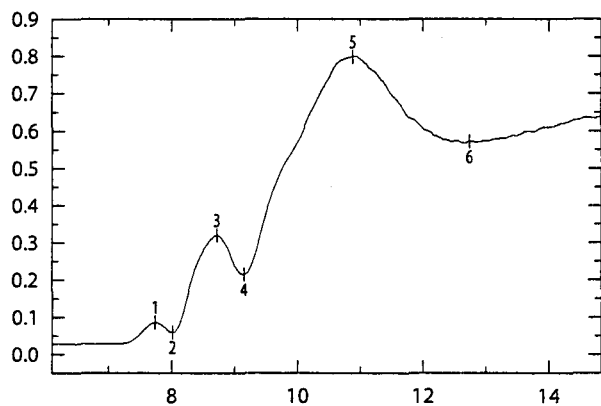
Experiment 50
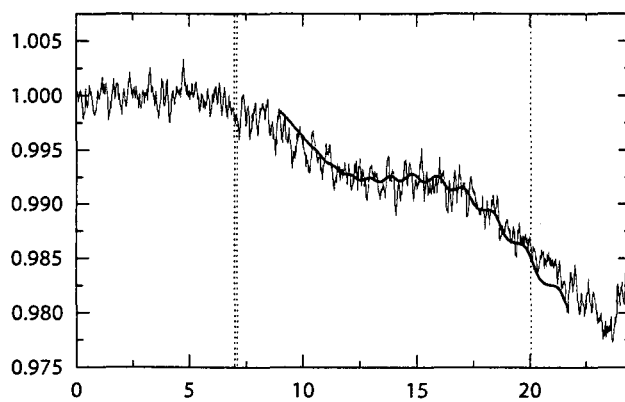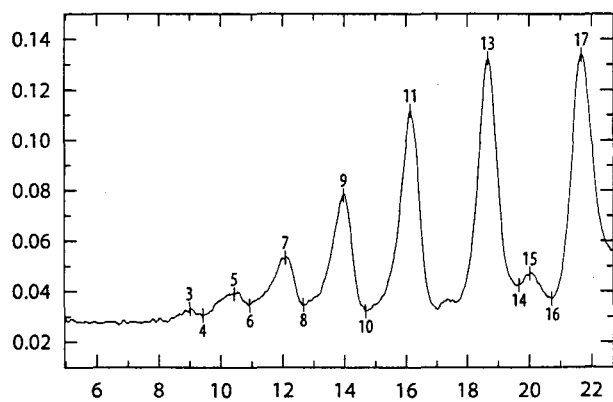
Experiment 51
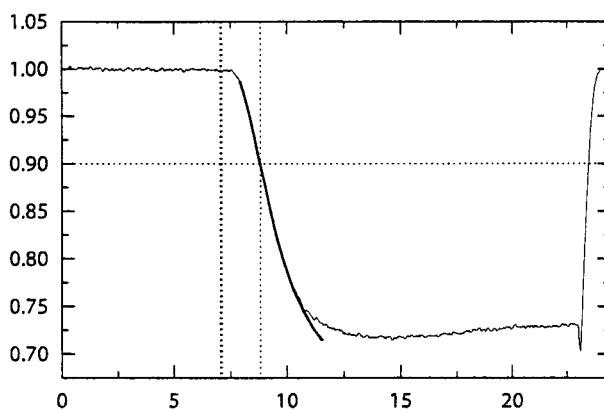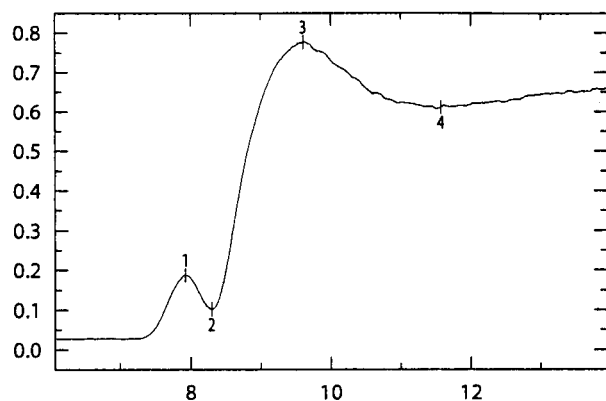
Experiment 52
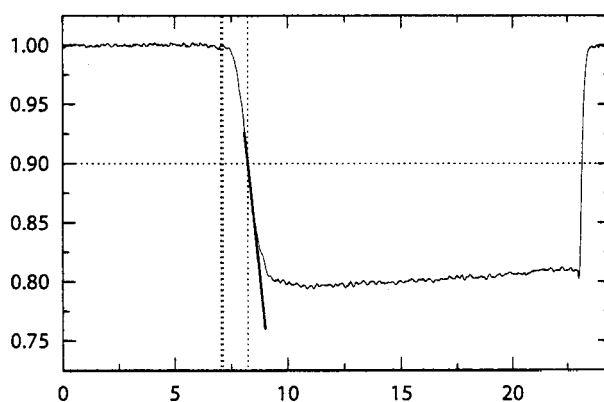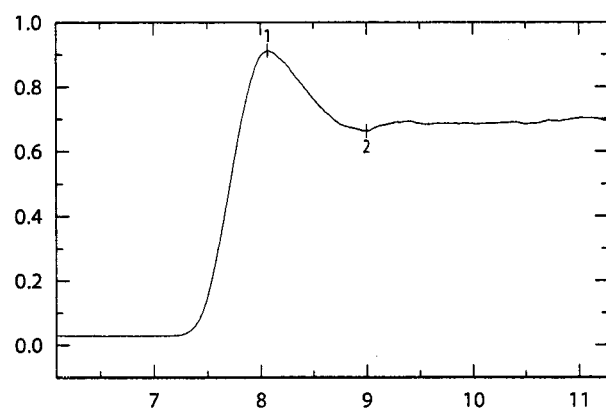
Experiment 53
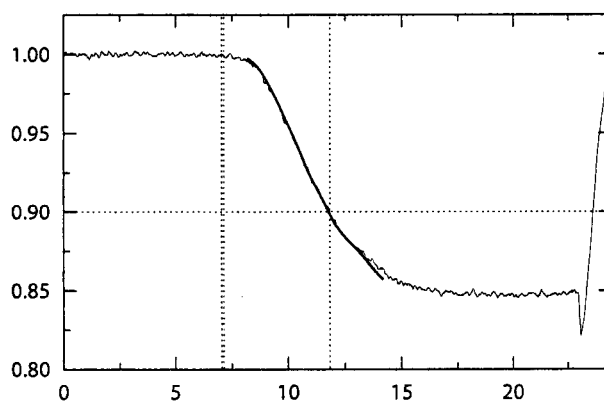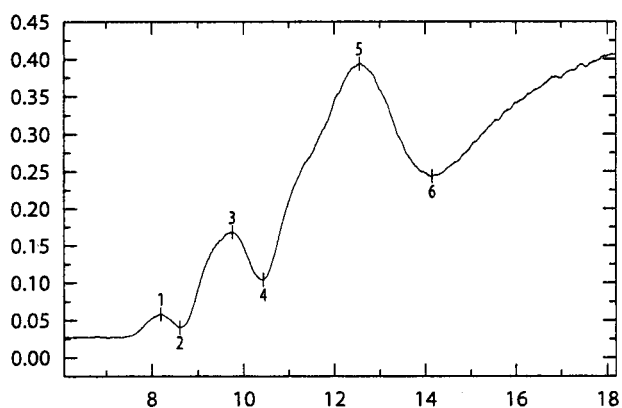
Experiment 54
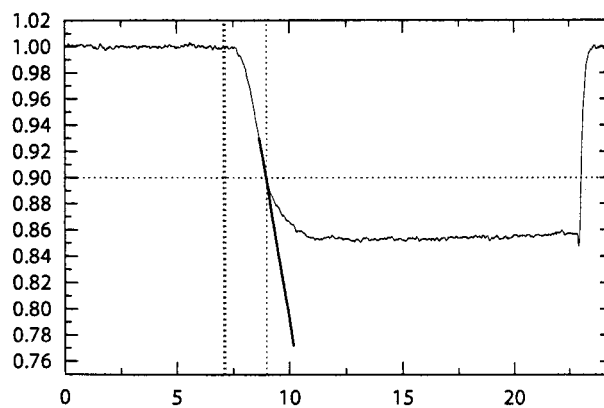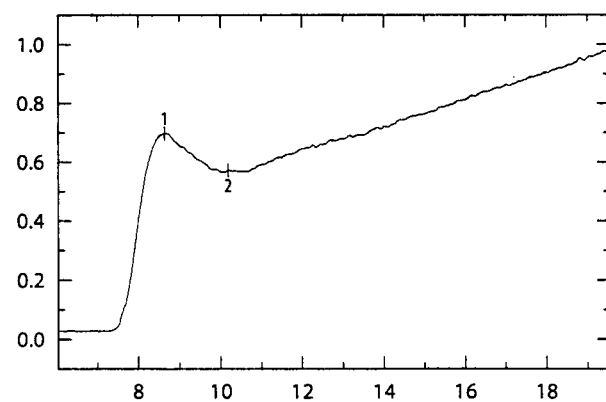
Experiment 55
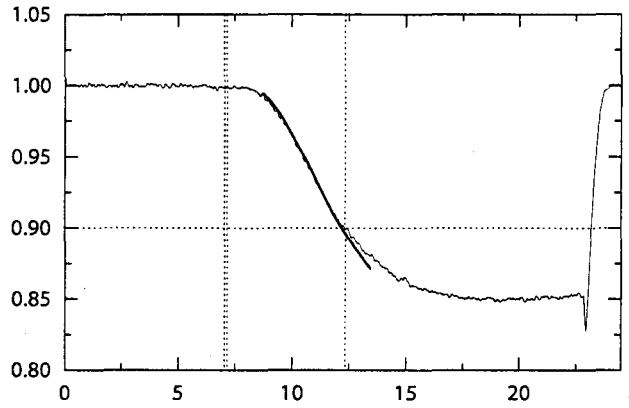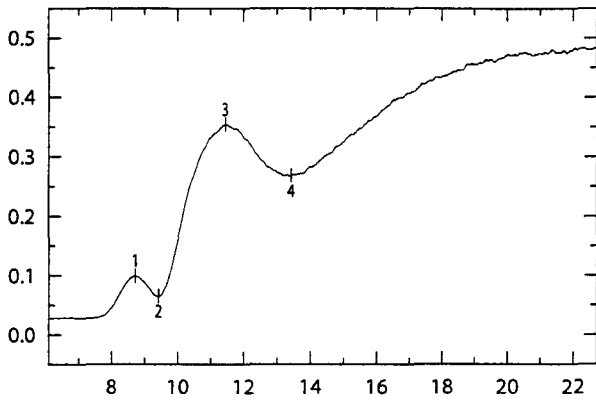
Experiment 58
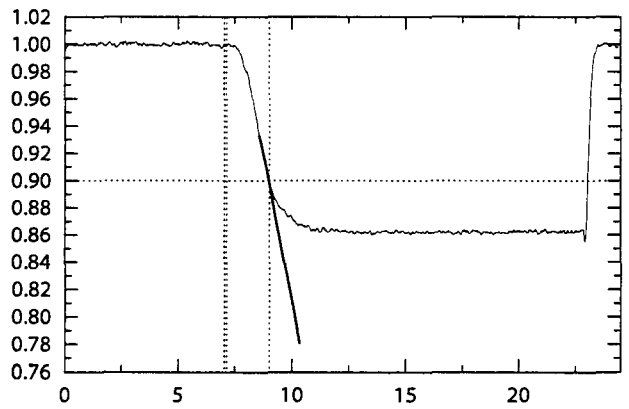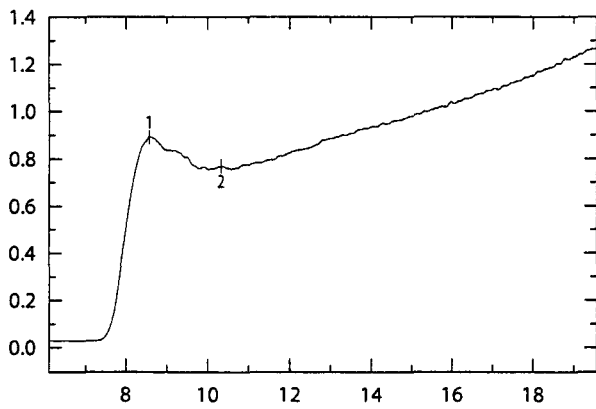
Experiment 59
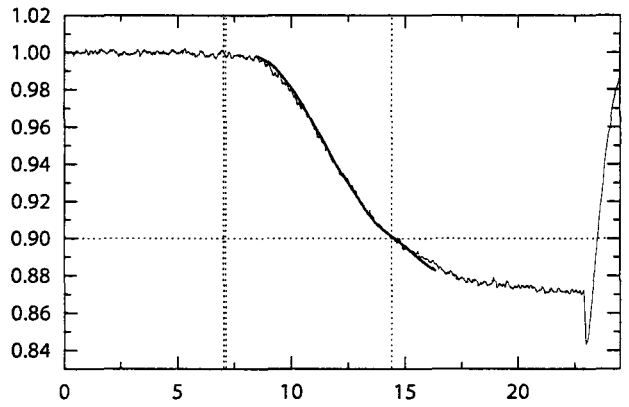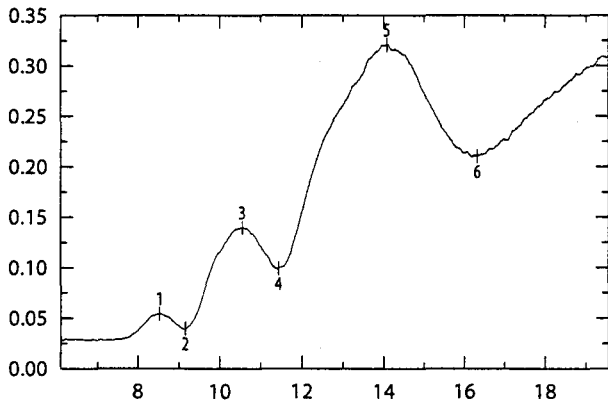
Experiment 60
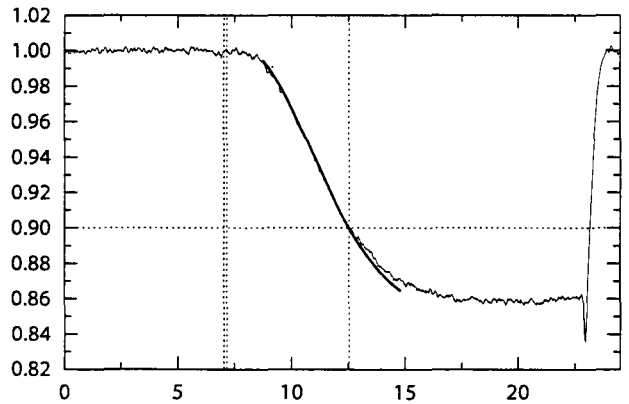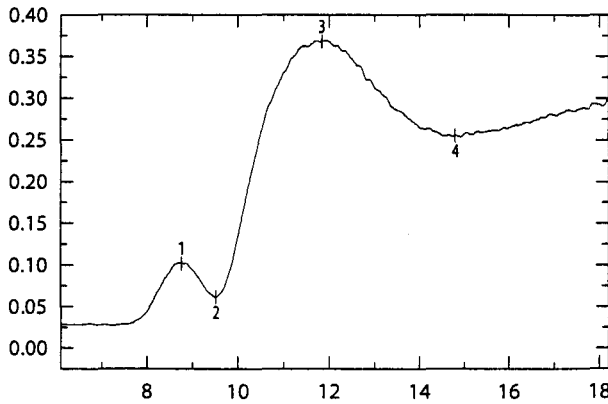
Experiment 62
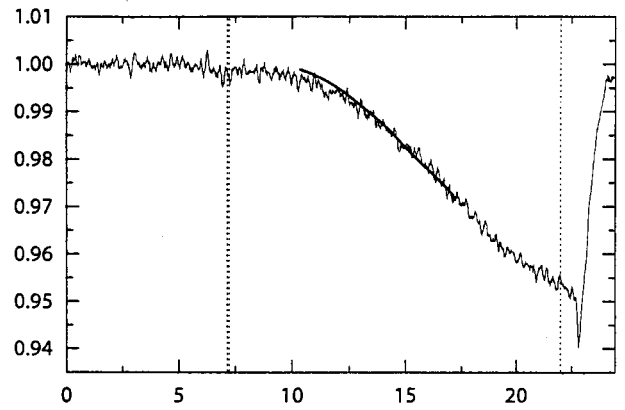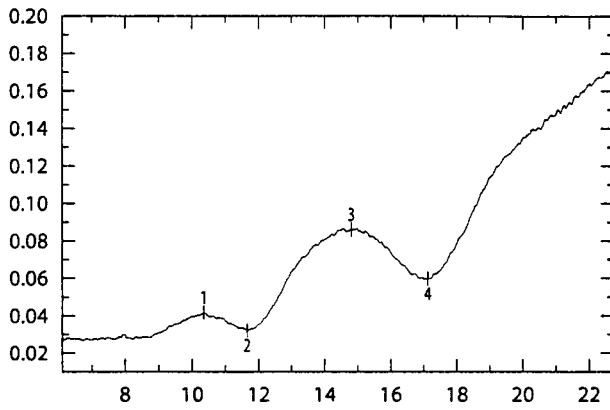
Experiment 66
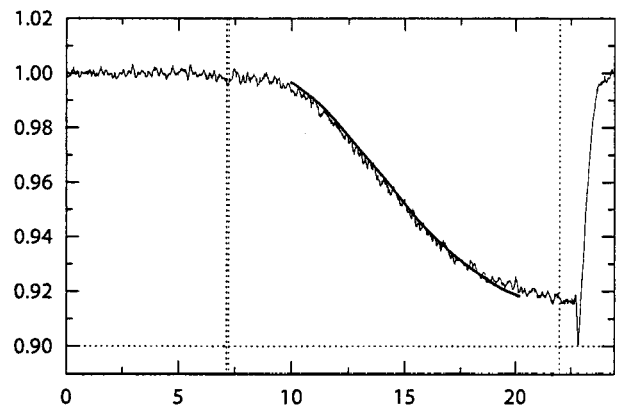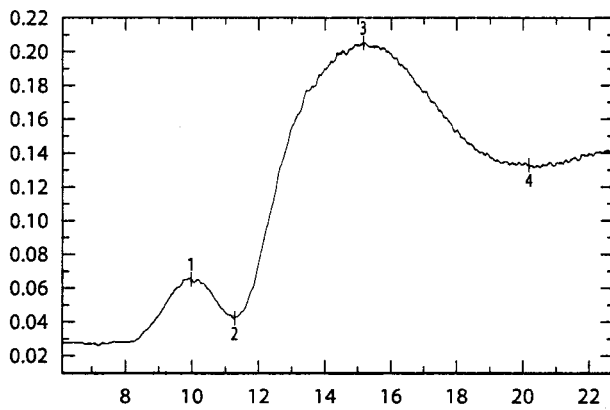
Experiment 67
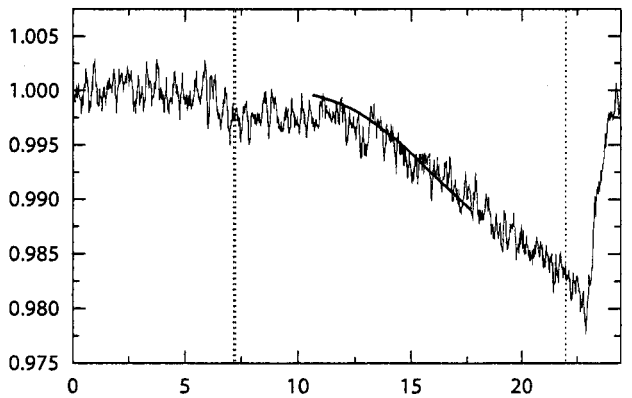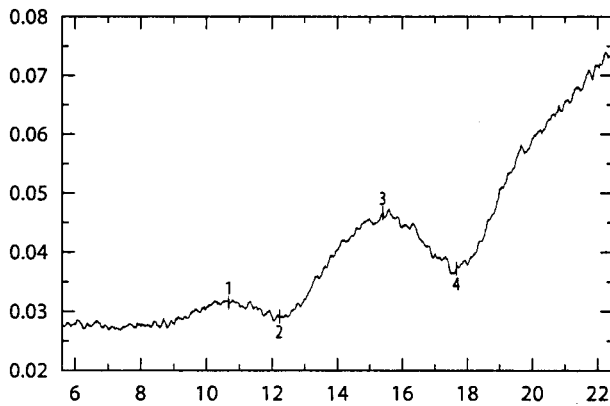
Experiment 68
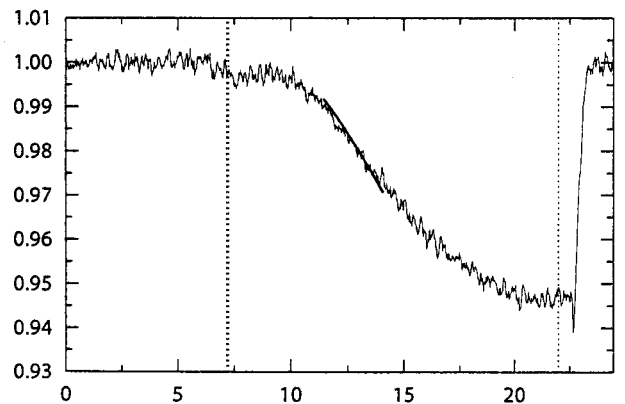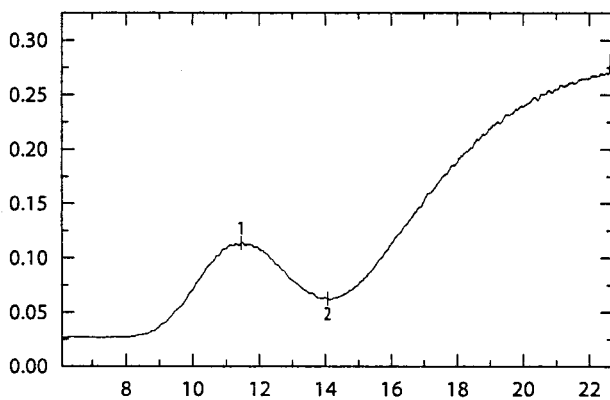
Experiment 69
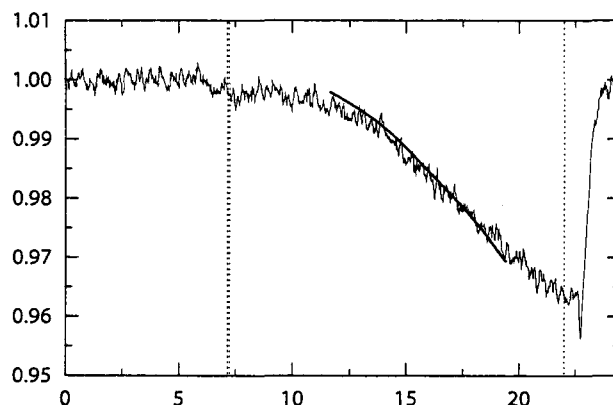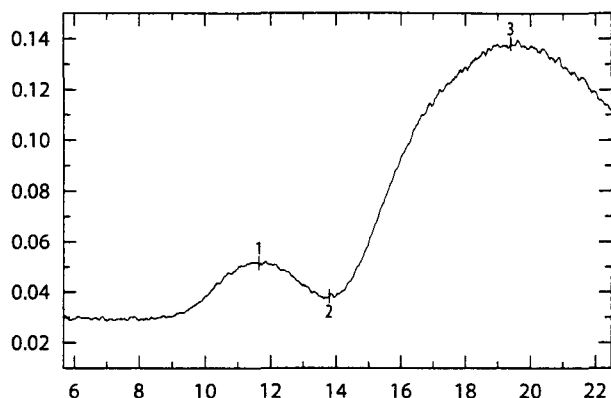
Experiment 70
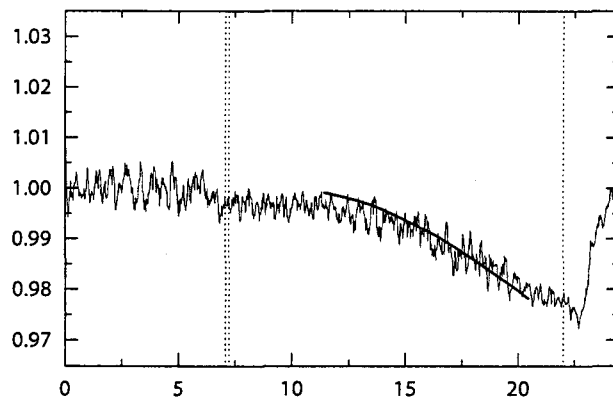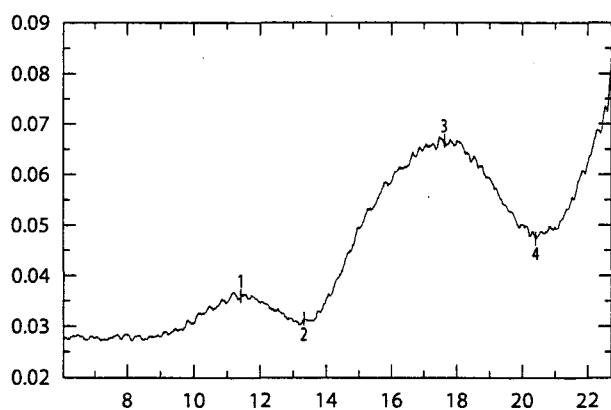
Experiment 73
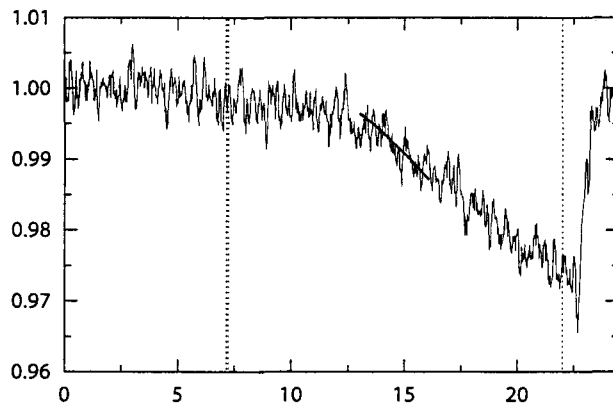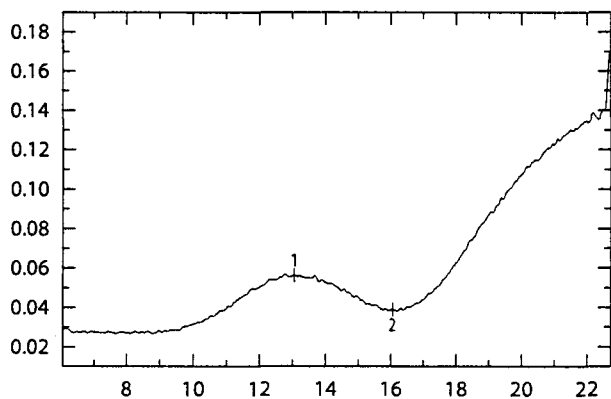
Experiment 74
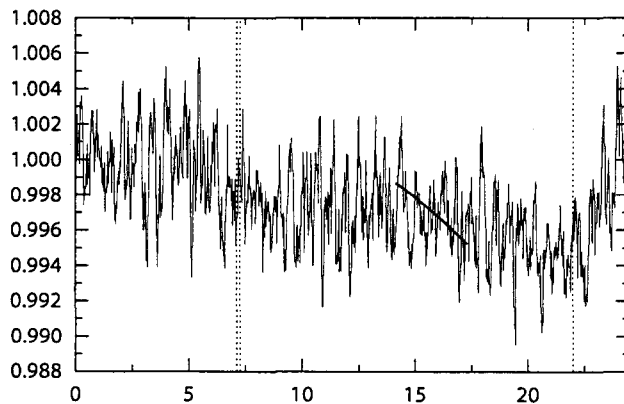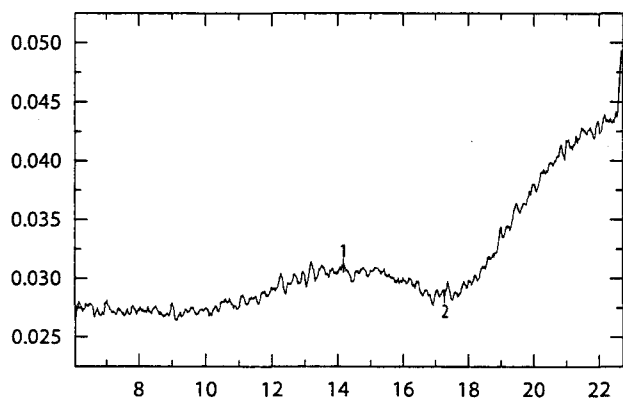
Experiment 75
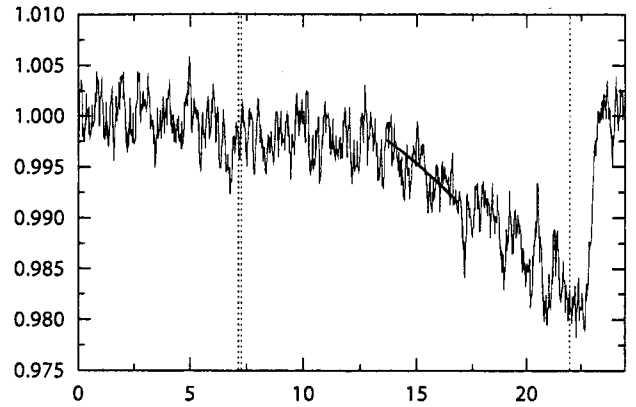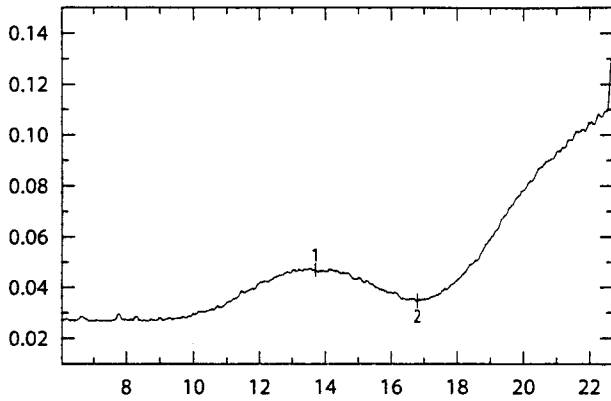
Experiment 77
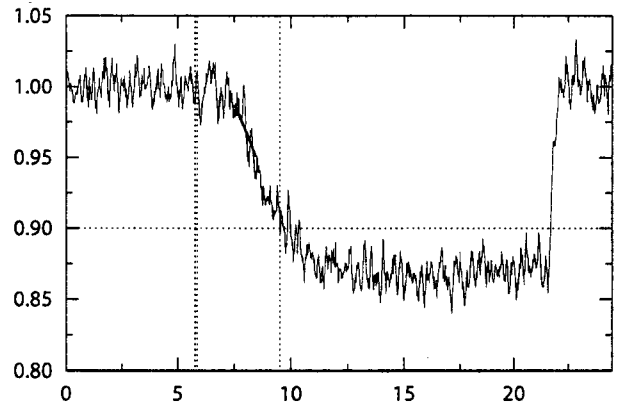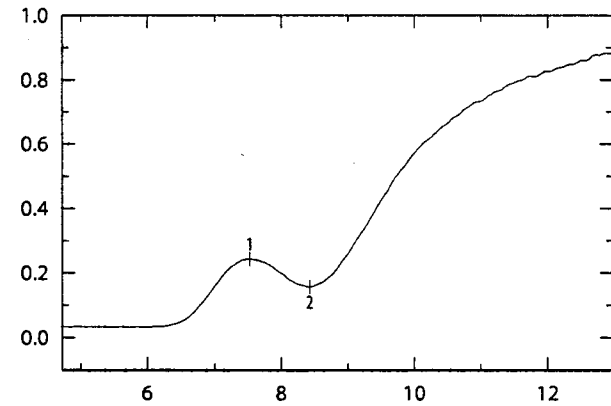
Experiment 82
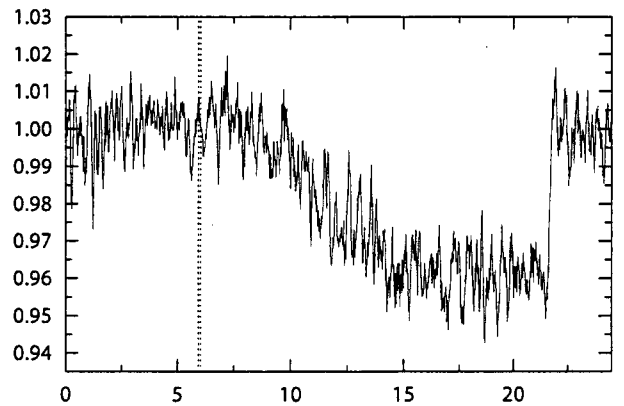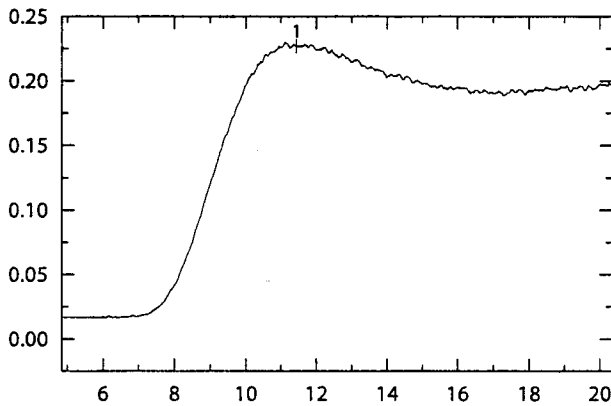
Experiment 83
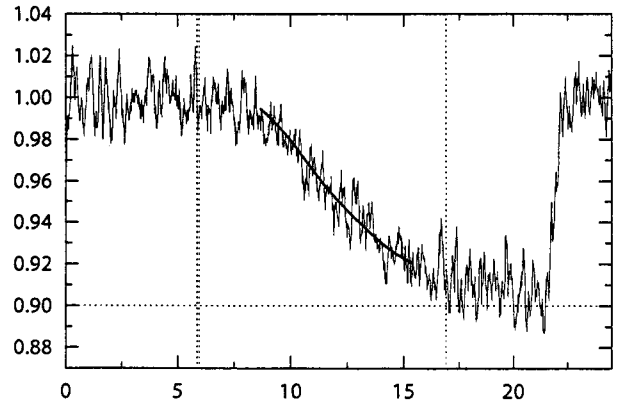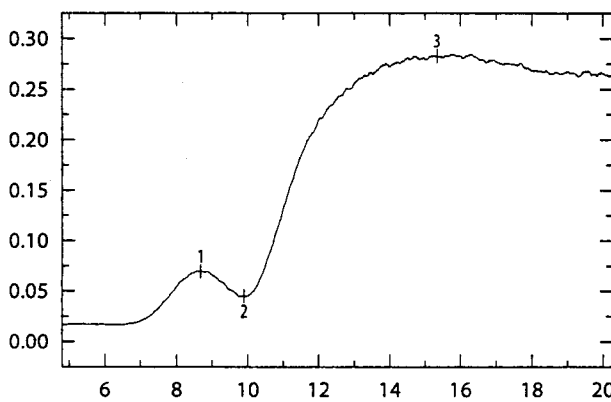
Experiment 84
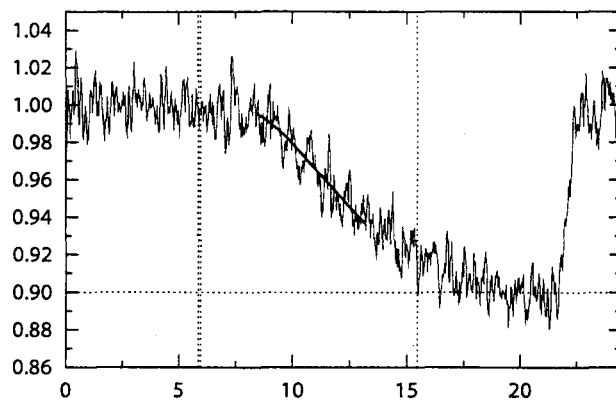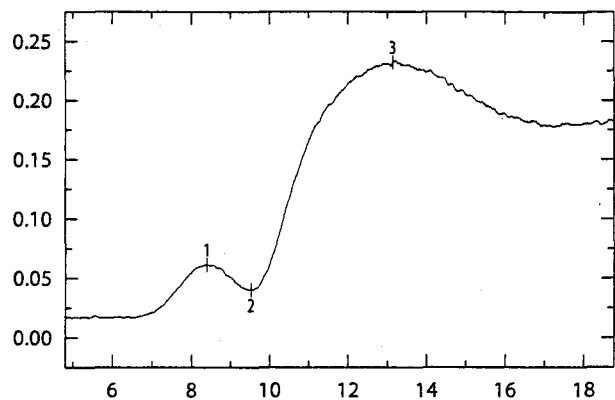
Experiment 87
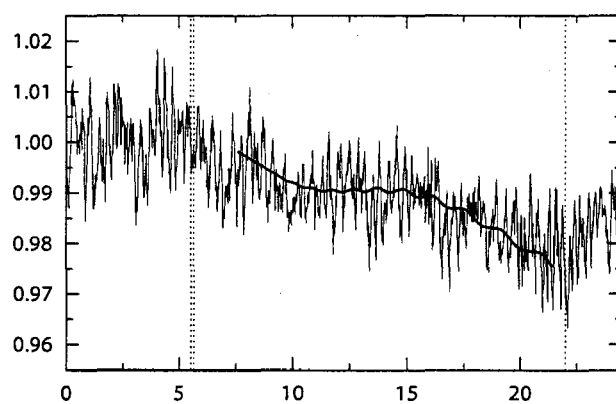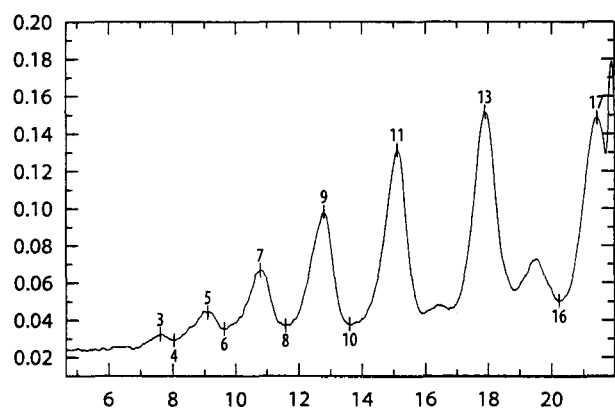
E. Rewriting Eq. 2.57

Using a first-order approximation,

$$\ln Q_{N-n}(V - v_n) = \ln Q_{N-n}(V) - \frac{\partial \ln Q_{N-n}(V)}{\partial V} v_n. \tag{E.1}$$

According to Eq. 2.52, the pressure p is defined as

$$p = kT \frac{\partial \ln Q_{N-n}(V - v_n)}{\partial V - v_n}. \tag{E.2}$$

If $v_n \ll V$, then the quantity $kT \, \partial \ln Q_{N-n}(V)/\partial V$ is also equal to p, so that

$$\ln Q_{N-n}(V - v_n) = \ln Q_{N-n}(V) - \frac{p v_n}{kT}, \tag{E.3}$$

and

$$Q_{N-n}(V - v_n) = Q_{N-n}(V) e^{-p v_n/kT}. \tag{E.4}$$

F. Technology assessment

The formation of a new phase through the process of homogeneous nucleation plays an important role in many technological applications. For example, in steam turbines, homogeneous nucleation can lead to a loss of efficiency. The natural gas industry needs accurate descriptions of the nucleation of vapours such as water to remove them from the gas. Natural gas consists mainly of methane, but also contains undesired components such as water vapour and hydrocarbon vapours. One way to remove them is to cool the gas so that the vapours condense to droplets, which can be swirled out of the gas by a strong rotation.

In meteorology, knowledge of the nucleation of water is also essential; not only for short-term weather prediction but also for the modelling of long-term climate changes. In clouds, the tiny water droplets are often supercooled; liquid droplets have been observed at temperatures as low as -40 °C. The way in which clouds reflect and absorb solar radiation is different for clouds consisting of liquid water and for clouds that contain ice particles, so the fact that supercooled liquid can be formed from the vapour can have an influence on the climate.

Acknowledgements